THE SKA'S THE LIMIT:
ON THE NATURE OF FAINT RADIO SOURCES

A thesis submitted in fulfillment of the
requirements of the degree of:

Doctor of Philosophy

at

Rhodes University

by

Kim McAlpine

May 2012

Abstract

Within the next few years a large number of new and vastly more sensitive radio astronomy facilities are scheduled to come online. These new facilities will map large areas of the sky to unprecedented depths and transform radio astronomy into the leading technique for investigating the complex processes which govern the formation and evolution of galaxies. This thesis combines multi-wavelength techniques, highly relevant to future deep radio surveys, to study the evolution and properties of faint radio sources.

Two studies of the evolution of low luminosity radio sources are presented, one over a larger survey area of 2.75 degrees^2 limited to redshifts of $\sim$1.2 with only relatively coarse redshift information derived from single band photometry and a study over a smaller area (1 degree^2) utilising deeper radio data and multi-band optical and near-infrared data to obtain more accurate photometric redshift estimates. This second study investigates the radio luminosity function out to redshifts of $\sim$2.5. The results indicate that low-luminosity radio sources undergo mild positive evolution out to redshifts of $\sim$1.2, with tentative evidence of a decline in the number densities beyond this threshold.

This thesis also investigates the possibility of using multi-band SED fitting techniques to identify AGN and star-forming galaxies in faint radio populations. Based on comparisons with the SKADS simulations it appears that these techniques can identify a large fraction of AGN in the local universe ($z \leq 1$) based on their observed tendency to be hosted in galaxies with red optical colours.

A comparative study of the performance of a widely used cross-matching technique, the likelihood ratio, at resolutions of 6, 10 and 15 arcsec was also performed. This study was undertaken to determine whether the lower resolutions of planned future surveys including the Evolutionary Map of the Universe (Norris 2011; 10 arcsec resolution), and Westerbork Observations of the Deep APERTIF Northern-Sky (WODAN; 15 arcsec resolution) would significantly compromise their ability to identify multi-wavelength counterparts to faint radio sources. The results of this study indicated that when matching radio observations complete to $\sim$100 μJy to deep near-infrared observations complete to $K_{\mathrm{s}} \leq 22.6$ the likelihood ratio identifies reliable counterparts to 89, 86, and 82% of the radio sources at resolutions of 6, 10 and 15 arcsec respectively.

Acknowledgements

Special thanks to my supervisor superhero team, Prof. Matt Jarvis, Dr. Dan Smith and Dr. David Bonfield whose superpowers include rescuing Phd students in distress, lightning fast response times to questions, eagle-eyed draft reading and superhuman patience. Thank you for all your help, encouragment and advice during the course of my thesis, it was such a great priviledge to work with you.

I would also like to acknowledge the support of my Rhodes supervisor Prof. Justin Jonas and the financial support of the SKA bursary scheme and the NRF.

To the chicksoc chicks thanks for all the wine, sushi, chocolate and good gossip. Necessary provisions to guard against exhaustion and panic during those seemingly endless long, hard Phd years.

Thanks to my long time, long suffering, office mate Laura, who was not only a patient and supportive office mate but a wonderful friend.

To my husband Andrew, who provided me with constant support and love and who more than anyone was on the front lines of the Phd battle.

Thanks to my mum, dad and sister, for their faith in me, for their unwavering support and for providing encouraging motivational slogans,

“Nothing succeeds like a beakless budgie”

Declaration

I certify that this thesis has not been submitted for a degree in any other university and that it is my original work.

The work in chapter 2 has been published in Monthly Notices of the Royal Astronomical Society, volume 413, page 1054, McAlpine K., and Jarvis M.J., *The evolution radio sources in the UKIDSS-DXS-XMM-LSS field*

The work in chapter 3 has been accepted for publication in Monthly Notices of the Royal Astronomical Society, tmp 2986M, McAlpine K., Smith D.J.B., Jarvis M.J., Bonfield D.G., Fleuren S., *The likelihood ratio as a tool for radio continuum surveys with Square Kilometer Array precursor telescopes*

Contents

List of Figures

List of Tables

Chapter 1 Introduction

1.1 *AGN-The unified model*

The term Active Galactic Nucleus (AGN) refers to a class of highly luminous sources which emit from very compact regions in the centres of galaxies whose emission is powered by accretion onto a massive black hole. Historically the group of objects now collectively referred to as AGN were divided into a number of sub-classes based largely on the characteristics of their observed spectra. However modern AGN unification schemes imply that at least some of these classes represent different orientations of an intrinsically similar set of objects. Based on their spectra AGN can be classified into two broad categories. Type 1 AGN exhibit bright non-stellar continuum emission from UV through to X-ray wavelengths, the continuum is approximately described by a power law and their spectra exhibit both narrow ($\leq$1000 km s^{-1}) and broad ($\geq$1000 km s^{-1}) emission lines. In contrast Type 2 AGN have weak continuum emission and only narrow emission line features. The basic features of Type 1 and Type 2 AGN's in the unified model are illustrated in figure 1.1. In the following sections I describe the main components of an AGN.

1.1.1 *A supermassive black hole*

Shortly after the discovery of the first powerful AGN, which drew considerable attention in the astronomical community due their exceptionally high luminosities, strong theoretical arguments determined that gravitational accretion onto a supermassive black hole ($> 10^6 M_\odot$) was the most plausible mechanism capable of producing the required amounts of energy (Salpeter, 1964; Zel'Dovich, 1964; Lynden-Bell, 1969). It is now believed that every galaxy harbours a central black hole, a relic of a previous 'active' phase during which the black hole was still actively accreting mass. Evidence of black holes in both active and normal galaxies has steadily accumulated over the last two decades. Measurements of the proper motions of stars in our own Milky Way Galaxy determine the mass of the black hole at the centre of our galaxy as

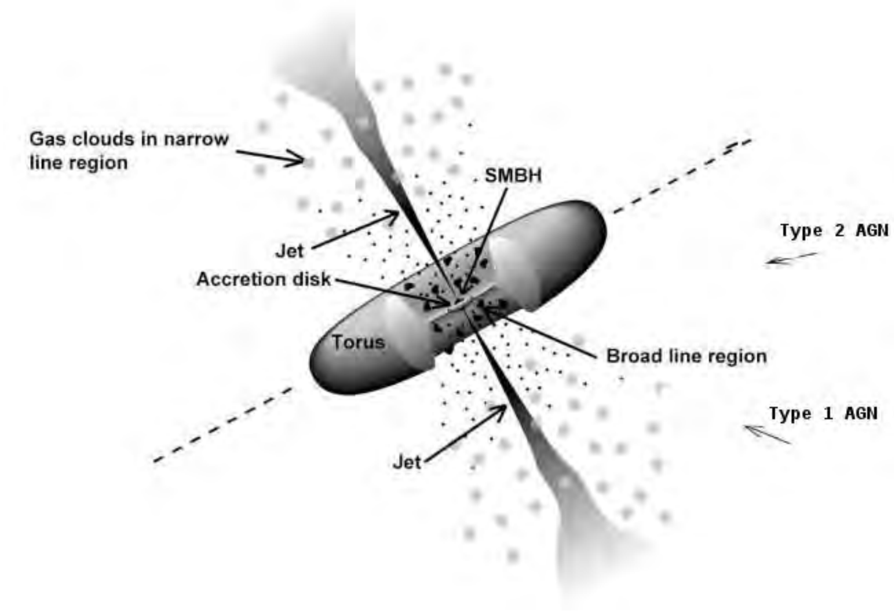

Figure 1.1: The unified model of an AGN. Differences in the observed spectra of Type 1 and Type 2 AGN occur due to the presence of a dusty torus which obscures the emission generated by the broad line region and the accretion disk from certain viewing angles. Original image from Urry and Padovani (1995).

$3.7\times10^{6}M_{\odot}$ (e.g. Eisenhauer et al., 2005; Ghez et al., 2005). While radial and proper motions of H_20 masers in the active galaxy NGC 4258 place its mass at $3.6\times10^{7}M_{\odot}$ and size at < 0.13 pc (Miyoshi et al., 1995; Herrnstein et al., 1999). Dynamical modelling of resolved stars and gas disks in nearby galaxies also provide further evidence of central massive black holes of the the order of $10^{6-9}M_{\odot}$(see Kormendy and Richstone, 1995; Magorrian et al., 1998; Ferrarese and Merritt, 2000).

1.1.2 *An accretion disk and corona*

Theoretical models predict that the accreting material forms a geometrically thin, optically thick accretion disk (e.g. Shakura and Sunyaev, 1973; Novikov and Thorne, 1973). These accretion disks form at radii of approximately 10 R_g, where R_g is the gravitational radius of the black hole given by :

$$R_g = \frac{GM}{c^2} \tag{1.1}$$

G is the gravitational constant, M is the mass of the black hole and c is the speed of light. For typical AGN black hole masses of 10^8 $M_{\odot}$ this implies disk radii of 10^{-5} pc making it impractical to resolve the accretion disks of even the most nearby AGN. This lack of detailed observational constraints means that predictions about the behaviour of the accretion disk close to the black hole rely heavily on theoretical arguments. The mechanisms responsible for transferring angular momentum outwards causing matter in the disk to spiral slowly inwards, and ultimately into the black hole, are poorly understood. Whatever the driving mechanism, the basic premise is that as matter spirals inwards its gravitational potential energy is transferred into radiative or thermal energy emitted approximately perpendicularly to the disk. It is commonly assumed that the emission from the disk is thermal which at luminosities approaching the Eddington limit, the highest luminosity a source of mass M can have and still be stable against radiation pressure, implies that most of the emission from the disk is emitted in the UV/optical regime. Under this assumption the accretion disk is responsible for the stong continuum emission detected in Type 1 AGN from UV through to soft (<2 keV) X-ray wavelengths. Although theoretical accretion disk models predict a strong excess of UV and optical emission, roughly corresponding to the predominantly blue spectra of AGN, they do not accurately reproduce the detailed spectral profile of continuum emission in AGN (see Koratkar and Blaes, 1999, for a review).

Both Type 1 and 2 AGN emit in the hard (>2 keV) X-ray band with an approximate power law spectrum. The hard X-ray emission is believed to be due to Compton upscattering of optical/UV photons emitted by the accretion disk by thermal or non-thermal electrons in a region close to the black hole, possibly in a magnetised corona.

1.1.3 *Clouds of high velocity gas*

These are usually referred to as the broad-line region (BLR) clouds. Photoionisation of these gas clouds by the accretion disk emission results in the characteristic broad emission line spectra of Type 1 AGN. The lines are broadened due to their high velocity motion in the gravitational field of the central black hole. The nearly complete absence of broad forbidden emission lines implies that the gas in this region must be dense in order to rapidly collisionally de-excite the energy levels which could give rise to these forbidden transitions. This argument implies that the density in this region is of the order $n_e \geq 10^8$ cm^{-3} (Osterbrock, 1989).

The strength of the emission lines are strongly variable and respond to variations in the

AGN continuum flux, with a certain delay. Measuring this delay and assuming that the gas clouds follow Keplerian orbits allows one to infer the approximate size of the BLR. Studies using this technique, known as reverberation mapping, imply that this region is extremely compact with sizes of the order of several light days to light months and that the radius of the BLR is correlated with AGN luminosity (e.g. Peterson et al., 2004; Kaspi et al., 2005).

1.1.4 *Clouds of lower velocity gas*

These are referred to as the narrow-line region (NLR) clouds. Photoionisation of these gas clouds located much further away from the central black hole than the BLR is thought to be responsible for the narrow emission lines detected in both Type 1 and 2 AGN. Narrow band imaging of the NLR region indicates that it extends between 0.1-5 kpc for typical optically bright AGN and 10-100 kpc in radio loud AGN where line emission is aligned with the radio emission. As is the case for the BLR, its size appears to scale with AGN luminosity (Bennert et al., 2002; Schmitt et al., 2003; Bennert et al., 2006). The NLR exhibits both permitted and forbidden lines indicating that conditions in these clouds are much less dense than in the BLR. There is also evidence that the electron density and ionisation parameters in these clouds decrease with distance from the central black hole (Bennert et al., 2006). There is no evidence that the narrow emision lines are variable, this is to be expected as the low density of these regions results in very long recombination times ($\sim$100 yr) making it much less sensitive to variations in the ionising flux (Yip et al., 2009).

1.1.5 *An obscuring torus*

The existence of an obscuring structure of gas and dust which hides the continuum flux generated by the accretion disk and the BLR from certain viewing angles is the central premise of the AGN unification theory. Although this obscuring structure was initially assumed to be toroidal in shape little is known about the precise geometry of this region. The size of the obscuring torus is approximately a parsec in order to obscure the BLR at certain orientations but still afford a clear view of the NLR in both types of AGN. Support for the existence of this obscuring structure was first discovered using spectropolarimetry of NGC 1068, an archetypal Type 2 AGN. The polarised spectrum of this object was found to have broad emission lines similar to those observed in Type 1 AGN which implied the presence of a hidden BLR whose detected emission is highly polarised due to its reflection from a scattering medium (Antonucci and Miller, 1985). Polarised broad lines have subsequently been observed in several other Type 2 AGN (Heisler et al., 1997; Moran et al., 2000; Tran, 2001, 2003). Since the original discoveries of Antonucci and Miller (1985) the existence of an obscuring medium in many AGN has been confirmed by a wide range of observational techniques.

These include the detection of conically shaped NLR in narrow band images and integral field spectroscopy of several nearby AGN (Pogge, 1988; Evans et al., 1991; Barbosa et al., 2009). If the NLR in Type 2 AGN is created by photoionisation from a nuclear accretion disk partially hidden from sight by a toroidal absorber then it should exhibit such a biconical structure due the restricted angle of the escaping ionising light.

Further support of an obscuring structure is found in X-ray observations, both Type 1 & 2 AGN exhibit very similar characteristics in their hard X-ray spectra but Type 2 AGN are often weak or undetected in the soft X-ray band. This favours a common central emission mechanism for both types with the soft X-rays in Type 2 AGN being absorbed by an intervening medium.

Interferometric studies at mid- and near-infrared wavelengths have also detected emission from a dusty circumnuclear region at parsec or sub-parsec scales as predicted by the unified model (Jaffe et al., 2004; Tristram et al., 2009; Kishimoto et al., 2011). Despite the many successes of the unified model in describing the general emission properties of AGN and the ample observational evidence that some Type 2 AGN are obscured Type 1 objects, there are still many open questions surrounding AGN. In particular it is not certain that all Type 2 AGN harbour a hidden BLR, Tran (2001) demonstrated that AGN Type 2 sources with and without polarised hidden BLR in their spectra have very similar levels of dust obscuration indicating that the BLR may be truly absent in the non-detected sources as opposed to just heavily obscured. Evidence is also mounting that the original model of a dusty parsec scale torus as the primary source of obscuration is too simplistic to account for the observed properties of Type 2 AGN and that there may be multiple, possibly ‘clumpy’, absorbing structures at different scales within the circumnuclear region (see Bianchi et al., 2012, for a review). While recent results using infrared spectral energy distribution fitting of nearby AGNs imply that the

Type 2 AGN may have obscuring tori which are systematically deeper and 'clumpier' than the Type 1's, resulting in a smaller probability of obtaining a direct view of the central emission disk and BLRs in these objects (Alonso-Herrero et al., 2011). Thus observed differences in AGN types may not be merely a question of viewing angle, but of different intrinsic properties of the obscuring stucture.

In radio, optical and X-ray selected AGN samples it has been found that the fraction of obscured Type 2 AGN increases towards lower luminosities (Willott et al., 2000; Simpson, 2005; Hasinger, 2008). It has been suggested that this trend might result from the presence of a separate class of low luminosity AGN, distinct from those described by the AGN unification scheme, which are included in the 'obscured' AGN class in these studies (Willott et al., 2000; Hopkins et al., 2009). There has also been some suggestions that the obscured AGN fraction increases towards higher redshifts (La Franca et al., 2005; Hasinger, 2008), however this result has been the subject of much debate due to the difficulties of disentangling redshift and luminosity effects in flux limited samples.

1.1.6 *Relativistic jets*

A small percentage of all AGN, approximately 5-10%, are radio-loud. This definition encompasses all AGN which have a very high ratio of radio to optical flux. One commonly used definition of radio-loudness is that the ratio of 5 GHz radio flux to B-band (∼4400Å) optical flux is $\geq$10 (Kellermann et al., 1989). The radio emission of these radio-loud sources display clear evidence that they are associated with powerful relativistic jets of plasma ejected from the central AGN. The jets originate very close to central black hole, within 50 R_g, and are observed to extend outwards for up to Mpc in some cases. Evidence of their relativistic nature includes:

- the apparent superluminal motion of jet features on parsec scales (Vermeulen and Cohen, 1994). This phenomenon is explained as an optical illusion created by photons moving along a jet at very high, relativistic speeds, when the jet is orientated at a small angle of inclination towards the observers line of sight.

- the presence of one-sided jets whose observed characteristics are consistent with Doppler boosting of the jet radiation as it propagates in the direction of the observer (Bridle and

Perley, 1984).

- high brightness temperatures of the radio sources, well above temperatures expected by comparison with levels of observed synchrotron generated X-ray emission. This is also consistent with Doppler boosting of the observed radio flux.

Despite much work in this area the mechanisms responsible for launching the relativistic jets in AGN remain unclear, as is the reason for their apparent presence in only a small fraction of known AGN.

As the emision from these jets is strongly anisotropic a number of orientation dependent effects can also be observed in the radio properties of AGN. The overall structure of radio sources emerging from AGN are observed to be comprised of 4 components, a flat-spectrum core possibly associated with the central AGN, twin relativistic jets, large diffuse steep-spectrum radio lobes generated by the interaction of these jets with the surrounding media and in some cases bright hotspots of emission located within the lobes (Miley, 1980). The transition from viewing the radio jets almost pole-on directly down the jet axis to perpendicular to the jet axis results in a corresponding transition from observing very bright, core-dominated flat-spectrum sources and single-sided Doppler boosted jets to double-lobed radio galaxies with steep-spectrum lobe dominated emission (Urry and Padovani, 1995). It is important to note that the jet axis in this scheme may be slightly offset from the axis of the ionisation cone created by the obscuring torus in the AGN unification scheme and that the transition in observed radio source properties may have a different dependence on viewing angle compared to the Type 1 and Type 2 AGN classification scheme. Therefore it is not possible to identify Type 1 or Type 2 AGN exclusively with a particular class of radio source.

1.2 *Radio sources*

The radio population above 1 mJy consists almost exclusively of radio-loud AGN (Windhorst et al., 1985; Willott et al., 2002) whose emission is generated by synchrotron emission due to the interaction of the AGN relativistic jets with a magnetic field. Although orientation effects help to explain some of the observed differences in the properties of radio loud AGN there are divisions in their morphology and emission line characteristics which point to more fundamental variations within this class. The two most widely used schemes for classifying radio sources are described below.

1.2.1 *The FRI/FRII classification*

Radio galaxies were originally classified into two morphologically distinct groups identified by Fanaroff and Riley (1974), which are identified as Fanaroff-Riley class I (FRI) and Fanaroff-Riley class II (FRII) sources (Fanaroff and Riley, 1974). The radio lobes of FRI sources tend to be diffuse with their brightest regions located close to the centre of these lobes. FRII sources have much more collimated large-scale jets with their bright emission hotspots located at the edges of their radio lobes. Examples of radio sources displaying typical FRI and FRII morphologies are presented in figure 1.2.

The FRII sources are also typically more luminous than the FRI sources with the division in luminosity falling at roughly $L_{1.4\mathrm{GHz}} = 10^{25}$ W Hz^{-1}. This dividing luminosity may be dependent on the optical luminosity of the host galaxy, with a higher optical host luminosity resulting in a higher FRI/FRII division luminosity (Ledlow and Owen, 1996). Since its discovery the origins of this observed division has proved to be stubbornly difficult to resolve and has been variously ascribed to differences in the central AGN including the black hole spin and accretion rate (Baum et al., 1995; Meier, 1999; Marchesini et al., 2004) as well as differences in the jet composition and kinetic energy. However the existence of a class of hybrid radio sources in which each of the two lobes display distinctly different FR morphologies lend weight to another popular argument that the separation may be primarily caused by differences in the external media with which the jets interact (Gopal-Krishna and Wiita, 2000).

1.2.2 *High and low excitation radio galaxies*

Recent evidence suggests that a more important division in the radio AGN population, distinct from the morphological classification, may be related to different modes of black hole accretion. Radio-loud AGN have been classified according to the presence or absence of narrow high-excitation emission lines in the spectra of their host galaxies (Hine and Longair, 1979; Laing et al., 1994; Jackson and Rawlings, 1997; Willott et al., 2001). Objects with and without high-excitation emission lines are referred to as high-excitation (HERG) and low-excitation

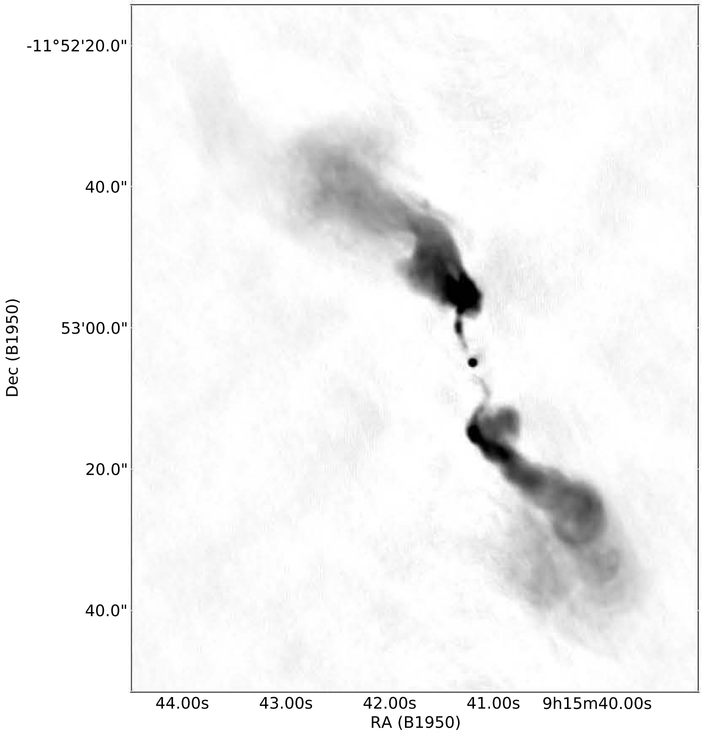

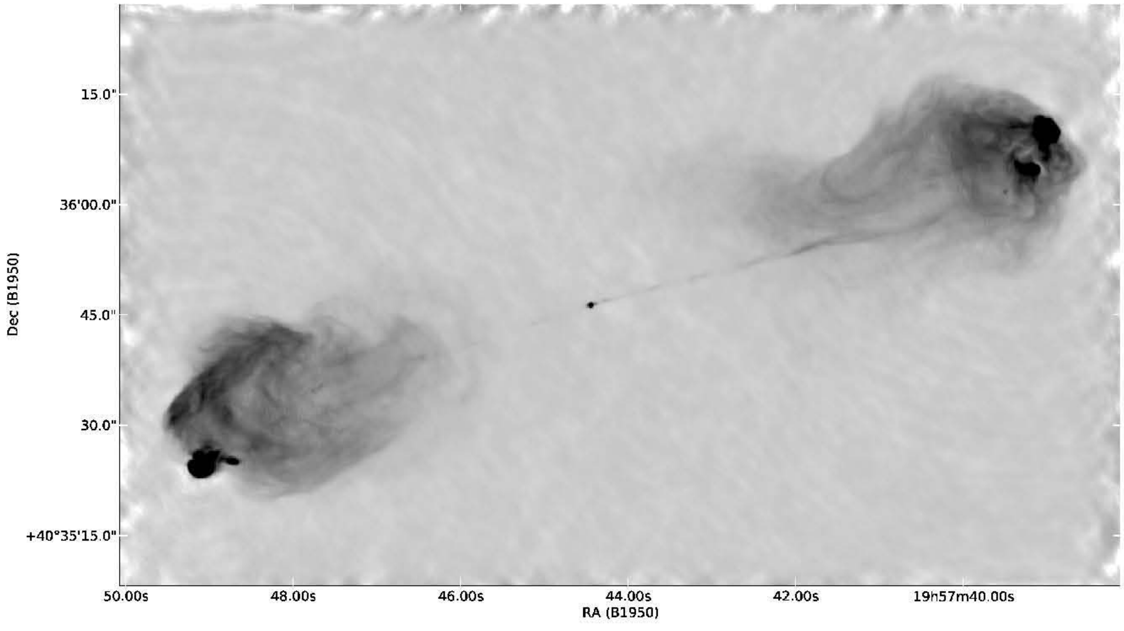

Figure 1.2: Radio images of typical Fanaroff Riley class I and II sources. The top image is Hydra A which displays FRI morphology. The lobe emission is diffuse and the bright emission hotspots are towards the centre of the lobes. Image taken from Taylor et al. (1990). The bottom image is of the FRII source Cygnus A. The bright emission hotspots are located at the edge of the diffuse emission lobes. Image taken from Perley et al. (1984).

radio galaxies (LERG) respectively. Low luminosity FRI galaxies are predominantly LERG's and most objects with high excitation emission lines are associated with the more powerful FRII sources. However the relationship between FR class and the emission line classification scheme is not one-to-one as many FRII galaxies have been found to be low-excitation radio galaxies (e.g. Evans et al., 2006). It has been argued that the LERG/HERG classification schemes correspond to different AGN phenomena powered by fundamentally different modes of accretion. As there is significant overlap in populations classified according to either of these schemes it is reasonable to propose that observed differences between the AGN properties of FRI and FRII populations reported in earlier studies occur as a result of the more fundamental LERG/HERG division in the radio population.

The HERG sources are powered by radiatively efficient accretion of cold gas via an accretion disk and are essentially radio-loud versions of the standard 'unified' AGN which power radio-quiet AGN sources. The LERG sources represent a class of source completely distinct from that described by the simple, orientation based, unified scheme and are powered by radiatively inefficient accretion of the hot gas in the intergalactic medium (Evans et al., 2006; Hardcastle et al., 2006, 2007; Herbert et al., 2010; Best and Heckman, 2012), these two accretion modes are sometimes referred to as "quasar" and "radio" mode accretion respectively. Further evidence in support of the distinct nature of LERG sources is the absence of mid-infrared emission produced by an obscuring torus (Ogle et al., 2006) and accretion-related X-ray emission typically produced by radio-quiet AGN (Hardcastle et al., 2006). While Best et al. (2005a) demonstrated that the low-luminosity radio-loud AGN are statistically independent from the optically selected radio-quiet AGN population.

The host galaxies of these two populations are also distinct with HERG's associated with lower stellar masses and lower black hole masses than LERG's. They are also seen to have bluer colours and shallower 4000Å breaks indicating that the HERG's are preferentially associated with sources with ongoing star formation activity (Kauffmann et al., 2008; Best and Heckman, 2012). The recently derived local luminosity functions of HERG's and LERG's indicate that both types of source occur across the full range of radio luminosities but that LERG's constitute the dominant population below a luminosity threshold of $L_{1.4\mathrm{GHz}} \sim 10^{-26}$ W Hz^{-1} (Best and Heckman, 2012).

Janssen et al. (2012) investigated which host galaxy properties including galaxy mass, star-formation rate and colour are the most influential in governing the formation of both HERG and LERG radio sources. Their results indicate that the fraction of galaxies hosting a radio loud LERG (f_{RL}^{LE}) increases strongly with increasing galaxy mass as $f_{RL}^{LE} \propto M_*^{2.5}$, and saturates at large galaxy masses at a fraction of approximately 10%. While HERG sources show much shallower dependence on galaxy mass with $f_{RL}^{HE} \propto M_*^{1.5}$. Star-formation rate appears to have very little influence on the probability of forming either a radio loud HERG or LERG with f_{RL}^{LE} and f_{RL}^{HE} remaining constant for a wide range of star-formation rates at fixed galaxy mass. The colour preference of LERG galaxies was also shown to be luminosity dependent with a higher fraction of LERG's occuring in red and green galaxies when the selection includes low luminosity radio sources ($\geq 10^{23}$ W Hz^{-1}), while the fraction of LERG's in blue galaxies remains constant regardless of the imposed radio luminosity selection criteria. Thus at higher luminosities the LERG sources are preferentially hosted in blue radio sources. In contrast HERG's at all luminosities are preferentially located in blue and green galaxies.

1.2.3 *The sub-mJy radio source population*

Below a flux density of 1 mJy the synchrotron emission generated by supernovae remnants in ordinary non-active star-forming galaxies in the local universe becomes detectable (Condon, 1992) and the radio population becomes a mixture of star-forming galaxies, radio-loud and radio-quiet AGN (Jarvis and Rawlings, 2004). The relative contributions of each of these classes of radio sources at sub-mJy levels has for many years been the subject of much debate (e.g. Simpson et al., 2006; Seymour et al., 2008; Huynh et al., 2008; Ibar et al., 2009; Smolčić et al., 2008; Padovani et al., 2009). Progress on this question was hampered by the small fields for which deep radio observations were available and the relative scarcity of complementary datasets at other wavelengths necessary for secure classification of these faint radio sources.

Various approaches have been used to separate the AGN and star-forming contributions in radio surveys producing quite variable results. These methods include:

1 The far-infrared radio correlation (FIRC)

The far-infrared and radio emission of local galaxies are known to be tightly correlated

(Condon, 1992; Yun et al., 2001), which leads to the conclusion that they both trace recent star-formation activity in their host galaxy. The reasons why the thermal dust emission at far-infrared wavelengths should be so tightly coupled to the non-thermal radio emission are not clear. However the simplest explanations assume that UV radiation from the most massive stars are completely absorbed by dust and re-radiated in the far-infrared, these massive stars end their lives as supernovae explosions the remnants of which power synchrotron radio emission. The far-infrared and radio emission are thus both determined by the levels of massive star-formation taking place in the galaxy. This explanation, proposed by Voelk (1989), is known as the calorimeter argument as it assumes that all the energy from cosmic ray electrons accelerated by supernova remnants is converted to synchrotron radiation and all UV radiation is converted to far-infrared. Thus the galaxy is simultaneously an electron and UV calorimeter. It is only valid if the galaxy is optically thick to UV radiation and neglects both non-synchrotron cooling and proton losses. As non-synchrotron cooling results in a decrease in the proportion of energy converted to radio emission in high density starburst environments while proton losses will simultaneously increase the number of secondary electrons emitting synchrotron emission, these effects may act to balance each other out in high density environments maintaining a constant FIRC. In low density galaxies both the UV and electron calorimeter approximations no longer hold, decreasing both the radio and far-infrared emission (see e.g. Lacki et al., 2010; Lacki and Thompson, 2010). Maintaining a constant FIRC across a wide range of environments thus requires a great deal of detailed fine-tuning of the basic calorimeter model and the observed correlation remains largely unexplained.

The FIRC is known to hold over a wide range of luminosities and does not appear to evolve significantly out to higher redshifts (Ivison et al., 2010; Jarvis et al., 2010). Typically the correlation is expressed as logarithmic ratio $\mathrm{q_{IR}}$ between the total integrated far-infrared flux and the 1.4 GHz flux which has a mean value of $\sim$2.6 for star-forming galaxies. As the radio-loud jets of an AGN produce much higher levels of radio emission than is typical of a star-forming galaxy, objects whose $\mathrm{q_{IR}}$ ratios are significantly below this value are identified as AGN. Figure 1.3 illustrates the correlation between radio and infrared luminosities and the $\mathrm{q_{IR}}$ distribution of star-forming galaxies.

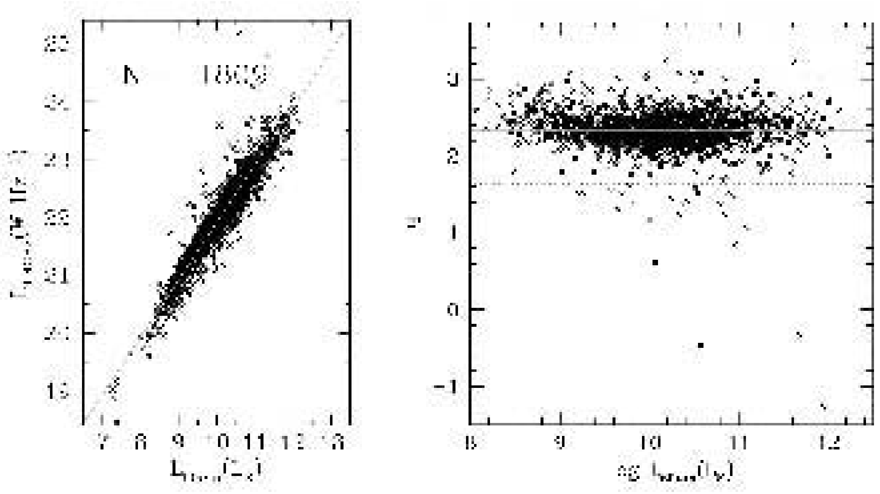

Figure 1.3: Left: The tight correlation between radio luminosity $L_{1.4\mathrm{GHz}}$ and far-infrared luminosity at 60 μm $L_{60\mu\mathrm{m}}$ in star-forming galaxies. Right: Distribution of $q_{60\mu\mathrm{m}}$, the logarithmic ratio of radio luminosity to far-infrared luminosity $q_{60\mu\mathrm{m}}=\log\frac{L_{1.4\mathrm{GHz}}}{L_{60\mu\mathrm{m}}}$ as a function of far-infrared luminosity. Figures taken from Yun et al. (2001).

2 Emission line ratios

The emission spectrum produced by an AGN is quite distinct from star-forming regions in an ordinary non-active galaxy. Baldwin et al. (1981) demonstrated that these objects occupy distinct regions of a diagram which plots the logarithmic ratio of the [OIII] to Hβ emission line strength versus the logarithmic line ratios of [NII] to Hα. This is commonly referred as the BPT diagram, the position of AGN and star-forming galaxies in such a diagram is illustrated in figure 1.4.

3 Colour relationships

Using galaxies detected in the Cosmic Evolution Survey (COSMOS) Smolčić et al. (2008) determined that the rest-frame optical colours of emission line galaxies are correlated with their positions in the BPT diagram and thus devised a colour based criteria to separate the AGN and star-forming galaxies out to redshifts of ~1.3. As spectroscopic observations require longer observing times than broad-band imaging for a given magnitude limit, such a colour based separation criteria is extremely useful when classifying large samples of faint objects for which follow up spectroscopy would prove prohibitively time consuming.

4 X-ray identifications

Padovani et al. (2009) have used X-ray luminosities to identify AGN based on the observations of Szokoly et al. (2004) that the majority of spectroscopically confirmed AGN in

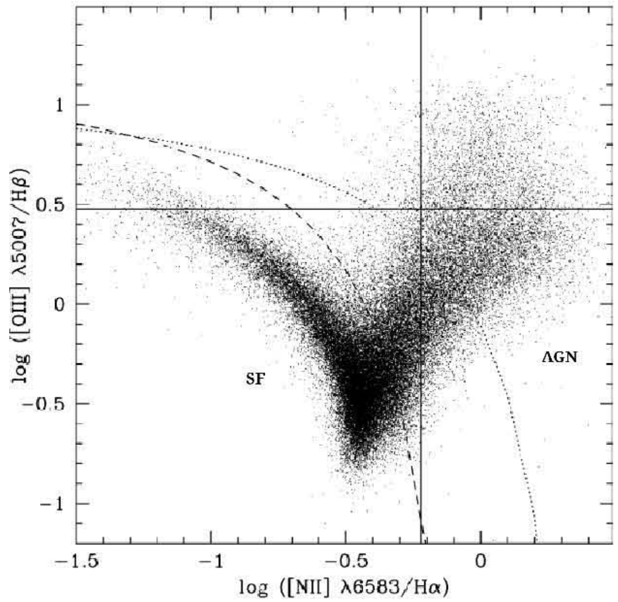

Figure 1.4: The BPT diagram, the dotted line represents the theoretical division between AGN and star-forming (SF) galaxies (Kewley et al., 2001) while the dashed line is an empirical determination of this separation (Kauffmann et al., 2003). Figure from Kauffmann et al. (2003).

the *Chandra* Deep Field South have hard X-ray luminosities $\geq 10^{42}$ erg s^{-1}. A number of authors have also suggested that star-forming galaxies exhibit a correlation between hard X-ray luminosity and radio luminosity (e.g. Bauer et al., 2002; Ranalli et al., 2003) which might be also be used to identify star-forming galaxies in a similar manner as the far-infrared radio correlation.

5 Radio morphology and spectral index

AGN in sub-mJy samples have been identified by their classic double lobed structure in radio images (Muxlow et al., 2005), however the requirement for sufficient resolution to resolve these structures clearly limits its applicability. With high enough spatial resolution AGN can also be identified based on the high brightness temperature of the emission. Star-forming galaxies and lobe-dominated AGN sources have spectral indices of α ~0.7 ($S_\nu \propto \nu^{-\alpha}$), which implies that spectral index is not a useful discriminant between these two populations. It is however able to identify core-dominated flat spectrum ($\alpha \sim 0$) AGN candidates.

6 4000Å break versus stellar mass normalised radio luminosity

Best et al. (2005b) devised a classification scheme based on the ratio of radio luminosity to stellar mass ($L_{1.4\mathrm{GHz}}/M_*$) and the strength of 4000Å break in the host galaxy. As radio luminosity in star-forming galaxies is correlated with star-formation rate both $L_{1.4\mathrm{GHz}}/M_*$ and the strength of the 4000Å break are loosely indicative of the specific star formation rate of the host galaxy. Radio-loud AGN produce excess radio emission compared to ordinary star-forming galaxes and thus their $L_{1.4\mathrm{GHz}}/M_*$ values will be greater than implied by the specific star formation rate indicated by the 4000Å break.

Due to the restrictions imposed by the depth and coverage of available complementary datasets it is also common to adopt some combination of these approaches to obtain the best possible characterisation of the sample (e.g. Seymour et al., 2008; Padovani et al., 2009). Recent results, after many years of intensive work in addressing the nature of the faint radio population, imply that AGN and star-forming galaxies each contribute ~50% at flux density levels of a few tens of μJy, with radio-quiet AGN accounting for ~50% of the faint radio AGN, i.e. ~25% overall (Simpson et al., 2006; Padovani et al., 2009).

1.3 *Evolution of radio sources*

The strong cosmic evolution of the most powerful radio sources was first deduced by Longair (1966). This work determined that power law evolution of the local luminosity function of powerful radio sources was necessary in order to reproduce the observed low frequency source counts. This evolution has since been confirmed by a number of investigations which imply that the co-moving space density of high luminosity radio sources has decreased by a factor of approximately 1000 between $z \sim 2$ and $z \sim 0$ (e.g. Laing et al., 1983; Dunlop and Peacock, 1990; Willott et al., 2001). Beyond $z \sim 2$ the evolution remains uncertain (e.g. Jarvis and Rawlings, 2000; Jarvis et al., 2001b) but appears to undergo a gradual decline (e.g. Wall et al., 2005; Rigby et al., 2011; Chhetri et al., 2012). Due to the increased difficulty in detecting the low-power radio sources up to even moderate redshifts the evolution of low-luminosity radio sources is considerably less well constrained, but early studies of the radio source counts indicated that they could not be evolving as strongly as their high luminosity counterparts (Longair, 1966; Doroshkevich et al., 1970).

Current studies of the cosmic evolution of low power radio sources appear to confirm that these sources experience only mild positive evolution out to redshifts of ~ 1.3. Clewley and Jarvis (2004) found little evidence that low luminosity radio sources with $L_{325\mathrm{MHz}} < 10^{25}$ W Hz^{-1} sr^{-1} were evolving out to redshift $z \sim 0.8$, their study also found evidence of luminosity dependent evolution taking place towards higher luminosities, with the strength of the evolution increasing with increasing luminosity. Sadler et al. (2007) find evidence of mild evolution out to $z \sim 0.7$ in their comparison of the radio luminosity function of sources in the 2dF-SDSS Luminous Red Galaxy and QSO (2SLAQ; Cannon et al., 2006) survey with that of sources in the 6 degree Field Galaxy survey (6dFGS; Jones et al., 2004), their study appears to rule out the no-evolution scenario. They find evidence of more rapid evolution towards higher luminosities, consistent with the results of Clewley and Jarvis (2004). Donoso et al. (2009) also find evidence of mild positive evolution in the $z = 0.1 \sim 0.55$ redshift range. These three studies make use of radio sources detected in the wide-area National Radio Astronomy Observatory (NRAO) Very Large Array (VLA) Sky Survey (NVSS; Condon et al., 1998) and the Faint Images of the Radio Sky at Twenty centimeters (FIRST; Becker et al., 1995) surveys whose flux density limits (≥1 mJy) are high enough to ensure that contamination from star-forming galaxies and radio-quiet AGN is low.

Smaller, deeper radio surveys have also been used to study the low-luminosity sources out to higher redshifts. These include studies in the Very Large Array (VLA) Cosmic Evolution Survey (VLA-COSMOS) field by Smolčić et al. (2009b), in the Lockman Hole *Spitzer* Wide-area Extragalactic legacy survey (SWIRE) field by Strazzullo et al. (2010), the *Chandra* Deep Field South by Padovani et al. (2011) and the *Suburu/XMM-Newton* Deep field by Simpson et al. (2012) which all find evidence of positive evolution of their low-luminosity AGN sources consistent with density enhancements ranging between $\sim 2 - 10$ at $z \sim 1.3$. These studies use different criteria to identify the AGN contribution in their sub-mJy samples which may contribute to small differences in their exact determinations of the strength of evolution taking place for these sources. Furthermore the survey sizes in these studies are all small, ranging from 2 to 0.1 degrees^2, thus cosmic variance is likely to contribute to variations in their findings. All of these studies imply that the level of evolution in the low power AGN is significantly less than that taking place in the high luminosity AGN. Two possible explanations of this observed separation in evolutionary behaviour have been put forward, the first being that evolution in the entire radio source population is luminosity dependent or that the radio source population is divided into two independently evolving components, a rapidly evolving high luminosity component and a lower luminosity component with much weaker evolution.

As both the morphological and accretion mode classification schemes divide the radio AGN population roughly according to their luminosities both the low luminosity FRI's (Jackson and Wall, 1999) and LERG's (Smolčić et al., 2009b; Best and Heckman, 2012) have been suggested as candidates for the slowly evolving component of the radio population. As the fundamentally different nature of the accretion taking place in LERG/HERG's has only recently been clarified, earlier work focused on determining whether the evolutionary behaviour of the FRI populations is significantly different to that taking place in the FRII's. Rigby et al. (2007) find evidence that high luminosity FRI sources evolve as rapidly as FRII sources of comparable radio power. Furthermore, Gendre et al. (2010) performed a detailed comparison of the radio luminosity function of FRI and FRII sources at a number of redshifts and revealed that both populations experience luminosity dependent number density enhancements at higher redshifts, $z \approx 0.8 \sim 2.5$, and that there are no significant differences between the enhancements measured for these two populations. These results would seem to suggest that both types of FR sources experience a similar evolutionary history when matched in radio luminosity and thus cannot fully account for the observed dichotomy in cosmic evolution.

The only work determining the evolution of a well defined sample of LERG and HERG galaxies is that of Best and Heckman (2012), which uses radio galaxies in the NVSS and FIRST surveys with counterparts in the Sloan Digital Sky Survey (SDSS; York et al., 2000) spectroscopic sample. The sources are classified on the basis of their detected emission lines. Their results indicate that LERG sources undergo little or no evolution while HERG sources at all luminosities appear to be strongly evolving, they speculate that as HERG sources are present in low numbers even at low radio luminosities they may be primarily responsible for the mild positive evolution detected in low luminosity samples in some earlier studies.

A further division in the evolutionary behaviour of radio-quiet and radio-loud AGN has been detected in the studies of Padovani et al. (2009) and Simpson et al. (2012) who find very little evidence of evolution in the low-luminosity radio-loud sources and evidence for stronger evolution in the radio-quiet AGN. This result is very interesting as it provides further evidence of a link between the radio-quiet AGN and the HERG sources which are believed to be powered by the same radiatively efficient “quasar” mode accretion as the HERG sources.

1.4 *The star-formation AGN connection*

Understanding the relationships between different classes of radio AGN, and their cosmic evolution, is important for improving our understanding of the broad and complex relationships that exist between AGN and star-formation activity in the universe. There are a number of indications that the formation and growth of galaxies may be closely linked to the growth of their central black holes. These include the tight correlations found between black hole mass and both stellar bulge mass (Kormendy and Richstone, 1995; Magorrian et al., 1998; McLure and Dunlop, 2002) and velocity dispersion (Gebhardt et al., 2000; Tremaine et al., 2002; Ferrarese and Merritt, 2000) in galaxies in the local universe. While on cosmological scales the increase in star-formation density at higher redshifts is accompanied by a corresponding increase in the number density of actively accreting supermassive black holes (Merloni et al., 2007).

Furthermore a long-standing difficulty with semi-analytic, hierarchical models of galaxy formation is that these models imply that galaxies form in hot hydrostatic haloes where the radiative cooling time of the gas is much shorter than the age of the system. Thus without further heating, cooling flows develop which channel gas to the centre of the galaxy triggering star formation and facilitating further accretion onto the supermassive black hole. In this scenario galaxies in the local universe should be more massive and have bluer colours and higher rates of star formation than is actually observed (e.g. White and Frenk, 1991). A related, similar problem is encountered on a larger scale in observations of the intracluster medium (ICM) of galaxy clusters where the X-ray emitting gas at the centre of clusters is observed to be much hotter than expected given the radiative cooling times of the system (see Voit and Donahue, 2005, for a review). Negative feedback from AGN has been invoked as the most likely candidate in the search for a mechanism to continuously reheat gas in both galaxies and clusters and disrupt the onset of these predicted cooling flows. In galaxies this disruption limits the growth of the supermassive black hole and halts or slows the formation of new stars. Such AGN feedback models might naturally account for the observed correlations in black hole mass and galaxy properties through a self regulation process which ties the growth of the galaxy to the growth of the black hole.

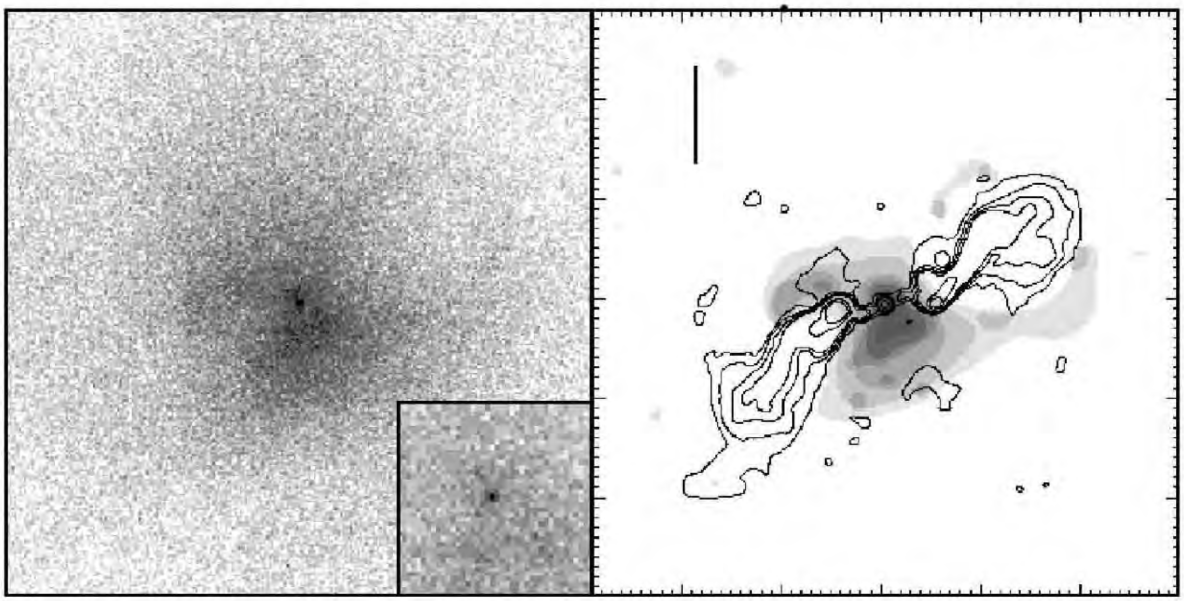

Figure 1.5: Radio jets in Hydra A aligned with low surface brightness regions in the X-ray image of the intracluster medium. On the left is the Chandra X-ray image of the central region of the cluster. On the right a smoothed version of the X-ray image is presented as a greyscale colourmap overlaid with contours representing the radio emission at 6 cm. The scale bar represents ∼20". Image taken from McNamara et al. (2000)

While in principle the large amounts of energy imparted by AGN to their neighbouring environments in the form of ionising radiation and relativistic jets should be more than sufficient to balance cooling losses the exact details of how this energy couples to the gas and influences the global properties of galaxies and clusters over a wide range of scales is unclear. Observationally the strongest direct evidence in support of AGN feedback is the presence of bubbles and cavities in the ICM of galaxy clusters which appear to be aligned with the axis of an AGN radio jet (McNamara et al., 2000; Fabian et al., 2003; Bîrzan et al., 2004). An example of such a radio jet induced cavity in the X-ray image is presented in figure 1.5. In cases where these cavities are observed in clusters without an AGN jet the assumption is that they were evacuated by a previously active, now dormant radio-loud AGN (e.g. McNamara et al., 2001).

As described above, AGN accretion occurs in two modes which each have a postulated associated mechanism of feedback which results in star-formation quenching. In the radiatively efficient "quasar" accretion mode, feedback occurs as a result of quasar driven winds which systematically remove gas from the galaxy, star-formation and accretion activity terminate abruptly as this process depletes their local fuel supply (Silk and Rees, 1998; Di Matteo et al., 2005). Observationally there is considerable evidence that such high speed ($\geq$ 1000 km s^{-1})

quasar driven winds exist (de Kool et al., 2001; Chartas et al., 2007; Rupke and Veilleux, 2011). Whether these winds are caused by heating or radiative pressure from the central AGN remains unclear, as is the potential efficiency of either of these types of winds in depleting the local fuel supply (see Cattaneo et al., 2009, for a review). Some radiatively efficient accretors are radio-loud and in these objects winds may also form due to shock acceleration by the relativistic jets (Best et al., 2000). It is tentatively speculated in the literature that this mode of accretion is predominantly fueled by cold gas supplied by gas rich mergers, this may help to explain the increased number density of radio-quasars and HERG's towards higher redshifts where the merger rate and gas fractions are higher than in the local universe (Best and Heckman, 2012).

In the radiatively inefficient "radio" accretion mode the bulk of the energy from the AGN is emitted as kinetic energy in jets, with very little radiative output from a central accretion disk. These sources accrete at much lower rates and consequently the total energy output from these AGN is lower than in the radiatively efficient case. However depending on how efficiently the kinetic energy in the jets is converted to heat in the interstellar gas these AGN may still have considerable potential to influence the star-formation properties of the galaxies they inhabit. It is this type of mechanical heating from an AGN jet that has been directly detected in the ICM of galaxy clusters. Using a scaling relationship between radio luminosity and mechanical heating power derived from such cluster observations Best et al. (2006) demonstrated that the time-averaged energetic output of "radio" mode accretors was indeed sufficient to counter cooling losses in massive, red galaxies. Furthermore semi-analytic models have successfully incorporated this "radio" mode feedback which are then able to better reproduce several features of the observed universe including the exponential cut-off in the bright end of the galaxy luminosity function (Croton et al., 2006; Bower et al., 2006). In this mode the AGN is fueled by direct accretion of the hot interstellar gas and is also the source of gas heating. As such AGN feedback in this mode has the potential to set up a stable feedback loop where the accretion rate is automatically adjusted by the available supply of hot gas (Allen et al., 2006; Best et al., 2006; Hardcastle et al., 2007).

Despite these arguments the true significance of such feedback processes is still largely unclear. Better observational constraints are required to make progress in answering fundamental questions about the relative importance of both "radio" and "quasar" mode accretors in shaping the global properties of the galaxies they inhabit. A key piece of evidence in resolving this question is thus an accurate determination of the cosmic evolution of the radio sources whose jets are speculated to be so profoundly influential.

1.5 *The future: upcoming radio surveys and their goals*

Multi-wavelength studies of the radio population in recent years have already made progress in addressing long-standing research questions such as the nature of the faint radio source population and the evolution of low-luminosity radio AGN. They have also provided the first evidence of a fundamental division in the radio AGN population which may have significance within the wider context of understanding the role of AGN feedback in determing the cosmic star-formation history of the universe. Large radio surveys such as the NVSS and FIRST in combination with the SDSS provide a great deal of insight into the properties of the low luminosity radio sources in the local universe yet they lack the depth to extend these studies out to high redshifts. While the sensitivity limits of the current generation of radio telescopes dictate that deeper surveys to flux density limits of tens of μJy are necessarily limited to very small areas ($\leq$ 2 degree^2). Current studies of sub-mJy samples are thus subject to cosmic variance which complicate the generalisation of their results to the entire radio population. Furthermore the ancillary datasets used for redshift estimation and source classification in these studies span a wide range of depths and wavelengths and the subsequent variations in their chosen classification procedures hinders direct comparisons of their results.

However a number of new radio continuum surveys are planned with upcoming, vastly more sensitive, SKA pathfinder telescopes which will overcome many of these limitations. These surveys include the Evolutionary Map of the Universe (EMU; Norris, 2011), Westerbork Observations of the Deep APERTIF Northern-Sky (WODAN) and the surveys to be conducted with the Low-Frequency Array (LOFAR; Röttgering et al., 2011)[1] which will map large areas of the sky ($\gtrsim$ 1000 sq degrees) to unprecedented depths ($5\sigma \simeq 10 - 50$ μJy). A detailed summary of the proposed areas and depths of these surveys is presented in table 1.1. Key astrophysical questions that these surveys will address include the cosmic star-formation history of the Universe out to z$\sim$2, the evolution of active galactic nuclei (AGN) to the edge of the

---

[1] www.strw.leidenuniv.nl/lofarsurveys

Table 1.1: Summary of areas and depths of upcoming radio continuum surveys with SKA pathfinder instruments.

Survey	Frequency (MHz)	Area (sq deg)	Depth 1σ (mJy)
LOFAR WIDE	15–40	20626	2.0
	40-60	20626	1.0
	120–180	20626	0.07
LOFAR DEEP	15–50	975	0.9
	40–60	1575	0.3
	120–180	566	0.015
LOFAR Ultra-DEEP	120–180	83	0.007
EMU WIDE	1400	$\geq$20000	0.010
EMU DEEP	1400	$\sim$30	0.001
WODAN WIDE	1400	$\geq$20000	0.010
WODAN DEEP	1400	$\sim$1000	0.005

universe as well as the influence of postulated AGN feedback mechanisms on star-formation activity and the formation and evolution of galaxies (Norris, 2011). The wide-field and source density of these surveys may be particularly suited to cosmological studies (e.g. Raccanelli et al., 2012; Camera et al., 2012). On the other hand, smaller area surveys with the eMERLIN (Muxlow, 2010), EVLA (e.g. Myers, 2010) and the future MeerKAT MIGHTEE surveys (Jarvis, 2011) will push to much deeper flux densities ($\lesssim 5\mu$Jy rms) to obtain a clear census of activity in the Universe up to higher redshifts, traditionally thought of as the realm of rest-frame optical and ultra-violet surveys. As radio observations are unaffected by dust extinction they have the potential to provide a dust-unbiased probe of the accretion and star-formation history of the Universe at these redshifts.

This thesis presents two new investigations of the evolution of low luminosity radio sources. The first of these, presented in chapter 2 is over an area of ~ 3 square degrees using a radio survey with a flux density limit of a few mJy and single-band photometric redshifts. While an improved investigation making use of a smaller, deeper radio survey and multi-band optical and near-infrared data is presented in chapter 4. As multi-wavelength data will be used extensively in future radio continuum surveys to classify the faint radio source population and to obtain redshift estimates through photometric redshift techniques, chapter 3 determines the efficiency of a widely used cross-matching technique, the likelihood ratio, in identifying faint counterparts to radio sources detected in these future surveys. Finally chapter 5 uses multi-band spectral energy distribution (SED) fitting techniques to classify and characterise the properties of faint radio sources. In chapter 6 I bring together these results and discuss possible future work in this area. This thesis assumes $H_0 = 70$ km s^{-1} Mpc^{-3}, Ω_m=0.3 and $\Omega_\Lambda = 0.7$ cosmology throughout.

Chapter 2 Evolution of radio sources

2.1 *Introduction*

Although the strong evolution of powerful radio sources out to redshifts of ∼2 has been established for many decades the seemingly much milder evolution of the less powerful radio sources is still the subject of active research, as is the origin of this apparent dichotomy in evolutionary behaviour. Determining the cosmic evolution of low-luminosity radio sources has taken on a renewed significance in light of recent suggestions that feedback from "radio" mode LERGs, rather than the powerful HERG sources, might play a significant role in switching off star-formation in massive galaxies particularly at low redshifts (see e.g. Best et al., 2006; Smolčić et al., 2009b). The LERG's constitute the dominant population of low luminosity radio AGN sources. In this chapter I use low frequency radio sources detected in the XMM-Large Scale Structure survey field to investigate the co-moving space density of low luminosity sources out to redshifts of ∼1. The low-frequency selection is preferred over high-frequency (e.g. geq1.4 GHz), as it provides an orientation independent selection, as the low-frequency detects the optically-thin lobe emission, whereas high-frequency surveys contain a higher fraction of pole-on sources where the optically thick core dominates (e.g. Jarvis and McLure, 2002).

The chapter is structured as follows: sections 2.2 and 2.3 discuss the radio and near-infrared (NIR) observations used in this analysis. Section 2.4 outlines the method used to cross match the radio sources with their infrared counterparts. In section 2.5 I describe the method used to obtain redshift estimates for the radio sources. Sections 2.6 and 2.7 discuss the $V/V_{\max}$ statistic used to evaluate cosmic evolution. In section 2.8 I determine the radio luminosity function of the low luminosity sources in the observed field and use it to investigate their evolution and finally I present my conclusions in section 2.9.

2.2 *Radio data at 610 MHz*

This analysis uses radio observations of the XMM-LSS field taken by Tasse et al. (2007). The full details of the observations as well as the imaging and calibration procedures used are discussed at length in their paper and in this section I highlight only some of the most relevant details. Their observations cover 13 degrees^2, centered at α(J2000)=$2^h24^m00^s$ and δ(J2000)=-$4°09'47''$, with 36 pointings of the Giant Metrewave Radio telescope (GMRT). The field was observed for a total of 18 h ($\sim$ 0.5 h per pointing) in August 2004 at a frequency of 610 MHz. The final mosaiced image has a resolution of $\sim$ 6.7$''$ and a non-uniform 5σ rms sensitivity ranging from 1.5 mJy to 2.5 mJy across the observed field.

I use the source parameters and original catalogue extracted from this image by Tasse et al. (2007). In order to exploit the full depth of the GMRT radio observations, whilst taking into account the non-uniformity of the noise distribution in the final image, Tasse et al. (2007) normalised the radio image with a background noise image prior to extracting a catalogue of sources with the AIPS Search and Destroy (SAD) task. Radio components with a peak value $>$5 in the noise normalised image were accepted as real and individual radio components were grouped into multiple component radio sources on the basis of the criteria that their individual components were separated by $<$60$''$. As they extracted 1024 individual radio components in the 13 square degree field Poissonian statistics predict that there is a less than 1% probability of the components being located within this distance of each other by chance. The final catalogue consists of 592 single component radio sources and 175 multi-component sources.

Tasse et al. (2007) associate their low frequency radio sources with 1.4 GHz sources in the NRAO VLA Sky Survey (NVSS; Condon 1998) when such sources are located within 45$''$ of the position of the low frequency source. The NVSS fluxes were used to obtain estimates or, in the case of non-detection in the NVSS, upper limits on the spectral indices of the sources, the NVSS has a 5σ flux limit of $\sim$2.5 mJy. Upper limits were determined assuming the 95% completeness limit of the NVSS survey. It should be noted that the spectral indices estimated by this method have large uncertainties for sources which are resolved in the 610 MHz survey as a result of the large mismatch in resolution at 610 (6.7$''$) and 1400 MHz (45$''$).

Positions of the NVSS counterparts were also used to estimate the overall positional accuracy of the 610 MHz catalogue. The calibration errors of the GMRT survey were found to be $\sigma_{\mathrm{GMRTra}} \lesssim 0.53''$ and $\sigma_{\mathrm{GMRTdec}} \lesssim 1.69''$, implying an overall accuracy of $\sim 2''$.

2.3 *K-band data*

I matched the radio sources detected in the XMM-LSS field with K-band sources detected in the 7th data release (DR7) of the ongoing UKIRT Infrared Deep Sky Survey (UKIDSS) (Lawrence et al., 2007). UKIDSS uses the Wide Field Camera mounted on the UK Infrared Telescope (UKIRT) (Casali et al., 2007). This survey, which began in May 2005, comprises 5 complementary sub-surveys of varying depths and sky coverage. This study uses data from the Deep eXtragalactic Survey (DXS) which is a deep, wide survey over four observed fields. The survey is aiming to cover 35 degrees^2 to a planned 5σ depth of $\mathrm{K}_{\mathrm{Vega}} \sim 20.8$ (see e.g. Kim et al., 2011). I used the online catalogue of sources in the XMM-LSS field, the sky coverage of this field in the 7th data release is illustrated in figure 2.1, the overlap in the DXS sky coverage and the radio observations is approximately 2.75 degrees^2. This data is complete down to $\mathrm{K}_{\mathrm{Vega}} = 19.2$ (Kim et al., 2011) and varies in depth across the observed field. Thus to ensure completeness I adopt a cut-off of $K_{\mathrm{Vega}} < 19.2$ for the optical counterparts to our radio sources. K-band magnitudes in the UKIDSS survey are calibrated in the Vega system described by Hewett et al. (2006).

2.4 *Radio and infrared matching*

For the purposes of identifying near-infrared counterparts to the radio data I divided the radio data into two categories. The first category comprises sources whose radio and optical emission are expected to be physically co-incident and includes all single component radio sources as well as partially resolved multiple component sources and double radio sources with clear radio cores. The second category contains sources where the optical emission is expected to be separated from the radio emission, and includes double radio sources with no detected radio core, radio jets and other complex multiple component structures.

To determine the optimal pairing radius for sources in the first category it is necessary to consider the accuracy of the radio and K-band source positions. The radio source positions in the GMRT catalogue are accurate to approximately $2''$ (see section 2.2) and the UKIRT

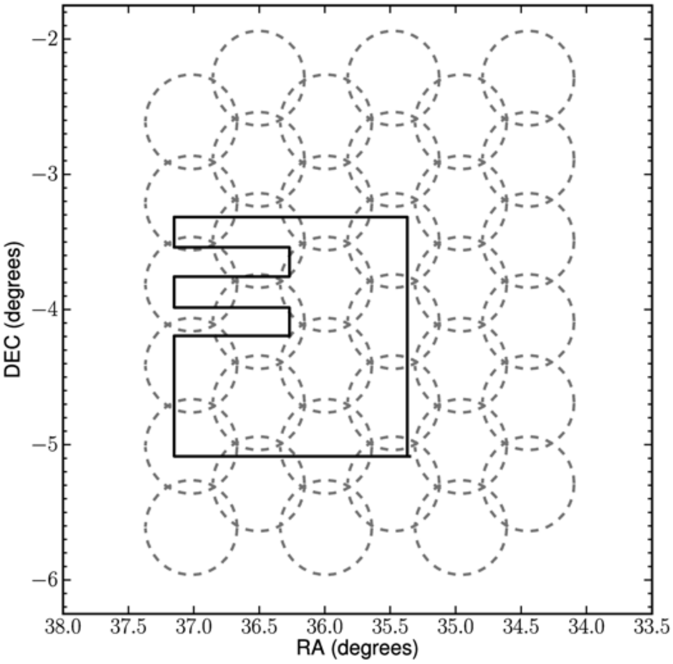

Figure 2.1: Location of the radio and infrared data used in this chapter. Light grey circles show the 610 MHz pointings of the GMRT. The thick black line indicates the UKIDSS DXS coverage of the XMM-LSS field in the 7th data release.

survey provides accurate astrometry to within $0.1''$ (Lawrence et al., 2007). I thus chose to adopt a pairing radius of $5''$, corresponding to roughly 2.5σ, where σ is the combined error in the positions of the radio and K-band sources. This large radius ensures relatively few true near infrared (NIR) counterparts will be located outside the chosen search area. Astrometric offsets between the radio and infrared datasets were removed prior to final matching.

As the surface density of NIR sources increases at fainter magnitudes there is an increasing probability that an unrelated NIR counterpart could appear within the adopted search radius by chance. To quantify the formal significance of a match between a radio source and a candidate NIR counterpart detected within the search radius I used the frequentist method of identification developed by Downes et al. (1986).

The Downes P-Statistic

The Downes et al. (1986) method calculates the probability that a NIR counterpart located at distance r from the radio source is simply a chance coincidence by correcting the raw Poissionian probability for the number of ways that such an apparently significant association could take place. These corrected probabilities are usually referred to as P-values.

To determine this corrected probability, Downes et al. (1986) begin by considering that the expected number of NIR counterparts with magnitude $\leq$ m, found within distance r of the radio source can be calculated from the surface density N_m of NIR objects with magnitudes $\leq$ m. It is simply given by the expression:

$$\mu = \pi r^2 N_m \tag{2.1}$$

The Poisson probability of at least one object brighter than m being found within the search radius is $P = 1 - \exp^{-\mu} \approx \mu$ for $\mu \ll 1$. If P$\ll$ 1 is then the object is unlikely to be a chance association. However Downes et al. (1986) make the point that that the probability of the object being the true counterpart is not simply $(1 - P)$ as for any given probability value P* the expected number of matches with P less than P* in a region defined by a finite search radius $\mathrm{r}_{\mathrm{max}}$ is :

$$E = P^* \left(1 + \ln\left(\frac{\pi r^2_{\mathrm{max}} N_{\mathrm{lim}}}{P^*}\right)\right) \tag{2.2}$$

where $\mathrm{N}_{\mathrm{lim}}$ is the surface density of objects brighter than the limiting magnitude of the survey. Thus given P* for an object the probability that it is a chance coincidence is calculated at $(1 - \exp^{-E})$. As is common practice I rejected all matches whose P-values were$>$ 0.05, in cases of two possible NIR matches with P-values $<$0.05 the match with the lowest P-value was accepted as the most likely counterpart.

Determining the optical counterparts of the more complex radio sources in our second category is less suited to statistical methods as a result of the much larger uncertainty in the expected position of the NIR counterpart. Therefore I determined the best match for sources in this category by overplotting the radio source contours on the near-infrared images and determining the most likely match by eye. The combination of the Downes et al. (1986) method and the visual inspections found matches brighter than K=19.2 for 131 sources out of a total of 213 radio sources detected in the DXS XMM-LSS field.

2.5 *Estimating redshifts*

I use a method of redshift estimation, developed by Cruz et al. (2007), which utilises the observed tight correlation between K-band magnitude and redshift for radio galaxies. This $K-z$ relation has been investigated for a number of radio galaxy samples including the 3CRR (Lilly and Longair, 1984), 6CE (Eales et al., 1997), 6C* (Jarvis et al., 2001a) and 7CRS samples (Willott et al., 2003) and continues to at least z=3 (Jarvis et al., 2001a).

The method developed in Cruz et al. (2007) uses a model of the distribution of radio galaxies as a function of redshift together with the linear $K-z$ relation to generate a Monte Carlo simulation of radio sources which populate a synthetic $K-z$ diagram. The advantage of this method over simply applying a linear fit to the $K-z$ relation is that it incorporates information about the observed scatter in this relationship and is thus able to provide a measure of the uncertainty in the output redshift estimates.

The distribution of radio galaxies and $K-z$ relation used in my simulations were based on the combined dataset of the 3CRR, 6CE, 6C* and 7CRS samples presented in Willott et al. (2003). Cruz et al. (2007) find the radio galaxies in this sample to be well fitted by a function of the form :

$$n(z) = A\exp\{-[\Sigma_{i=0}^{5} a_i(\log_{10} z)^i]^2\} \tag{2.3}$$

with polynomial coefficients : A=197.96; a_0=-0.39; a_2=1.00; a_4=1.47;
a_1=1.17; a_3=1.83; a_5=0.38.

Willott et al. (2003) quote the best fit to the $K-z$ relation in this combined sample as the second-order polynomial

$$K(z) = 17.37 + 4.53\log_{10} z + 0.31(\log_{10} z)^2. \tag{2.4}$$

The Monte Carlo simulations assume Gaussian deviations about a mean K-magnitude obtained from the $K-z$ relation. A constant dispersion for these deviations is adopted for the entire redshift range. I use the dispersion σ_k obtained by Cruz et al. (2007) via a fit to the same combined dataset used to obtain the $K-z$ relation. This dispersion was found to be σ_k=0.593.

The highly populated synthetic $K-z$ diagram generated by the Monte Carlo simulations can be used to obtain a photometric redshift probability density function for a source of any given K-band magnitude. This is achieved by extracting the redshifts of all the simulated sources in a narrow interval about the K-band magnitude in question. A fit to the distribution of these extracted redshifts provides the required probability density function. These distributions are best-fit by a $\log_{10}$-normal distribution with probability density function given by :

$$p(z|K) = \frac{1}{\ln(10) z \sqrt{2\pi\sigma^2}} \exp\{-\frac{[\log_{10}(z) - \mu]^2}{2\sigma^2}\} \tag{2.5}$$

where μ and σ are the mean and standard deviation for normally distributed random variable $\log_{10}(z)$. The best-fitting estimate for z is defined as

$$z_{est} = 10^{\mu} \tag{2.6}$$

and the asymmetric 68% confidence interval is defined as :

$$10^{\mu-\sigma} \leq z_{est} \leq 10^{\mu+\sigma} \tag{2.7}$$

The distribution of the estimated redshifts for all the radio sources in the survey with $K-$band counterparts is shown in figure 2.2. This distribution is compared with the redshift distribution predicted by the SKA Design Study (SKADS) simulations (Wilman et al., 2008, 2010) for a radio continuum survey with flux limits comparable to the survey used in this analysis.

This method of redshift estimation does not adjust for the possibility that optical host galaxy luminosity and radio luminosity may be correlated (e.g. Willott et al., 2003). This would most likely occur as a result of a correlation between both these properties with the mass of the central black hole. McLure et al. (2004) investigated the relationship between radio luminosity and black hole mass and concluded that these properties were only significantly correlated for the higher luminosity FRII and HERG sources, and the effect is relatively small. As this work is predominantly concerned with investigating the evolution of low luminosity sources this should not have a significant effect on the final conclusions.

Although using this method essentially precludes one from investigating any correlations between galaxy mass and radio emission, (e.g. Willott et al., 2003; McLure et al., 2004), it does allow the possibility of just using single band photometry to measure the evolution of radio sources, and is therefore much less telescope intensive than using multi-band photometry. This is particularly true if one wants to constrain the brighter end of the luminosity function, and are therefore driven to use larger survey areas. Recent work by Simpson et al. (2012) demonstrated that faint sub-mJy radio sources are systematically fainter than the $K-z$ relation by up to a magnitude, thus inferring redshifts for these sources from the $K-z$ relation results systematic overestimations of their redshifts. As the flux density limit of the Tasse et al. (2007) survey is $\geq$1.5 mJy this effect should not significantly bias the redshifts estimates used in this work.

2.6 $V/V_{\rm max}$

The evolution of the co-moving space density of sources in a complete sample can be assessed using the non-parametric $V/V_{\rm max}$ method (Rowan-Robinson, 1968; Schmidt, 1968). Here V is the cosmic volume enclosed by the object and $V_{\rm max}$ is the cosmic volume enclosed by the object if it were located at the redshift $z_{\rm max}$ where it's measured flux drops below the limit of the survey. This technique is useful as it does not require a priori assumptions about the form of the evolution taking place, furthermore the test easily incorporates a variety of selection criteria in the input surveys by considering the maximum and minimum observable redshift limits these criteria impose.

The test for evolution is straightforward as Schmidt (1968) demonstrates that in the case of a sample of objects uniformly distributed in space their $V/V_{\rm max}$ values will be uniformly distributed between 0 and 1 with a mean value of $\langle V/V_{\rm max}\rangle = 0.5\pm(12N)^{-\frac{1}{2}}$, where N is the number of objects in the sample. As such a mean value of $\langle V/V_{\rm max}\rangle > 0.5$ implies that the co-moving space density of sources increases at higher redshifts i.e. positive evolution with redshift whereas $\langle V/V_{\rm max}\rangle < 0.5$ indicates a decline in co-moving space density at higher redshift. As this work aims to investigate the less well-constrained evolution of the low luminosity radio sources I performed the $V/V_{\rm max}$ test on samples binned according to their radio luminosities.

2.6.1 *Calculating radio luminosity and radio* $z_{\rm max}$

To convert the observed radio fluxes at 610 MHz $F_{610}^{\rm obs}$ to the flux emitted at 1400 MHz $F_{1400}^{\rm em}$ I used the radio spectral indices estimated by Tasse et al. (2007), by comparison with the NVSS,

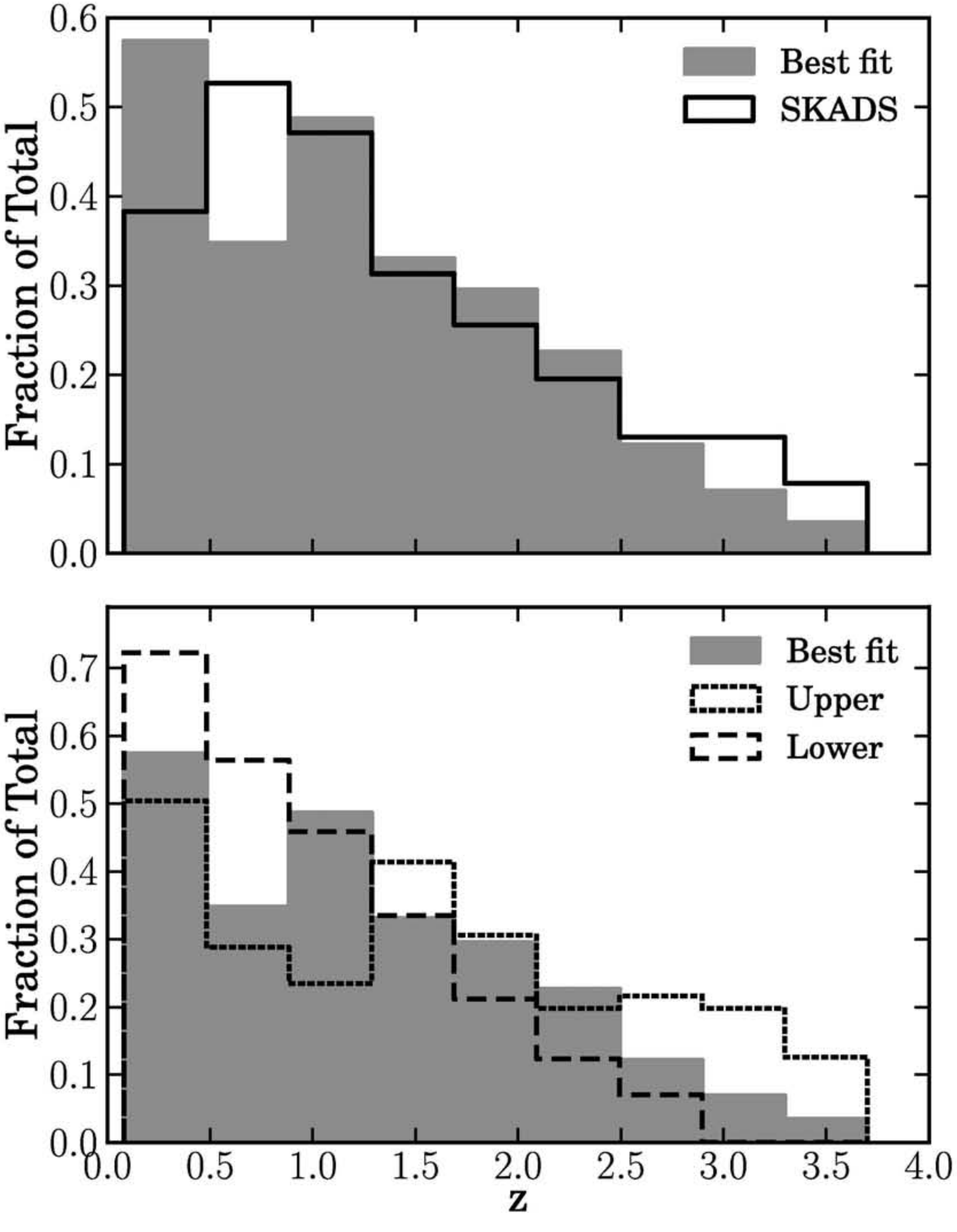

Figure 2.2: The distribution of the estimated redshifts of the matched NIR/radio sample. The top figure compares the best fit redshift estimates determined via the $K-z$ diagram to the theoretical redshift distribution in the SKADS simulations (Wilman et al., 2008) of a radio survey with the same flux limits as that described in section 2.2. The bottom figure compares the best fit distribution to the distributions which would occur if all the sources had redshifts corresponding to the upper and lower 68% confidence intervals of their predicted redshift.

and the standard relationship:

$$F^{\mathrm{em}}_{1400} = \left(\frac{1400}{610}\right)^{\alpha} (1+z)^{-(1+\alpha)} F^{\mathrm{obs}}_{610} \tag{2.8}$$

These emitted fluxes, measured in Jy, are converted to 1.4 GHz luminosities $\mathrm{L}_{1.4\mathrm{GHz}}$ in SI units of W Hz^{-1} sr^{-1} using the luminosity distance $\mathrm{D_L}$ as:

$$\mathrm{L}_{1.4\mathrm{GHz}} = 10^{-26} 4\pi D_{\mathrm{L}}^2 F^{\mathrm{em}}_{1.4\mathrm{GHz}} \tag{2.9}$$

The luminosity distance is calculated from the mean redshift of the radio source as:

$$\mathrm{D_L} = (1+\mathrm{z})\mathrm{D_H} \int_0^{\mathrm{z}} \frac{\mathrm{dz}'}{\sqrt{\Omega_{\mathrm{M}}(1+\mathrm{z}')^3 + \Omega_\Lambda}} \tag{2.10}$$

where $\mathrm{D_H}$ is the Hubble distance and Ω_M, Ω_Λ are the dimensionless density parameters of matter and the cosmological constant Λ respectively (e.g. Hogg, 1999). Having calculated the intrinsic 1.4 GHz luminosity of all the radio sources in the survey the relationships in equations 2.8 and 2.9 can be used to determine for any given 1.4 GHz luminosity the maximum redshift $z^{\mathrm{radio}}_{\mathrm{max}}$ which results in an observed 610 MHz flux greater than the survey limit. Radio luminosities calculated from these relationships are presented in figure 2.3.

2.6.2 *Calculating optical* z_{max}

The chosen method of redshift estimation, which relies on the $K-z$ relation, imposes the additional restriction that a source can only be included in the final sample used in the V/V$_{\mathrm{max}}$ test if its infrared counterpart is brighter than the magnitude limit employed in the cross-matching procedure. In order to determine z_{max} it is necessary to take into account this extra selection criteria. Therefore if $z^{\mathrm{radio}}_{\mathrm{max}}$ determined by the radio data is larger than the redshift $z^{\mathrm{opt}}_{\mathrm{max}}$ which would cause the source to drop out of the infrared survey then $z_{\mathrm{max}} = z^{\mathrm{opt}}_{\mathrm{max}}$, i.e. $z_{\mathrm{max}} = \min\{z^{\mathrm{opt}}_{\mathrm{max}}; z^{\mathrm{radio}}_{\mathrm{max}}\}$. I used the Monte Carlo simulations of the $K-z$ diagram to predict $z^{\mathrm{opt}}_{\mathrm{max}}$ and obtained a value of $z^{\mathrm{opt}}_{\mathrm{max}} = 2.5$ as the mean z corresponding to the limiting K-band magnitude of 19.2.

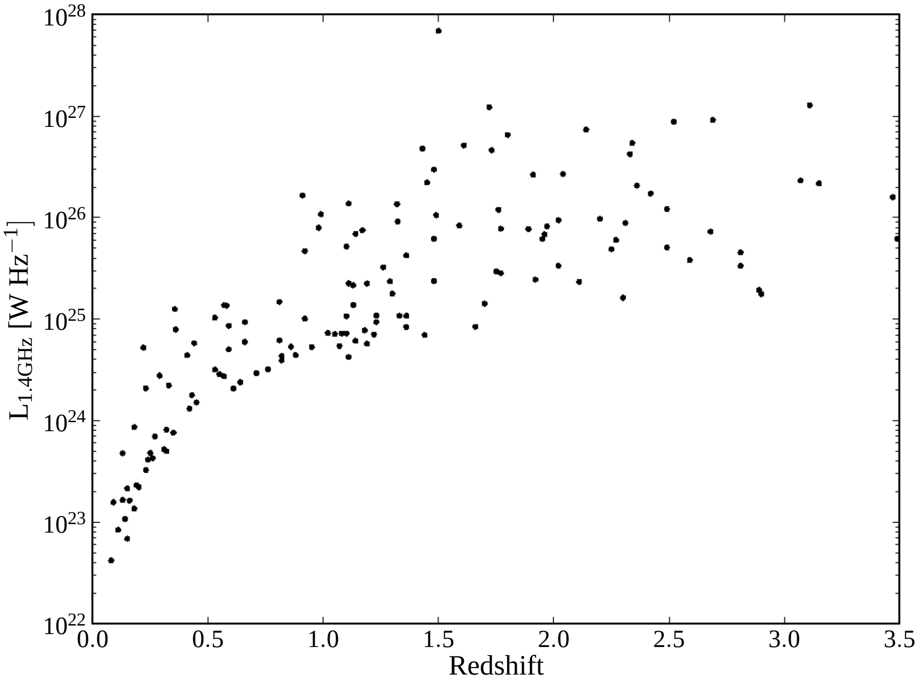

Figure 2.3: 1.4 GHz luminosity versus redshift for the radio sources in the XMM-LSS-DXS field.

2.6.3 *Generalised* $V_{\mathrm{e}}/V_{\mathrm{a}}$ *test*

The original $\langle V/V_{\max}\rangle$ test was formulated for a single sample complete above a given radio flux density and optical magnitude. However the radio survey used in this analysis is inhomogeneous in depth (Tasse et al., 2007), thus it is more appropriate to use the generalised $V_{\mathrm{e}}/V_{\mathrm{a}}$ test devised by Avni and Bahcall (1980) to analyse the evolutionary properties of this sample.

The method devised by Avni and Bahcall (1980) is completely general in that it can be applied to combine data from any number of surveys which may all have different flux density limits and whose survey areas may cover either separate, non-contiguous or overlapping regions of the sky. For clarity I present a brief description of the generalisation as it applies to the survey used in this chapter, namely a survey over a single contiguous region of sky with an inhomogeneous flux density limit. This survey can be represented by considering a survey over an area B with a flux density limit $\mathrm{F_B}$ where for some small sub-area of this survey, denoted as area C, the survey is slightly deeper and has a flux density limit $\mathrm{F_C}$ with $\mathrm{F_C} < \mathrm{F_B}$. This arrangement is represented schematically in figure 2.4. In this scenario a source could be included in the survey by either being detected in the region of sky B-C at a redshift which is $< z^B_{\max}$ defined by the flux limit F $_{rmB}$ or it may be detected in region C with z$< z^C_{\max}$. Thus

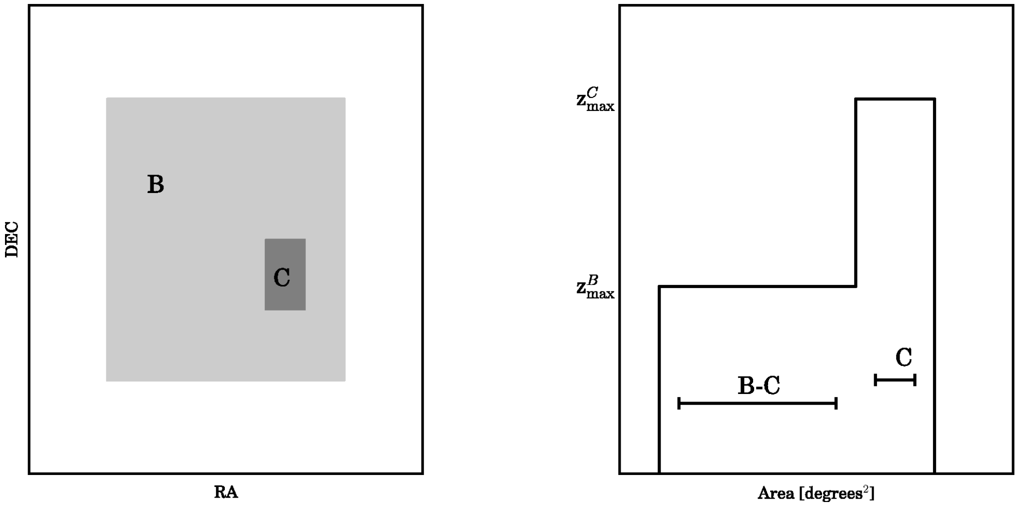

Figure 2.4: Left: Schematic representation of a survey with an inhomogeneous depth, where some part of the full survey region B, labelled region C has a slightly deeper flux limit. Right: A schematic representation of the cosmic volume available to a source detected in the inhomogeneous survey represented in the left plot.

the combined total volume of space available to a source detected in the survey is given by the expression:

$$V_{\mathrm{a}} = \frac{\Omega_{B-C}}{4\pi} V(z^{B}_{\mathrm{max}}) + \frac{\Omega_{C}}{4\pi} V(z^{C}_{\mathrm{max}}) \tag{2.11}$$

where $\Omega_{\mathrm{B-C}}$ and $\Omega_{\mathrm{B-C}}$ are the solid angles subtended by regions B-C and C on the sky and $V(z^{B}_{\mathrm{max}})$, $V(z^{C}_{\mathrm{max}})$ represent the total cosmic volumes of the universe at redshifts $z^{\mathrm{B}}_{\mathrm{max}}$ and $z^{\mathrm{C}}_{\mathrm{max}}$. The total volume enclosed by a source depends on whether its observed redshift is greater or less than $z^{\mathrm{B}}_{\mathrm{max}}$ and given by the expression:

$$\begin{aligned} V_{\mathrm{e}}(z) &= \frac{\Omega_{B-C}}{4\pi} V(z) + \frac{\Omega_{C}}{4\pi} V(z) && z \leq z^{B}_{\mathrm{max}} \\ V_{\mathrm{e}}(z) &= \frac{\Omega_{B-C}}{4\pi} V(z^{B}_{\mathrm{max}}) + \frac{\Omega_{C}}{4\pi} V(z) && z \geq z^{B}_{\mathrm{max}} \end{aligned} \tag{2.12}$$

The total available and enclosed volumes are represented schematically in figures 2.4 and 2.5 respectively.

It is straightforward to see how the analysis above can be extended to the case of multiple subregions within survey area B with a range of increasingly deep flux density limits, as is the case for a radio survey with non-uniform noise coverage. The generalised test thus defines two new test variables the enclosed volume V_{e} and the available volume V_{a} which are calculated by

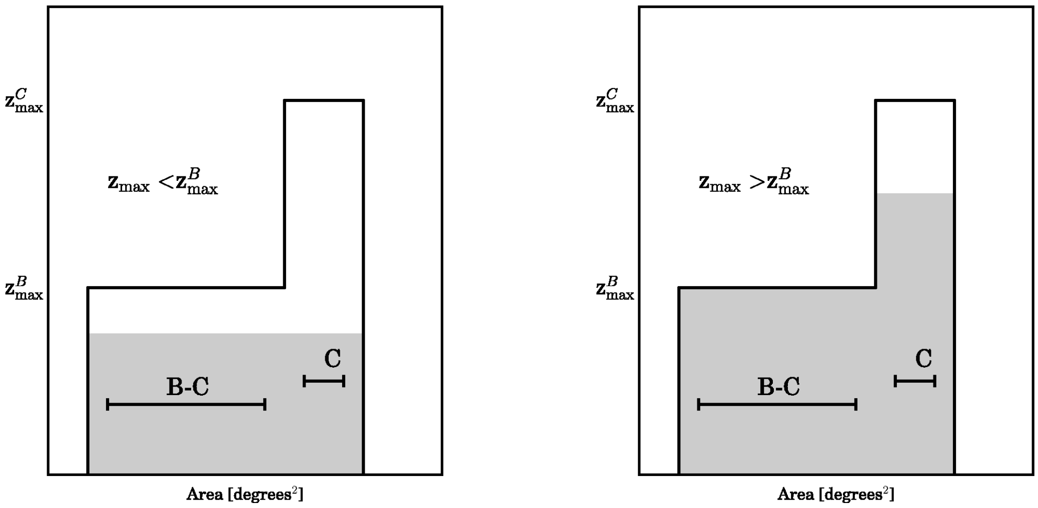

Figure 2.5: Schematic representation of the volume enclosed by a sources whose $z_{\rm max}$ is $< z_{\rm max}^{B}$ (left) and $> z_{\rm max}^{B}$ (right)

combining the total and maximum cosmic volumes defined by the areas and flux density limits of these subregions. As the statistical properties of the new $V_{\rm e}/V_{\rm a}$ variable are identical to those of the original $V/V_{\rm max}$ variable in a single flux-limited sample, evidence of cosmic evolution can once more be inferred by evaluating the mean $< V_{\rm e}/V_{\rm a} >$ of the sample in question (Avni and Bahcall, 1980).

To determine the effective survey area as a function of radio flux density I perform a simple simulation. I inject 1000 radio sources with peak flux densities ranging from 1-4 mJy into the original map of the radio data. These simulated sources are restricted to the 2.75 degrees^2 covered by the DXS survey and I determine the fraction of these simulated sources which are recovered by the source extraction algorithm SAD in the Astronomical Image Processing Software (AIPS) as a function of their input flux densities. This fraction is used to derive the effective survey area at a range of flux density limits and the corresponding available and enclosed volumes as per equations 2.11 & 2.12.

2.7 *$V/V_{\rm max}$ results*

In figure 2.6 I compare the mean $V_{\rm e}/V_{\rm a}$ statistics obtained for the XMM-LSS-DXS sample with those found in Clewley and Jarvis (2004). The results are in good agreement with their analysis which is based on galaxies selected at 325 MHz in the Sloan Digital Sky Survey. The

Table 2.1: Results of $\langle V_{\mathrm{e}}/V_{\mathrm{a}}\rangle$ analysis is seven luminosity bins. The column entitled 1σ (MC) quotes the uncertainty in the $\langle V/V_{\mathrm{max}}\rangle$ estimates due to the uncertainty in the $K-z$ derived redshift estimates. The last column gives the mean z of sources in each bin.

$L_{1.4\mathrm{GHz}}$ [W Hz^{-1}]	$\langle V_{\mathrm{e}}/V_{\mathrm{a}}\rangle$	1σ	1σ (MC)	$\langle z\rangle$
23.5-24	0.52	0.09	0.07	0.26
24-24.5	0.40	0.09	0.06	0.47
24.5-25	0.55	0.05	0.04	0.91
25-25.5	0.46	0.06	0.04	1.2
25.5-26	0.55	0.06	0.05	1.7
26-26.5	0.53	0.08	0.06	1.7
26.5-27	0.69	0.10	0.07	1.9

results also compare very well with the V/V_{max} results of Tasse et al. (2008). Their analysis is based on a combination of 325 MHz and 610 MHz radio sources in the XMM-LSS field. The radio data used in the Tasse et al. (2008) analysis overlaps the DXS field studied in this work [1], they do not however use DXS near-infrared data, so it is encouraging that I obtain a similar result. The strong evolution of the high luminosity radio sources detected by Clewley and Jarvis (2004) is also in evidence in figure 2.6 although this result is at a lower statistical significance due to the small size of the GMRT sample, similarly there is little evidence that the low power sources are evolving with cosmic time.

As discussed in section 2.5, there is some uncertainty in the redshift estimates used in this analysis due to the inherent scatter in the $K-z$ relation. To characterise the effect of this source of error on the $V_{\mathrm{e}}/V_{\mathrm{a}}$ estimates I used Monte Carlo methods. In these Monte Carlo simulations each source is assigned a redshift estimate determined by the redshift probability density function derived from its K-band magnitude. These simulated redshifts are used to rederive the $\langle V_{\mathrm{e}}/V_{\mathrm{a}}\rangle$ in the seven luminosity bins in figure 2.6. This process is repeated 1000 times to obtain the 68% confidence interval of the $V_{\mathrm{e}}/V_{\mathrm{a}}$ estimates. This confidence interval is indicated in table 2.1. The size of this source of error is comparable to the statistical errors due to the sample size.

To further investigate this evolutionary behaviour I determine the banded $V_{\mathrm{e}}/V_{\mathrm{a}}$ statistic in two luminosity bins. A high luminosity bin corresponding to sources with $L_{1.4\mathrm{GHz}} > 10^{25}$ W Hz^{-1} and a low luminosity bin with $L_{1.4\mathrm{GHz}} < 10^{25}$ W Hz^{-1}. The banded test calcu-

---

[1] A comparison between redshifts estimated via the K-z relation in this work and multi-band photometric redshifts used by Tasse et al. (2008) is presented in appendix A

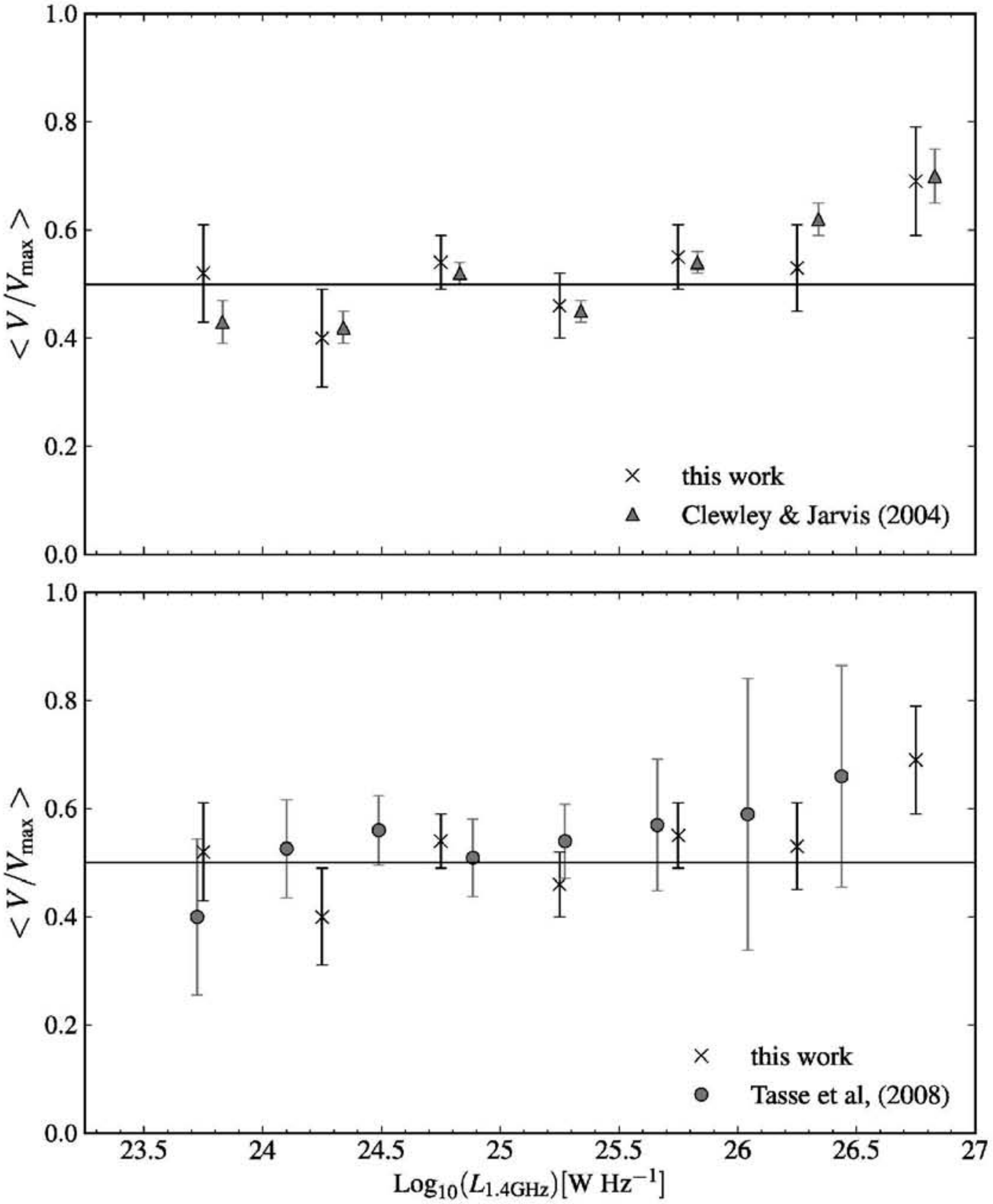

Figure 2.6: Average $V/V_{\max}$ in seven different radio luminosity bins compared to the results obtained in Clewley and Jarvis (2004) (top) and Tasse et al. (2008)(bottom).

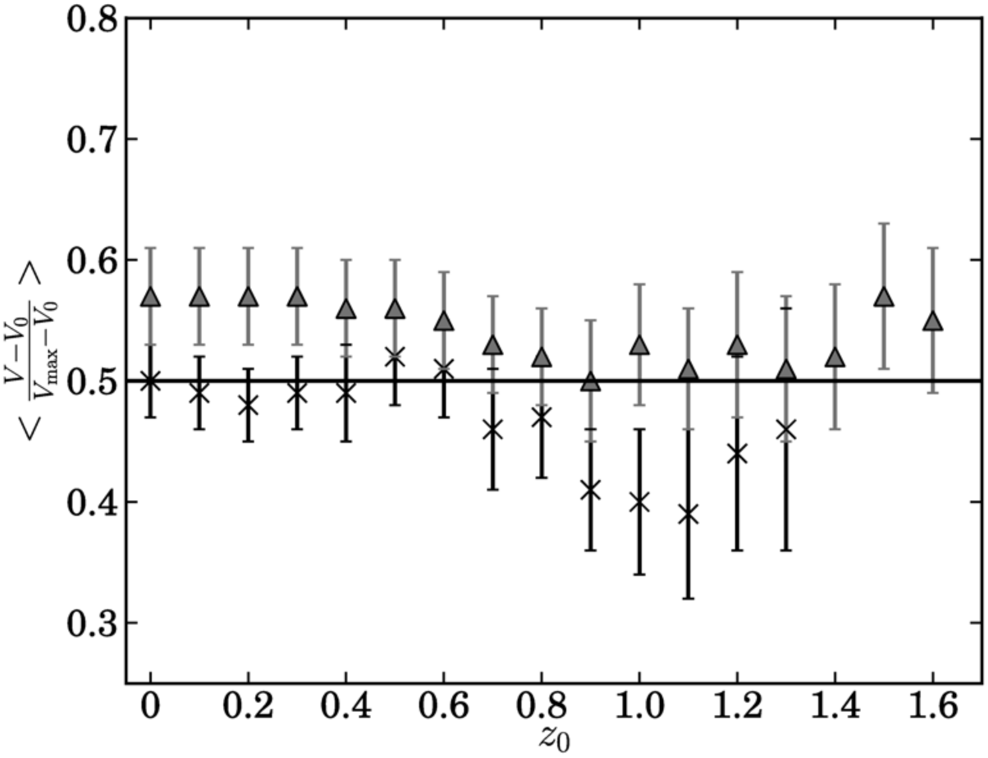

Figure 2.7: The banded $V/V_{\rm max}$ in two luminosity bins. The bin with $L_{1.4\rm GHz} > 10^{25}$ W Hz^{-1} is represented by grey triangles and the black crosses represent the $L_{1.4\rm GHz} < 10^{25}$ W Hz^{-1} bin.

lates the mean $V_{\rm e}/V_{\rm a}$ for all sources with $z > z_0$ for a range of z_0 values. All evolution below z_0 is thus masked out of the analysis allowing one to determine whether the evolution of these two populations of radio sources changes as a function of redshift. The results of the banded test are presented in figure 2.7. The error in the banded test as a result of the uncertainty in the $K - z$ redshift estimates is also calculated using Monte Carlo methods and presented in table 2.2.

The results in figure 2.7 indicate that there is little evidence of evolution in the low power radio sources out to a redshift of $z \sim 0.8$. Beyond this redshift there is a slight decline in the average $V_{\rm e}/V_{\rm a}$ of this population however the errors derived from the Monte Carlo estimates increase significantly at these higher redshifts. The stronger evolution of the high luminosity sources can also be seen in this figure. The mean $V_{\rm e}/V_{\rm a}$ for the low and high luminosity bins is calculated as 0.5 ± 0.03 and 0.57 ± 0.04 respectively in the redshift interval $0 \leq z \leq 2.5$.

Table 2.2: Results of the banded $\langle V_{\rm e}/V_{\rm a}\rangle$ test. The columns entitled 1σ (MC) list the Monte Carlo estimates of the error in the $\langle V_{\rm e}/V_{\rm a}\rangle$ estimates due to scatter in the $K-z$ relation.

	$L_{1.4\rm GHz} < 10^{25}$ W Hz^{-1}			$L_{1.4\rm GHz} > 10^{25}$ W Hz^{-1}		
z_0	$\langle V_{\rm e}/V_{\rm a}\rangle$	1σ	1σ(MC)	$\langle V_{\rm e}/V_{\rm a}\rangle$	1σ	1σ (MC)
0	0.50	0.03	0.02	0.57	0.04	0.02
0.2	0.48	0.03	0.02	0.57	0.04	0.02
0.4	0.49	0.04	0.04	0.56	0.04	0.03
0.6	0.51	0.04	0.05	0.55	0.04	0.03
0.8	0.47	0.05	0.07	0.52	0.04	0.03
1.0	0.40	0.05	0.14	0.53	0.05	0.04
1.2	0.44	0.08	0.24	0.53	0.05	0.05
1.4				0.52	0.06	0.05
1.6				0.55	0.05	0.06

2.8 *The radio luminosity function*

Another standard means of quantifying the cosmic evolution of radio sources is to compare the measured Radio Luminosity Function (RLF) of these sources at different cosmic epochs. Changes in the luminosity function $\Phi_z(L)$ are usually modelled as being due to one of two simplified evolution scenarios, either pure density evolution (PDE) or pure luminosity evolution (PLE). In pure density evolution the luminosity distribution of the radio sources is considered fixed while the number density of radio sources changes with redshift. In this scenario the measured luminosity function at a given redshift $\Phi_z(L)$ is related to the local luminosity function $\Phi_0(L)$ via the following equation :

$$\Phi_z(L) = (1+z)^{\alpha_D}\Phi_0(L) \tag{2.13}$$

In pure luminosity evolution the radio sources undergo a change in their luminosity with time, this evolution is parameterized as:

$$\Phi_z(L) = \Phi_0\left(\frac{L}{(1+z)^{\alpha_L}}\right) \tag{2.14}$$

I calculate the $\Phi_z(L)$ of the radio sample in four redshift bins using the standard $1/{\rm V}_{\rm max}$ method of Schmidt (1968). Thus the RLF and its corresponding error is calculated for a particular luminosity bin as:

$$\Phi(L) = \sum_{j=1}^{N} \frac{1}{V_{\mathrm{max}}^{j}} \qquad\qquad \sigma = \sqrt{\sum_{j=1}^{N} \left(\frac{1}{V_{\mathrm{max}}^{j}}\right)^{2}} \tag{2.15}$$

where the j index runs over all sources in the luminosity bin L-ΔL →L+ΔL. The V$_{\mathrm{max}}$ values are adjusted to take into account the redshift limits of the four redshift bins for which the luminosity functions were calculated. The results of this determination of the RLF are presented in figure 2.8 and compared with the RLF of radio sources in the VLA-COSMOS survey derived by Smolčić et al. (2009b). The luminosity function estimates appear to be in good agreement with the results of this previous study.

Smolčić et al. (2009b) characterise the evolution of the radio sources in the VLA-COSMOS survey by adopting the RLF given by Sadler et al. (2002) as the best representative model of their measured local luminosity function and using a least squares fit to derive the α_D and α_L parameters for pure density and pure luminosity evolution of this RLF. The analytic form of the RLF given in Sadler et al. (2002) was obtained from radio galaxies in the NVSS survey matched with optical counterparts in the 2dF Galaxy Redshift Survey. It is given as :

$$\Phi(L) = \Phi^{*} \left[\frac{L}{L^{*}}\right]^{1-\alpha} \exp\left\{\frac{1}{2\sigma^{2}}\left[\log\left(1+\frac{\mathrm{L}}{\mathrm{L}^{*}}\right)\right]^{2}\right\} \tag{2.16}$$

where α=1.58,σ=1,Φ^{*}=7.6×10^{-6} Mpc^{-3} and L^{*}=2.1×10^{2} W Hz^{-1}.

The fitting procedure of Smolčić et al. (2009b) yielded estimates of $\alpha_D = 1.1 \pm 0.1$ and $\alpha_L = 0.8 \pm 0.1$ where the errors were derived from the distribution of χ^2 in the least squares fit. Employing this same method we obtain values for the density and luminosity evolution parameters of $\alpha_D = 0.6 \pm 0.1$ and $\alpha_L = 0.8 \pm 0.2$. These estimates are fairly consistent with the estimates of Smolčić et al. (2009b) and imply an increase in the co-moving space density of low luminosity radio sources by a factor of ~ 1.5 in the interval between z=0 − 0.8.

The consistency of these results with those of Smolčić et al. (2009b) provides encouraging evidence that the $K - z$ relation can be used to investigate the radio luminosity function. This could provide a useful alternative technique for studying the RLF in the absence of multi-band photometric redshift estimates.

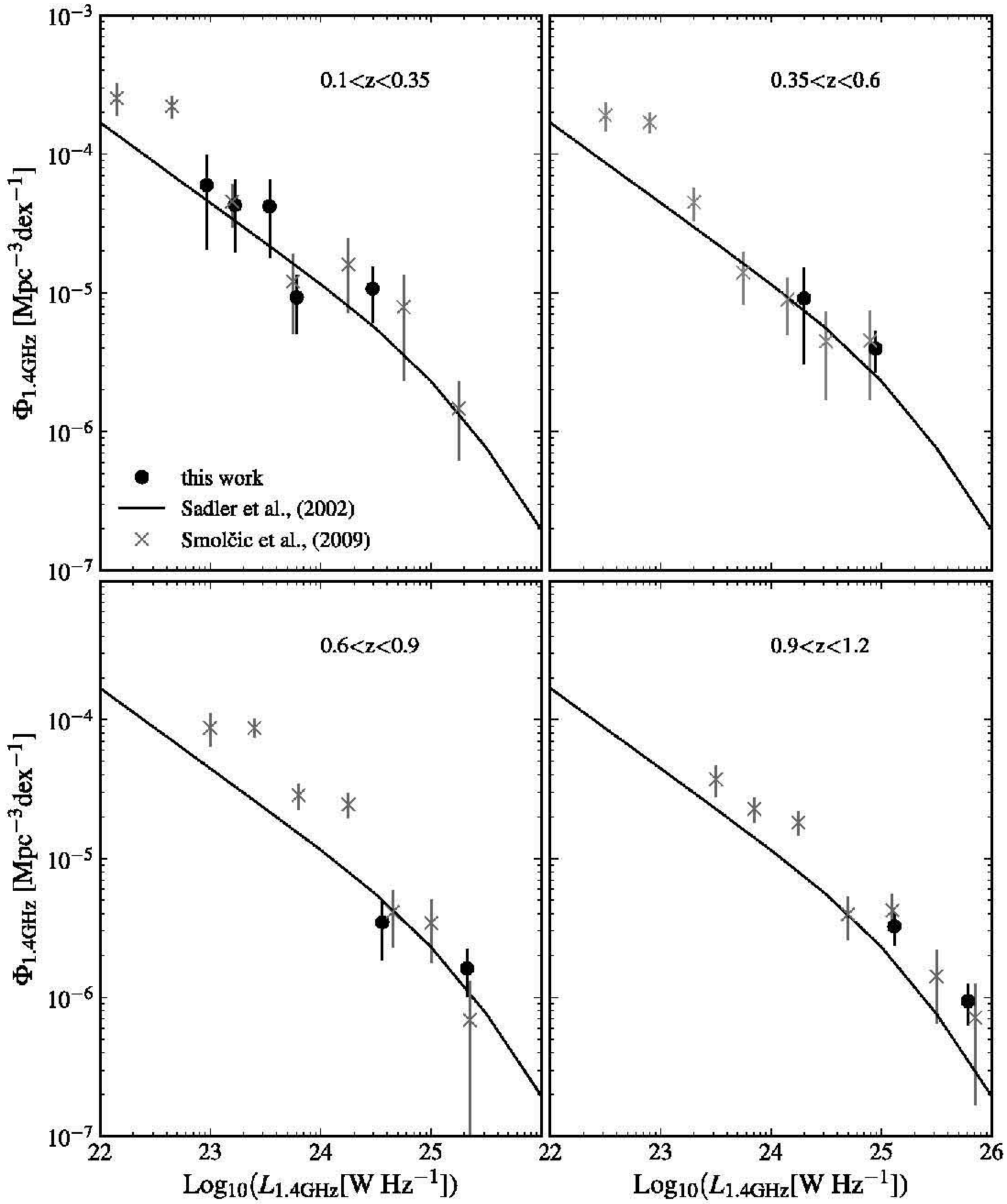

Figure 2.8: The measured radio luminosity function in four redshift bins compared to the results of Smolčić et al. (2009b). The solid line represents the analytic form of the local luminosity function derived in Sadler et al. (2002).

2.9 *Conclusion*

I have used the non-parametric V/V_{max} test and the radio luminosity function to investigate the cosmic evolution of low power radio sources in the XMM-LSS field. Previous investigations of the evolution of low-power radio AGN have found evidence of no evolution (Clewley and Jarvis, 2004; Padovani et al., 2011) or mild evolution taking place in the redshift range $z = 0 - 1.3$. Donoso et al. (2009) find that the co-moving density of low luminosity sources ($L_{1.4\mathrm{GHz}} < 10^{25}$ W Hz^{-1}) in the MegaZ-Luminous Red Galaxy catalogue increases by a factor of 1.5 between $z = 0.1 - 0.55$. Similarly Sadler et al. (2007) find evidence that low luminosity sources experience mild evolution with an increase in their number density by a factor of $\sim$2 at z=0.55. This is significantly less than the strong evolution detected in the high power radio sources whose number densities are enhanced by a factor of 10 in the same cosmic timeframe. The results of Sadler et al. (2007) seem to rule out the no-evolution scenario. Smolčić et al. (2009b) find mild evolution of the low power AGN in the VLA-COSMOS survey out to $z \sim 1.3$, as did Strazzullo et al. (2010) in the Deep SWIRE field and Simpson et al. (2012) also see evidence of positive evolution taking place out to $z \sim$1. In light of the possibly significant role that difference types of AGN phenomena have to play in regulating galaxy formation and growth via AGN feedback mechanisms there is considerable interest in trying to determine whether different sub-classes of low luminosity radio AGN have different evolutionary behaviours. Detailed investigations of the radio-quiet and radio-loud AGN have been undertaken by Simpson et al. (2012) and Padovani et al. (2011) which imply that the radio-quiet AGN are predominantly responsible for the observed mild evolution between z=$0-1$ and that the low luminosity radio-loud sources experience much less or even no evolution in this interval. Recent work by Best and Heckman (2012) determined that there is little evidence of evolution for the LERG sources while HERG sources appear to experience strong evolution at all luminosities. While Gendre et al. (2010) find evidence that higher luminosity, $L_{1.4\mathrm{GHz}} \geq 10^{24.5}$ W Hz^{-1} FRI sources increase their space density by a factor of $\approx$ 10 in the interval z= 0.8 $\sim$ 1.5, which is comparable to the level of evolution seen in FRII sources at similar luminosities. The division in the FRI/FRII classification system and the LERG/HERG system occurs at roughly the same luminosity threshold of $L_{1.4\mathrm{GHz}} \sim 10^{25}$. As the analysis in this chapter categorises radio sources solely on their luminosity I am unable to determine how the observed separation in evolutionary behaviour relates to the evolution of the underlying subclasses of radio sources including FRI/FRII's and HERG/LERG's and to make comparisons with these more detailed investigations.

However the results are broadly consistent with previous works which consider a single population of low-luminosity AGN and imply density enhancements by a factor ~ 1.5 at z=0.8. There is also evidence that the low power radio AGN are evolving more slowly than their high power counterparts in the redshift range $z = 0 - 0.8$ and tentative evidence that this separation in evolutionary behaviour persists to $z = 1.2$. It is possible that this luminosity dependent behaviour results from a changeover in the dominant population of radio-AGN with weakly evolving LERG sources and strongly evolving HERG sources comprising the dominant contributors at low and high luminosities respectively.

The results demonstrate that using the $K-$band (or similar wavelength), combined with radio surveys, is a viable route to investigating the evolution of the radio source population, at least up to $z \sim 1.2$. In the future, all-sky radio surveys such as those carried out with the Low-Frequency Array (LOFAR; Morganti et al., 2010; Röttgering et al., 2011) and the Australian Square Kilometre Array Pathfinder (ASKAP; Johnston et al., 2008) telescope, combined with the UKIDSS Large Area Survey (LAS; Lawrence et al., 2007) and the VISTA Hemisphere Survey, as well as Wide-field Infrared Survey Explorer (WISE; Wright et al., 2010), will enable us to pin down the evolution of the radio source population to a much higher degree of accuracy.

However the analysis is limited by the relatively low fraction of radio sources with identified counterparts ($\sim 60\%$) and the large uncertainties associated with redshifts estimated via the $K - z$ relation and would benefit greatly from more accurate redshift estimates in the form of either spectroscopic or multi-band photometric redshifts. Thus in order to obtain better constraints on the evolution of the radio luminosity function the next chapters match radio sources with deep multi-band optical and near-infrared data which have been used to derive very accurate photometric redshifts.

Chapter 3

Cross-matching

With the ultimate goal of extending my investigation of low-luminosity radio sources this chapter identifies optical and near-infrared (NIR) counterparts to deep VLA radio observations complete to a flux density limit of $S_{1.4\mathrm{GHz}} \sim 100\mu$Jy. The greater depth of these radio observations will allow me to extend the RLF beyond the $z \sim 1$ limit imposed by the shallower GMRT data in chapter 2. However identifying counterparts to lower resolution radio observations becomes an increasingly complex problem as the depth of the multi-wavelength ancillary dataset increases. This can be understood by considering that the resolution and signal to noise ratio of the radio observations determines a lower limit on the positional accuracy of the faint radio source positions dictating that their true counterparts might be located anywhere within this positional uncertainty. However as the source density of the increasingly faint ancillary datasets increases, a large number of faint sources will be located within this search area by chance. Nearest neighbour matching techniques are thus no longer adequate when the surface density of faint sources is such that a significant number of these unrelated background sources are expected to be located within a search area comparable to the positional uncertainty of the radio observations. A method which is often used to identify counterparts to low resolution radio observations is the Likelihood Ratio (LR) technique. This technique was first developed by Richter (1975) and later expanded upon by de Ruiter et al. (1977); Sutherland and Saunders (1992) and Ciliegi et al. (2003) The method combines information about the brightness distribution of the complementary higher resolution data and the positional errors in both the radio source catalogue and the complementary dataset to determine the most likely counterpart. In this chapter I thus use the LR technique to associate the faint radio sources in the 100μJy limited survey with their counterparts in the VIDEO survey in preparation for the determination of the RLF in chapter 4.

Multi-wavelength ancillary datasets will also play a vitally important role in the upcoming radio-continuum surveys with SKA pathfinder telescopes, including the EMU, WODAN and MIGHTEE surveys. These surveys will probe to μJy levels where the radio population is composed of a mixture of star-forming galaxies and AGN. The relative fraction of AGN and star-forming galaxies present at these low flux densities is not well-determined but observational studies and extrapolations of the radio luminosity functions of both populations indicate that AGN constitute a significant fraction (up to 50%) of the radio source population even at levels of ten's of μJy (Sadler et al., 2002; Jarvis and Rawlings, 2004; Simpson et al., 2006; Seymour et al., 2008; Kellermann et al., 2008; Padovani et al., 2009; Padovani et al., 2011). Thus there is no observational regime in which one can assume a faint radio source is simply associated with a starburst galaxy, and complementary datasets at optical and infrared wavelengths will play a vital role in classifying these faint radio sources. Furthermore, optical and near-infrared imaging are crucial for providing redshift estimates of radio sources through photometric redshift techniques (e.g. Benítez, 2000; Mobasher et al., 2004; Babbedge et al., 2004; Ilbert et al., 2006) or through follow-up spectroscopy at the position of the optical/near-infrared counterpart.

Attaining the scientific goals of future deep continuum surveys, which include determining both the star-formation and accretion histories of the universe, is thus largely dependent on the ability to identify the correct multi-wavelength counterparts to the faint radio sources. Identifying the counterparts to a large fraction of higher redshift radio sources will require very deep complementary multi-wavelength datasets. Given the resolution of these planned radio surveys, 10 arcsec for EMU, 15 arcsec for WODAN, and the increased difficulty of cross-matching to fainter magnitudes, it is possible that the required increase in depth of complementary datasets will complicate and frustrate the cross-identification process. It is thus of interest to determine how current sophisticated matching techniques such as the LR perform in the proposed case of low resolution ($\gtrsim$10 arcsec) radio observations matched to high resolution very deep infrared and optical catalogues. To investigate the question of cross-matching completeness and reliability in future surveys this chapter degrades the positional accuracy of the set of deep radio observations taken with 6 arcsec resolution and produces a number of simulated catalogues whose positional accuracies are consistent with observations taken at 10 arcsec and 15 arcsec resolution. I then use a LR analysis, similar to that in Smith et al. (2011) and Fleuren et al. (2012), to determine reliable NIR counterparts to both the original catalogue and the simulated 'low resolution' catalogues and compare the results.

The chapter is structured as follows: sections 3.1 and 3.2 outline the radio and infrared observations used in the matching procedures. Sections 3.3 and 3.4 give the details of the LR technique used for matching, section 3.5 explains the procedure used to simulate the low resolution catalogue and section 3.6 gives the results of the comparison. Section 3.7 summarises the effects of blended radio sources. Section 3.8 discusses the relevance of these results to future surveys and my conclusions are presented in section 3.9. All magnitudes are quoted in the AB magnitude system.

3.1 *Radio observations*

The radio survey used in this analysis consists of Very Large Array (VLA) observations at 1.4 GHz undertaken by Bondi et al. (2003). These VLA B-configuration observations cover a 1 square degree area, centred at α(J2000)=$2^{\rm h}26^{\rm m}00^{\rm s}$ and δ(J2000)=$-4^{\rm d}30'00''$, with nine pointings observed over a total of 56 hours (6 hours per pointing). To ensure uniform noise coverage across the whole field the pointings were separated by $1/\sqrt{2}$ times the 1.4 GHz primary beam of the VLA (∼31 arcmin). The final mosaiced image has a nearly uniform 1σ noise of ∼17 μJy and a FWHM synthesised beamwidth of 6 arcsec. Bondi et al. (2003) conclude that the good uv-coverage produced by their long observing tracks as well as their strategy of weighting the individual images by the square of the beam response in the mosaicing process result in negligable CLEAN bias and bandwidth smearing in their final image.

I used the original catalogue of radio sources in this field produced by Bondi et al. (2003) for the cross-matching procedure. Their catalogue was extracted from the mosaiced image using the AIPS (Greisen, 2003) Search and Destroy (SAD) task, retaining only sources with a peak flux to local noise ratio of $\gtrsim 5$. The final catalogue consists of 1054 radio sources whose peak flux densities exceed 60 μJy of which 19 are identified as multiple component radio sources. Radio sources are identified as multiple component sources if their individual components meet the following three criteria, the components are separated by < 18 arcsec, have peak flux ratios < 3, and all components have a peak flux > 0.4 mJy/beam. Further details of the calibration, catalogue extraction and multi-component classification procedures are outlined in Bondi et al. (2003)

For the purpose of evaluating the performance of the LR technique I disregarded the multiple component radio sources in the catalogue as the LR relies on knowledge of the ex-

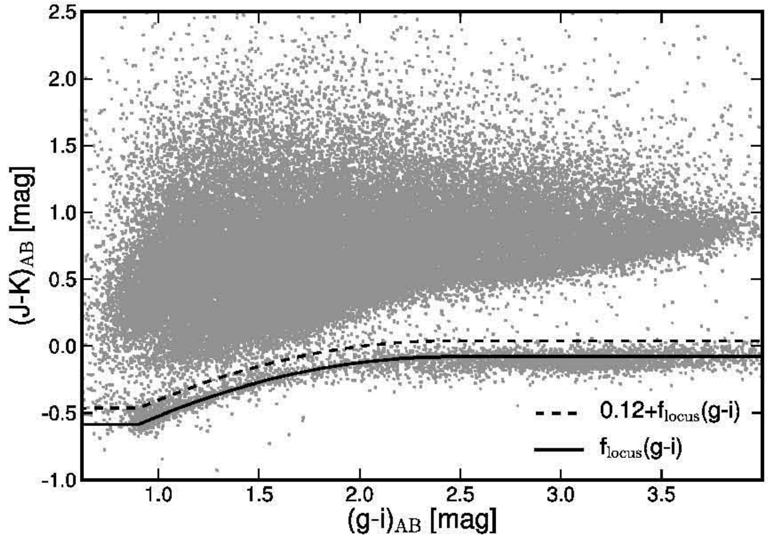

Figure 3.1: Fit to the stellar locus used to remove stars from the infrared cross-matching catalogue. The solid line indicates the fit to the stellar locus in the combined VIDEO/CFHTLS-D1 dataset. The dashed line indicates the separation criteria applied and objects below the dashed line were removed from the cross-matching catalogue.

pected position of the infrared counterpart and the associated errors on this position, and both these quantities are poorly determined in the case of multiple component radio sources. I also excluded single component radio sources whose morphologies are asymmetric or elongated as the position of the potential counterpart source is not well known in these cases. This morphological criteria results in the exclusion of a further 3 radio sources from the input catalogue. Such sources will be important components of future wide-area radio surveys, however they are not key to the LR evaluation presented in this chapter. All radio sources excluded from the matching procedure in this chapter are inspected for counterparts before determination of the radio luminosity function is presented in chapter 4.

3.2 *Multi-band photometry*

The whole square degree of VLA radio observations has been observed with the VISTA Deep Extragalactic Observations (VIDEO; Jarvis et al. in prep.) Survey. This is a 12 sq. degree survey over three fields currently being undertaken with the Visible and Infrared Survey Telescope for Astronomy (VISTA) designed to investigate the formation and evolution of galaxies and galaxy clusters. The survey provides photometry in the Z,Y,J,H and K_s bands to 5σ depths of 25.7, 24.6, 24.5, 24.0, 23.5 magnitudes (2 arcsec diameter apertures) respectively.

The 1 square degree with VLA observations also coincides with the Canada-France-Hawaii Telescope Legacy Survey (CFHTLS) D1 field which provides additional photometry in the $u*$,g',r',i',z' optical bands. The CFHTLS utilised the wide-field optical imaging camera MegaCAM on the 3.6 m Canada-France-Hawaii telescope. Completeness limits for the T0005 data release used in this work are 27.4, 27.9, 27.6, 27.4, 26.1 in $u*$,g',r',i',z' respectively. A final bandmerged catalogue for this field was produced by the VIDEO survey team using SEXTRACTOR (Bertin and Arnouts, 1996) in double image mode. This process used each image in the $u*$,g',r',i',z',Z,Y,J,H, $K_{\rm s}$ filters as a detection image in turn with photometric measurements in other bands made at the position in the detection images. Duplicate sources were removed by matching the detected catalogues to within 1 arcsec tolerance and retaining only the longest wavelength detection; full details of the extraction will be given in Jarvis et al. (in prep).

To minimise the number of spurious faint sources in the combined VIDEO-CFHTLS catalogue used for cross-matching I retained only those sources with $K_{\rm s} < 22.6$ (Petrosian magnitude), corresponding to an approximately 5σ detection in the VIDEO survey, and disregarded radio sources whose counterparts are affected by the presence of nearby saturated stars in the infrared images.

Infrared photometry to the full depth of the VIDEO survey will not be available over the 1000's of square degrees observed by ASKAP, LOFAR and MeerKAT for quite some time, an extremely deep large area infrared survey of this nature will only become feasible with the launch of the proposed ESA *Euclid* space mission (Laureijs, 2009; Laureijs et al., 2011). Given the stated importance of complementary datasets to the goals of these upcoming radio surveys it is of interest to determine the likely completeness achieved when cross-matching against more immediately available infrared surveys with similarly large sky coverage. One of the largest near-infrared surveys currently being undertaken is the VISTA Hemisphere Survey (VHS) which is surveying the entire Southern Hemisphere to a 5σ depth of $K_{\rm s}$=20.0. The VHS thus represents one of the deepest complementary datasets covering the entire survey area of the wide-field EMU survey and is an obvious ancillary dataset for EMU. With this in mind I also determine the completeness of such a cross-matched EMU-VHS dataset by performing a LR cross-match to the VIDEO catalogue limited to detections with $K_{\rm s} < 20.0$.

3.2.1 *Star-galaxy separation*

To remove contaminating stars from the combined NIR/optical catalogue, which are unlikely to be genuinely associated with radio sources, I employed a colour based criteria similar to that used by Baldry et al. (2010) in their star-galaxy separation algorithm for target selection in the GAMA survey. To achieve this separation I fitted the stellar locus in $(J\text{-}K)_{\mathrm{AB}}$ versus $(g\text{-}i)_{\mathrm{AB}}$ colour space with a quadratic $f_{\mathrm{locus}}(x)$ given by:

$$f_{\mathrm{locus}}(x) = \begin{matrix} -0.58 & & x < 0.4 \\ -0.88 + 0.82x - 0.21x^2 & \text{for} & 0.4 < x < 1.9 \\ -0.08 & & x > 1.9 \end{matrix} \tag{3.1}$$

where x is $(g\text{-}i)_{\mathrm{AB}}$ colour. Objects were removed from the cross-matching catalogue if their colours met the criteria:

$$J - K < 0.12 + f_{\mathrm{locus}}(g - i) \tag{3.2}$$

Figure 3.1 illustrates the fit to the stellar locus and the separation criteria used, quasars are located towards the top, left-hand corner of this plot.

Another method to achieve star-galaxy classification is to determine how well an object is resolved in the optical/NIR image, with stars and quasars being unresolved. Object detection and photometry for the VIDEO survey was achieved using SEXTRACTOR (Bertin and Arnouts, 1996). This package uses a neural network to assess how well resolved an object is and thereby determines a likelihood that an object is a star or galaxy. This likelihood is expressed as a CLASS_STAR estimate between 0 and 1.0 with stars having measurements close to 1.0 and galaxies close to zero. An inspection of these CLASS_STAR estimates reveal that the total contribution of stars to the VIDEO catalogue after implementing the colour threshold is <5%. I chose to use the criteria in equation 3.2 rather than a straightforward CLASS_STAR cut to avoid removing quasars, which are also unresolved in optical images and may be genuine counterparts to the radio sources. However it should be noted that the criteria in equation 3.2 also removes a small number of quasars from the final NIR catalogue. To demonstrate that

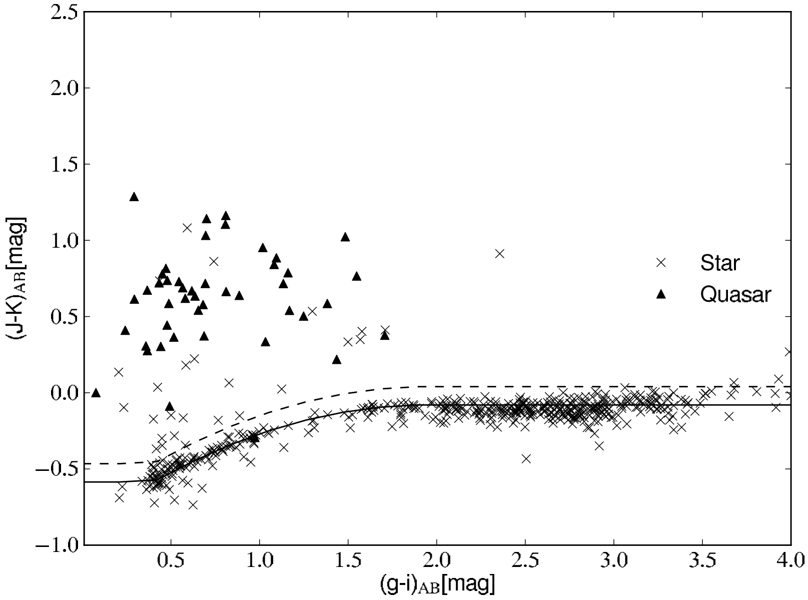

Figure 3.2: Colours of stars and quasars in the VVDS spectroscopic survey. The dashed line indicates the separation criteria applied in the combined VIDEO-CFHTLS dataset and objects below the dashed line were removed from the cross-matching catalogue.

this strategy is effective in figure 3.2 I include a colour-colour plot of all sources in the VIMOS VLT Deep Survey (VVDS; Le Fèvre et al., 2004, 2005) with confirmed stellar spectra as well as objects with broad emission line features classified as quasars and compare with the criteria in equation 3.2. Only 1 confirmed quasar and 31 stars are misclassified by the color criteria which corresponds to 2% and 6% of the total number of quasars and stars in the VVDS.

3.3 *Likelihood ratio*

The likelihood ratio is the ratio of the probability that a given source and counterpart are related to the probability that they are unrelated. It is given by the relationship:

$$\mathrm{LR} = \frac{q(m)f(r)}{n(m)} \tag{3.3}$$

(Sutherland and Saunders, 1992) where $f(r)$ is the probability distribution function of the offsets between the radio and infrared source positions, $q(m)$ is the probability distribution of the true infrared counterparts to the radio sources as a function of K_s-band magnitude and $n(m)$ is the magnitude probability distribution of the full catalogue of K_s-band detected objects. The procedure for calculating each of these quantities is described in the following

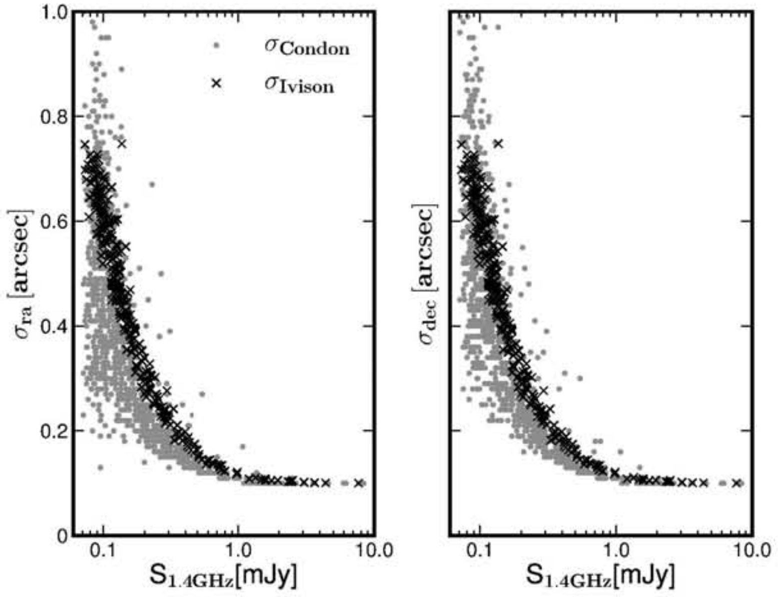

Figure 3.3: Comparison between the errors in the radio source positions calculated using the relationships in Condon (1997) $\sigma_{\rm Condon}$ and the error estimates used in the LR analysis $\sigma_{\rm Ivison}$ based on the relationships in Ivison et al. (2007).

sections.

3.3.1 *The radial dependence of the LR*

The radial probability distribution, which represents the decreasing probability that a pair of sources are related as their separation increases, $f(r)$ is given by the Gaussian:

$$f(r) = \frac{1}{2\pi\sigma_{\rm pos}^2} \exp - \left(\frac{r^2}{2\sigma_{\rm pos}^2} \right) \tag{3.4}$$

where r is the offset between the radio and infrared position and $\sigma_{\rm pos}$ is the combined positional error of the radio and infrared sources.

Positional errors of radio sources can be ascribed to two independent sources of error, calibration errors and noise-like errors (Condon et al., 1998). Calibration errors are independent of source strength and are best estimated by a comparison with external, more accurate data. In contrast, the noiselike contribution to positional errors is a function of the signal to noise ratio of the detection and is thus the dominant contributor to the positional errors of sources detected at low signal to noise. The noiselike positional errors of radio sources are usually estimated from the models of Condon (1997) for the propagation of errors in 2-dimensional Gaussian fits in the presence of Gaussian noise. The models give the noiselike contribution to the positional errors as:

$$\sigma_\alpha^2 \approx \sigma_{\rm M}^2 \sin^2({\rm PA}) + \sigma_{\rm m}^2 \cos^2({\rm PA}) \tag{3.5}$$

$$\sigma_\delta^2 \approx \sigma_{\rm M}^2 \cos^2({\rm PA}) + \sigma_{\rm m}^2 \sin^2({\rm PA}) \tag{3.6}$$

where $\sigma_\alpha, \sigma_\delta$ are the errors in the right ascension and declination of the fitted positions for the radio sources. PA is the position angle of the elliptical Gaussians and $\sigma_{\rm M}$,$\sigma_{\rm m}$ are the positional errors parallel to the major and minor axes of the fitted Gaussian respectively. They are given by the expression :

$$\frac{\sigma_{\rm M}^2}{\theta_{\rm M}^2} = \frac{\sigma_{\rm m}^2}{\theta_{\rm m}^2} = \frac{1}{4{\rm ln}2\rho^2} \tag{3.7}$$

$$\rho^2 = \frac{\theta_{\rm M}\theta_{\rm m}}{4\theta_{\rm N}^2}\left[1+\left(\frac{\theta_{\rm N}}{\theta_{\rm M}}\right)^2\right]^{\alpha_{\rm M}}\left[1+\left(\frac{\theta_{\rm N}}{\theta_{\rm m}}\right)^2\right]^{\alpha_{\rm m}}\frac{{\rm S}_{\rm P}^2}{\sigma_{\rm map}^2} \tag{3.8}$$

The $\theta_{\rm M}, \theta_{\rm m}$ terms are the size of the fitted major and minor axes, $\theta_{\rm N}$ is the FWHM of the restoring beam, $\sigma_{\rm map}$ is the average rms noise in the map and $S_{\rm P}$ is the peak of the fitted component.

However in recent work Ivison et al. (2007) derived a simplified expression for the positional errors due to the Gaussian fits in the special instance of all the radio sources being unresolved by the symmetric beam. In this instance the positional errors can be described by the following equation:

$$\sigma_{\rm fit} \simeq 0.6\frac{\theta_{\rm N}}{\rm SNR} \tag{3.9}$$

with SNR being the signal to noise ratio of the detected source. I adopted this simplified description of the expected positional errors in determing $\sigma_{\rm pos}$ for the LR.

The final positional errors should also include an estimate of the calibration error term. As there are no other radio catalogues over this area of better positional accuracy with which to make a comparison, Bondi et al. (2003) chose to estimate the calibration error term by comparing the position of the sources in the final mosaiced image with their positions in the images of the single VLA pointings. They find on the basis of this comparison that these calibration errors are of the order of 0.1 arcsec. Thus the final combined expected positional error is:

$$\sigma_{\rm pos}^2 = 0.1^2 + \sigma_{\rm fit}^2 \tag{3.10}$$

I justify this simplified description of the errors based on figure 3.3 which presents a comparison of the errors estimated using equation 3.9 with those predicted by the method of Condon (1997) and demonstrates that they are in reasonable agreement. However to account for the possibility that the radio and observed-frame K_s band emission may not arise at exactly the same position in the galaxy I imposed the additional restriction that the minimum positional accuracy does not drop below 0.5 arcsec thus $\sigma_\mathrm{pos} \geq 0.5$ arcsec.

Any systematic astrometric offsets between the radio observations and the NIR data need to be removed prior to the LR matching procedure. To determine these offsets I calculated the mean separation in right ascension and declination between the radio source positions and all possible NIR counterparts within a 3.6 arcsec radius, this radius corresponds to 5 times the maximum expected positional uncertainty for the radio sources. The mean offsets, with their standard errors ($\frac{\sigma}{\sqrt{N}}$), are $< \Delta\mathrm{ra} >$=0.15±0.03“ and $< \Delta\mathrm{dec} >$=0.45±0.03”, these offsets were subtracted from the radio positions to minimise systematic offsets between the radio and NIR co-ordinate systems. The offsets are only a fraction of the 1.5 arcsec pixel size of the radio image and are expected as the radio data has undergone self-calibration.

3.3.2 *The magnitude dependence of LR*

The magnitude dependence of the likelihood ratio depends on two quantities, the first of these $n(m)$ is simply the probability of observing a background, unrelated source of magnitude m, in the case of an unclustered population it can thus be directly calculated from the source counts of the input VIDEO catalogue normalised to the area of the survey. Galaxy clustering, on scales comparable to the search radius of the matching procedure, has the potential to bias the outcome of this procedure.

The second magnitude dependent term $q(m)$ is the most difficult component of the LR to determine accurately, it is the magnitude probability distribution of the true counterparts to the radio sources. This term is estimated using the method outlined in Ciliegi et al. (2003) which assumes that an observed excess of NIR sources, above the predicted background source counts, centred in the positions of the radio sources likely results from an association between these two groups of objects. The procedure thus begins by calculating the magnitude distribution of all the possible counterparts within a fixed search radius r_max of the radio positions. The distribution constructed in this manner is referred to as total(m). The contribution due to the background source counts is subtracted from total(m) to produce a magnitude distribution of the excess infrared sources detected around the radio positions, designated as real(m). Thus

$$\mathrm{real}(m) = \mathrm{total}(m) - \big(n(m) \times N_{\mathrm{radio}} \times \pi \times r_{\mathrm{max}}^2\big) \tag{3.11}$$

where N_{radio} is the total number of radio sources in the input catalogue and r_{max} is chosen search radius.

The $q(m)$ distribution is derived from real(m) by normalising real(m) and scaling it by a factor Q_0, where Q_0 is an estimate of the fraction of radio sources with infrared counterparts above the magnitude limit of the VIDEO survey. Hence:

$$q(m) = \frac{\mathrm{real}(m)}{\sum_m \mathrm{real}(m)} \times \mathrm{Q}_0 \tag{3.12}$$

The total(m), real(m), n(m) and q(m) distributions for the VIDEO-VLA cross-matched datasets are presented in figure 3.4. Limited statistics at the brightest magnitudes can lead to erroneous estimates of q(m) in the brightest bins and in the worst cases may lead to an estimate of zero probability of a match between bright NIR objects and the radio sources. To circumvent these effects I followed Smith et al. (2011) and simply extrapolated the q(m) values determined from the brightest well sampled bin.

3.3.2.1 *Calculating Q_0*

The Q_0 term is usually estimated by determining the fraction of radio sources with counterparts above the background as follows:

$$\mathrm{Q}_0 = \frac{N_{\mathrm{matches}} - (\sum_m n(m) \times \pi r_{\mathrm{max}}^2 \times N_{\mathrm{radio}})}{N_{\mathrm{radio}}} \tag{3.13}$$

(Ciliegi et al., 2003) where N_{matches} is the total number of possible counterparts within r_{max} of the radio positions and the second term in the numerator is just the total number of sources predicted by the background counts in an area corresponding to the size of the search radius multiplied by the number of radio sources. However for the datasets used in this thesis, when cross-matching with a large r_{max} I found this expression led to an overprediction of the Q_0

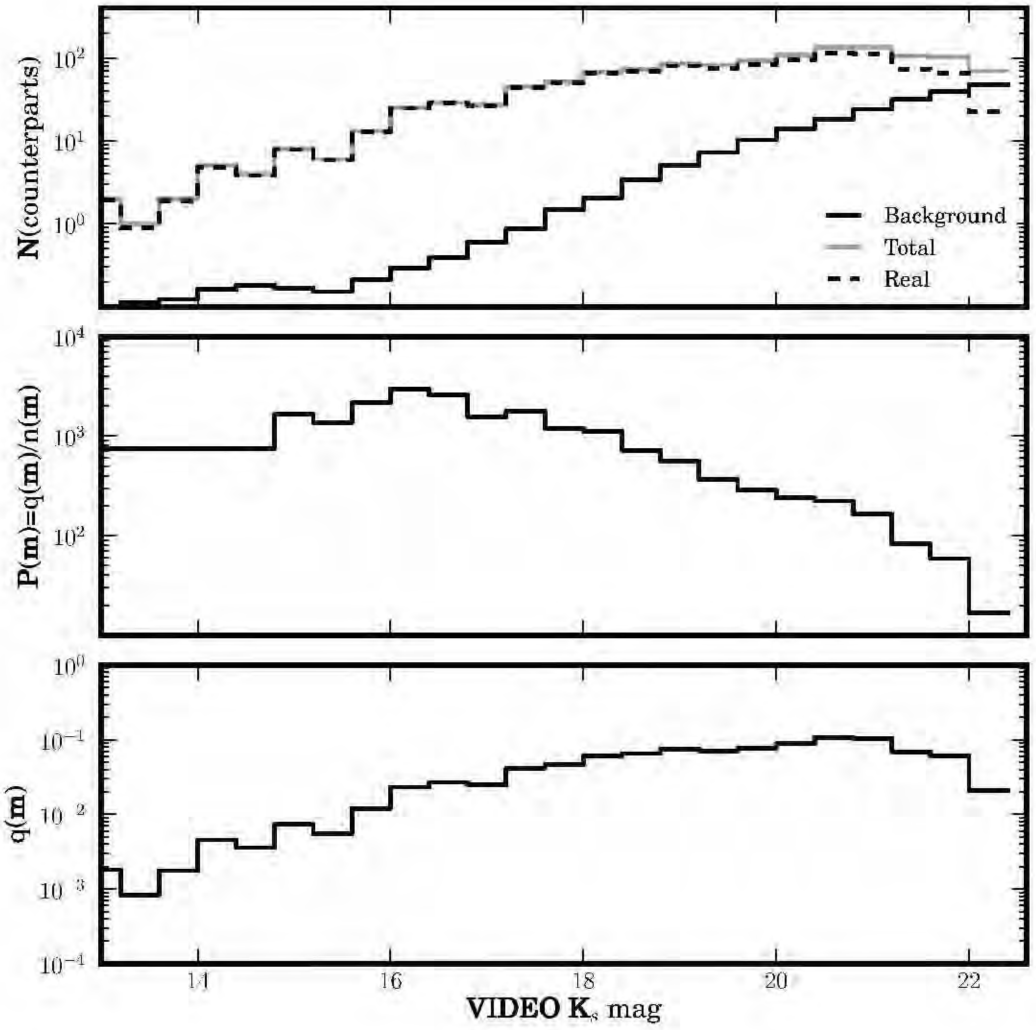

Figure 3.4: Top: The distribution of real(m) and total(m). Middle: The magnitude dependence of the of the LR $P(m)$. Bottom: $q(m)$ calculated by the LR in the cross-matching procedure.

value. The overprediction stems from the presence of an unexpectedly large number of excess sources in the search radii above the predicted background source counts. This effect may result from the tendency for radio-loud AGN to favour denser environments than normal galaxies (e.g. Best et al., 2005a; Falder et al., 2010), resulting in a large number of close neighbours for these sources. To overcome this difficulty I used the method recently developed by Fleuren et al. (2012) to estimate Q_0.

The Fleuren et al. (2012) method requires the creation of a number of simulated catalogues with the same total number of sources $N_{\rm radio}$ as the radio catalogue used for cross-matching but whose sources have random positions in the survey area. From these simulations one can calculate the number of random sources with no NIR counterparts within a search radius r of the random positions. This number of unpaired random sources as a function of radius is referred to as $U_{\rm random}(r)$ and is clearly related to the number of paired random sources $N_{\rm random}(r)$ as:

$$U_{\rm random}(r) = N_{\rm radio}(r) - N_{\rm random}(r) \tag{3.14}$$

Similarly one may calculate the number of sources in the real, observed radio catalogue which have no NIR counterparts within search radius r of the radio positions as a function of the size of the search radius $U_{\rm obs}(r)$. The number of truly unpaired radio sources, ie. those with no true counterpart in the VIDEO catalogue, can be related to the number of observed unpaired sources by the following relation:

$$U_{\rm true}(r) = U_{\rm obs}(r) + \epsilon_r U_{\rm true}(r), \tag{3.15}$$

where $U_{\rm true}$ is the number of truly unpaired radio sources and ϵ_r is the fraction of truly unpaired radio sources which are observed as paired due to a random background source occuring with a distance r of the radio position. The ϵ_r term can be determined from the simulated random catalogues as:

$$\epsilon_r = \frac{N_{\rm random}(r)}{N_{\rm radio}} \tag{3.16}$$

as all paired sources in the random catalogues occur as a result of this type of random alignment effect. Equation 3.15 can then be re-arranged to make U_{true} the subject:

$$U_{\text{true}}(r) = \frac{U_{\text{obs}}(r)}{1 - \epsilon_r} \tag{3.17}$$

It is then possible to estimate $1 - Q(r)$, which is the fraction of sources which have no true counterpart within the search radius r, as follows:

$$1 - Q(r) = \frac{U_{\text{true}}(r)}{N_{\text{radio}}} \tag{3.18}$$

substituting equations 3.17, 3.16 and 3.14 results in:

$$\begin{aligned} 1 - Q(r) &= \frac{U_{\text{obs}}}{(1 - \epsilon_r)N_{\text{radio}}} \\ &= \frac{U_{\text{obs}(r)}}{U_{\text{random}}(r)} \end{aligned} \tag{3.19}$$

To account for the fraction of counterparts which lie outside r_{max} and relate the above equations to Q_0, which is the quantity of interest, it can been seen that :

$$\begin{aligned} \frac{U_{\text{obs}(r)}}{U_{\text{random}}(r)} &= (1 - Q_0) + (1 - F(r)) - (1 - Q_0)(1 - F(r)) \\ &= 1 - Q_0 F(r) \end{aligned} \tag{3.20}$$

where $(1 - Q_0)$ represents the fraction of sources with no counterpart in the NIR catalogue, $(1 - F(r))$ is the fraction of sources whose counterparts fall outside the search radius r and $(1 - Q_0)(1 - F(r))$ is the fraction of sources with no counterpart in the catalogue but whose counterpart would fall outside the search radius if detected. It should be added that:

$$\begin{aligned} F(r) &= \int_0^r P(r')dr' = 1 - e^{\frac{r^2}{2\sigma^2}} \\ P(r) &= 2\pi r f(r) \end{aligned} \tag{3.21}$$

Thus Q_0 is determined by finding the best-fitting value of the observed ratio of $\text{U}_{\text{obs}}(r)$ to $\text{U}_{\text{random}}(r)$ from equation 3.20. The fits used to obtain Q_0 terms are included in figure 3.5 and a comparison of the Q_0 estimates produced by the two methods is presented in table 3.1,

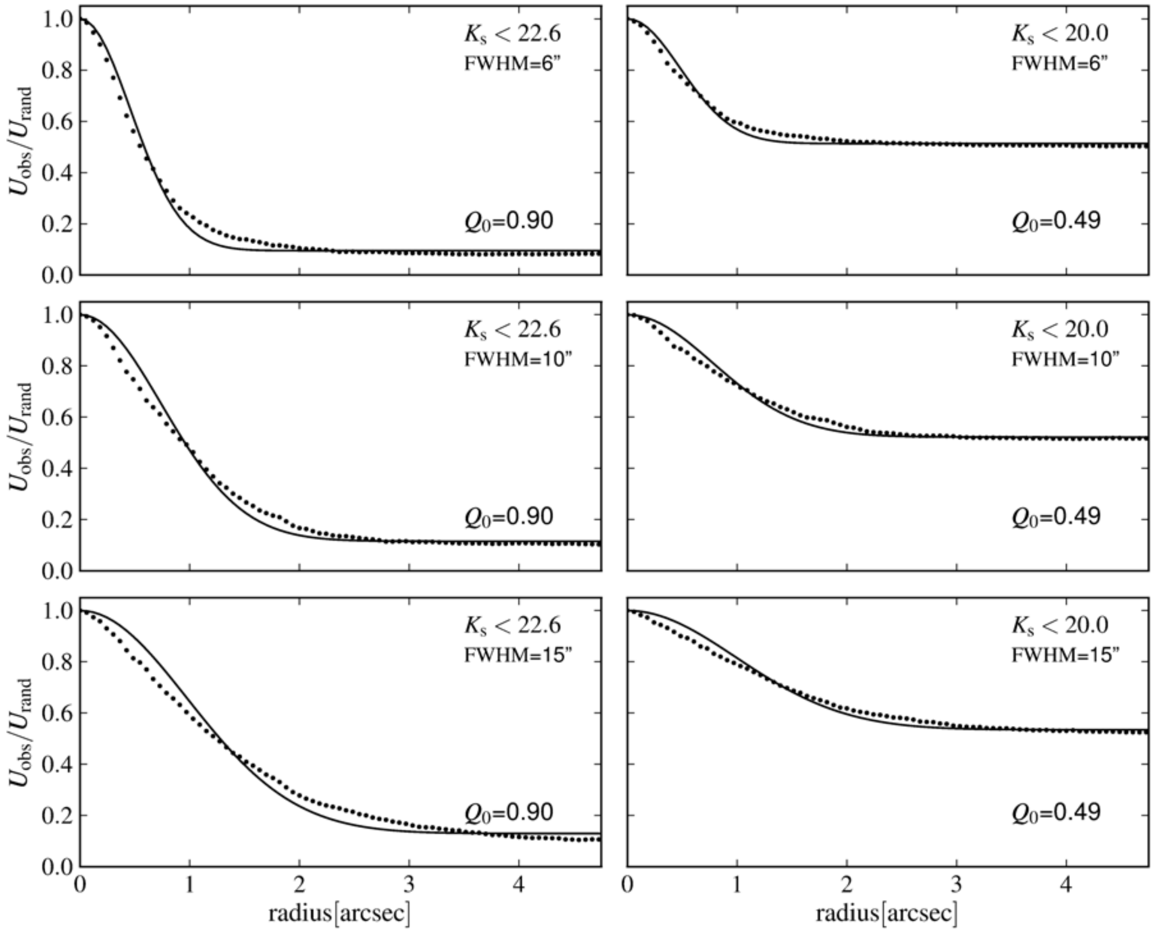

Figure 3.5: Fit to the ratio of unpaired sources in the radio catalogues $U_{\rm obs}(r)$ and unpaired sources in a catalogue of random positions $U_{\rm rand}(r)$ used to estimate Q_0 according to equation 3.20.

which clearly demonstrate the Q_0 overprediction produced by the Ciliegi et al. (2003) method when applied to this dataset. As such the estimates produced by the Fleuren et al. (2012) method are adopted in the LR matching procedures at all resolutions.

3.4 *Reliability of counterparts*

The presence or absence of more than one infrared counterpart for a particular radio source provides extra information to that contained in the LR itself which can then be used to estimate the reliability of the counterpart source, or the probability that a particular source is the correct

Table 3.1: Comparison of Q_0 estimates using the methods of Ciliegi et al. (2003) and Fleuren et al. (2012).

		6 arcsec	10 arcsec	15 arsec
$K_\mathrm{s} < 22.6$	Q_0 (eqn 3.13)	1.03	1.19	1.3
	Q_0 (eqn 3.20)	0.90	0.90	0.90
$K_\mathrm{s} < 20.0$	Q_0 (eqn 3.13)	0.51	0.55	0.57
	Q_0 (eqn 3.20)	0.49	0.49	0.49

counterpart. The reliability is calculated as:

$$\mathrm{Rel_i} = \frac{\mathrm{LR_i}}{\Sigma_\mathrm{j}\mathrm{LR_j} + (1 - \mathrm{Q_0})}, \tag{3.22}$$

where j is the index of all the possible counterparts to the radio source. We accept sources with $\mathrm{Rel}_i > 0.8$ as being reliably identified counterparts to the radio source.

Including the Q_0 term in equations 3.12 and 3.22 allows the LR method to account for the fact that not all the VLA radio sources will have a counterpart detected in the VIDEO survey. This is an advantage that the LR method has over simple nearest neighbour matches and frequentist methods like the Downes et al. (1986) statistic which intrinsically assume that all the radio sources have a match in the complementary dataset. This a particularly useful feature of the method when cross-matching observations which are primarily sensitive to different astronomical populations resulting in a large fraction of the sources you are trying to match being undetected in the ancillary dataset. An excellent example of such a scenario is the effort to cross-match far-infrared sources in the Herschel-ATLAS science demonstration phase field with r-band optical sources in the SDSS by Smith et al. (2011). Their LR method demonstrated that only 60% of the far-infrared sources in Herschel-ATLAS are detected in the SDSS-DR7 (Abazajian et al., 2009) r-band catalogue to a depth of 22.4 magnitudes, but the high surface density of SDSS sources at this magnitude limit and low resolution Herschel beams resulted in 70% of the far-infrared sources having a least one match within a $5\sigma_\mathrm{pos}$ radius of the Herschel position. Although a large fraction of the radio sources used in this thesis are detected in the VIDEO dataset the LR will provide an invaluable means to evaluate such effects when matching future much deeper radio surveys against potentially shallower IR and optical datasets, as would be the case in a cross-match between the future VHS and EMU-wide surveys. The LR and reliabilities for the VLA-VIDEO datasets are presented in figure 3.6.

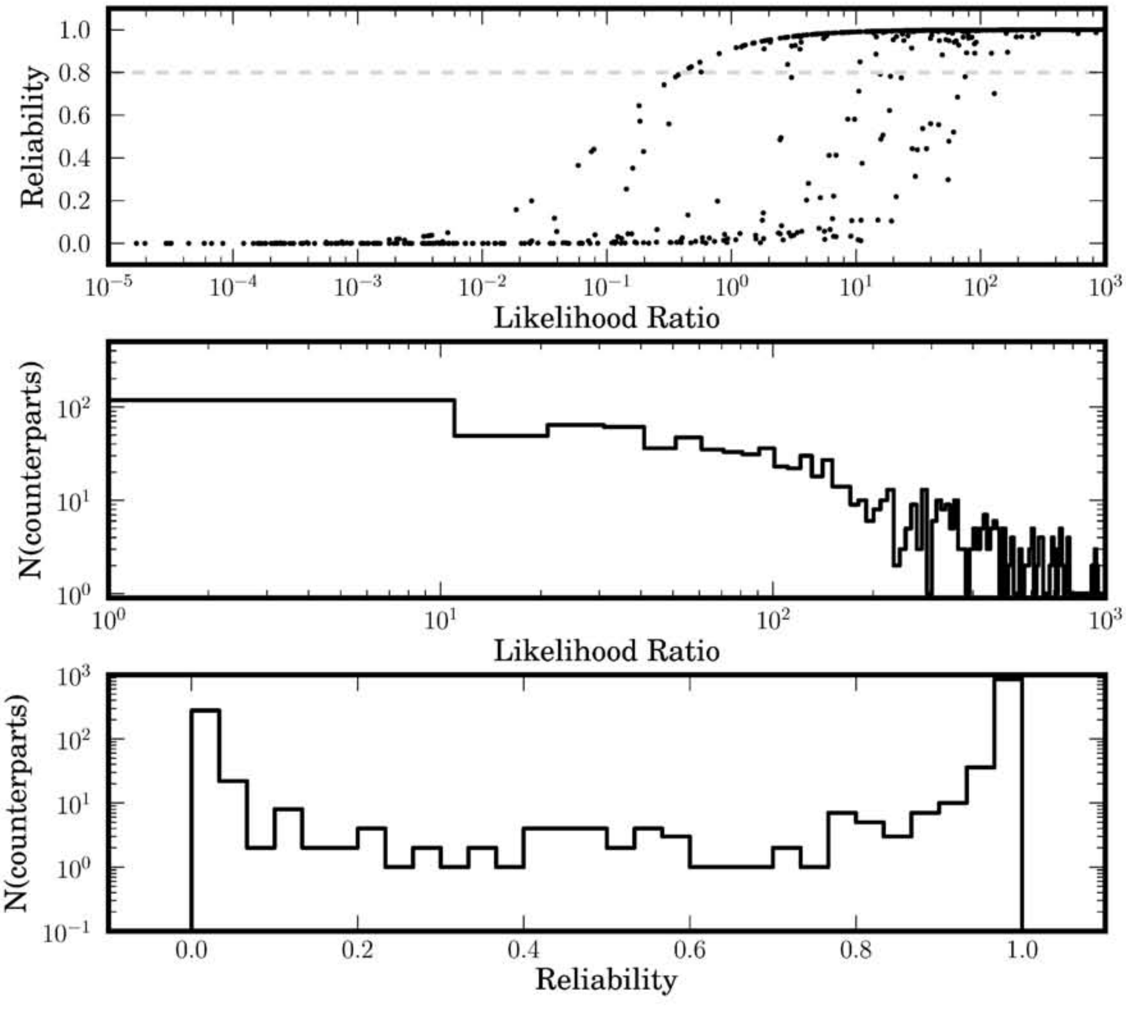

Figure 3.6: Likelihood ratios and reliabilities for the VLA-VIDEO cross-matched dataset. Reliability is not linearly related to likelihood ratio and only sources with reliabilities >0.8 are retained as reliable counterparts.

Implementing a reliability threshold, rather than adopting sources with the highest LR as the most likely counterparts, has the crucial advantage of minimising the number of spurious false identifications in the final cross-matched catalogue. The LR method allows one to estimate the number of contaminating false identifications $N_{\rm cont}$ in a catalogue of cross-matches with Rel >0.8 as being :

$$N_{\rm cont} = \sum_{\rm Rel>0.8} (1 - {\rm Rel}). \tag{3.23}$$

This contamination estimator can be used to adjust the reliability threshold to maximise completeness at the expense of a higher fraction of false matches (by decreasing $\mathrm{Rel}_{\rm thresh}$) or minimise contamination with a lower degree of completeness (by increasing $\mathrm{Rel}_{\rm thresh}$) in accordance with demands of the scientific goals of any particular cross-matching procedure.

3.5 *Simulated catalogue*

This chapter aims to determine whether the LR cross-matching procedure will reliably identify a large fraction of the counterparts to the radio sources detected in future radio continuum surveys including EMU, MIGHTEE and WODAN. Thus I compare the performance of this technique at 6 arcsec resolution against observations with 10 and 15 arcsec resolution, which are the proposed resolutions of the EMU and WODAN surveys respectively. To simulate the degradation of positional accuracy in the Bondi et al. (2003) catalogue which would take place if these observations were performed to the same depth with a larger synthesised beam, Gaussian scatter is added to the positions of the radio sources in the catalogue in line with the theoretical predictions of the equations 3.9 and 3.10 in section 3.3. 100 simulated 'low resolution' catalogues with simulated FWHM beamwidths of 10 and 15 arcsec are generated in this manner. The limitation of this approach is that it precludes the study of instances where close pairs of radio sources merge within the larger synthesised beam and the impact this blending may have on the LR's ability to make reliable counterpart identifications. An attempt is made to estimate the effect of these blended radio sources separately from the LR analysis in section 3.7.

3.6 *Near-infrared counterparts to radio sources*

I used the LR technique to find counterparts for both the original VLA radio catalogue and the two sets of 100 simulated catalogues with nominal FWHM beamwidths of 10 and 15 arcsec. The radio sources are first matched to almost the full depth of the VIDEO catalogue with $K_{\rm s} < 22.6$ and this procedure is then repeated with the VIDEO catalogue restricted to detections with $K_{\rm s} < 20.0$. In order to ensure that the search radius includes all possible real counterparts to the radio sources $\rm r_{max}$ is set to 5 times the largest expected positional error $\sigma_{\rm pos}$ at each of the three resolutions considered in this study. This results in an $\rm r_{max}$ of 3.6, 6.0 and 9.0 arcsec in the LR analysis of the 6,10 and 15 arcsec catalogues respectively. The $f(r)$ term of the LR is also adjusted to account for the increased positional uncertainty in the lower resolution catalogues. A summary of the relevant parameters used in the LR analysis at the three different resolutions is given in tables 3.2 and 3.3 for the $K_{\rm s} < 22.6$ and $K_{\rm s} < 20.0$ cases respectively. For the simulated catalogues these tables contain the mean and standard deviation of the 100 LR matching procedures performed at each resolution.

Table 3.2: Summary of relevant parameters in the LR analysis for the 6, 10 and 15 arcsec catalogues when matching against the VIDEO catalogue with $K_{\rm s} < 22.6$. N(Rel>0.8) and % Rel>0.8 represents the number and percentage of radio sources which have counterparts with Rel>0.8. The total number of radio sources in the input catalogue is 1031. Similarly $\rm N_{cont}$ and % cont represent estimates of the number and percentage contribution of misidentified contaminating sources.

	6 arcsec	10 arcsec	15 arcsec
$r_{\rm max}$ [arcsec]	3.6	6.0	9.0
Q_0	0.90	0.90	0.90
N(Rel>0.8)	915	887. ± 6	838 ± 7
$N_{\rm no\ match}$	68	51 ± 2	33 ± 2
$N < \rm r_{max}$	1274	1809 ±9	2669 ± 13
$N_{\rm cont}$	6.82	12.40 ±0.81	19.34 ± 0.93
% Rel>0.8	88.7%	86.0 ± 0.6%	81.8 ± 0.7%
% cont	0.74%	1.4 ± 0.1%	2.3 ± 0.1%

3.6.1 *Counterparts as a function of resolution*

An inspection of table 3.2 reveals that when cross-matching against the full VIDEO catalogue the number of sources with reliable counterparts decreases with decreasing resolution. The LR

Table 3.3: Summary of relevant parameters in the LR analysis for the 6, 10 and 15 arcsec catalogues with $K_\mathrm{s} < 20.0$. The row headings are as in table 3.2.

	6 arcsec	10 arcsec	15 arcsec
r_max [arcsec]	3.6	6.0	9.0
Q_0	0.49	0.49	0.49
N(Rel>0.8)	486	490 ± 4	485 ± 5.
$N_\mathrm{no\ match}$	510	484 ± 2	437 ± 3.
$N <$ r$_\mathrm{max}$	567	646 ±3	776 ± 5
N_cont	3.93	6.84 ±0.55	11.06 ± 0.71
% Rel>0.8	47.1%	47.5 ± 0.6%	47.0 ± 0.5%
% cont	0.80%	1.4 ± 0.1%	2.3 ± 0.1%

identifies 915, 887 and 838, sources with reliable counterparts at 6,10 and 15 arcsec resolution, with each decrease in resolution resulting in a loss of approximately 3% and then a further 4% of the identifications. The completeness as a function of flux density for all three resolutions is shown in figures 3.7 and 3.8. These figures indicate that the number of lost identifications increase at lower flux densities where the lower signal to noise ratio of the detections result in larger positional uncertainties. For clarity figure 3.8 presents a close-in view of the completeness at the fainter flux densities (< 1mJy) and the greyscale filled regions in this figure indicate the 1σ variation between the 100 simulated catalogues at each resolution.

Encouragingly, the results indicate that at 6 arcsec resolution the LR is able to identify nearly all the available counterparts whose magnitudes are less than the imposed $K_\mathrm{s} < 22.6$ magnitude limit as the fraction of reliably identified sources 89% is very close to the estimated Q_0 value of 0.90. The results also indicate that the contribution of contaminating or misidentified sources is very low at $\sim 0.7\%$. Table 3.2 also reveals that the number of contaminating sources in the cross-matched catalogue increases at lower resolution to 1.4% and 2.3% at resolutions of 10 and 15 arcsecs. In section 3.4 I discussed the possibility of adjusting the reliability threshold to maximise completeness or minimise contamination, it is clear that such an adjustment would not be advantageous in the VLA dataset used here as the close match between completeness and Q_0 indicates that there are very few remaining unidentified true counterparts in the VIDEO dataset and lowering $\mathrm{Rel}_\mathrm{thresh}$ would only introduce a large number of false identifications for very minimal gains in completeness. The power of the LR as a tool for removing possibly spurious identifications is also clear from table 3.2, as even though the total number of radio sources with possible counterparts increases at lower resolution the larger uncertainties

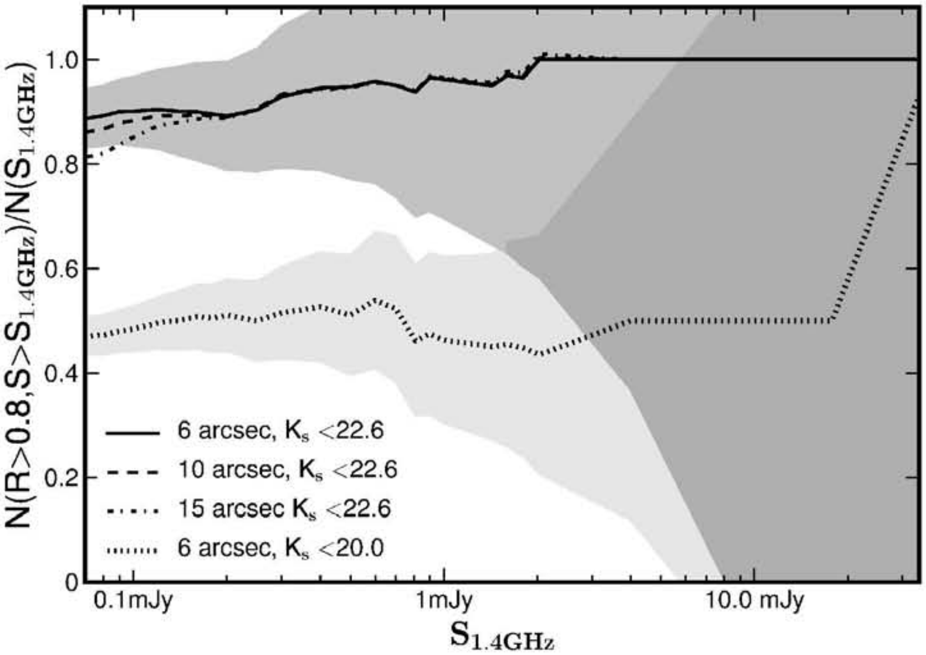

Figure 3.7: The fraction of reliable counterparts detected at 6, 10 and 15 arcsec resolution when matching against the VIDEO NIR catalogue restricted to detections with $K_{\rm s} < 22.6$ and $K_{\rm s} < 20.0$. The greyscale bands represent the 1σ Poisson error on the cross-matched fractions.

in $\sigma_{\rm pos}$ result in the expected decrease in the number of secure identifications.

A subsection of the radio data in this chapter has previously been matched to deep $K-$band data using a LR procedure (Ciliegi et al., 2005). This matching was performed over a 165 arcmin^2 field observed by Iovino et al. (2005), the limiting magnitude used in the matching procedure corresponds to the 50% completeness limit of $K_{\rm s}$=23.9. Ciliegi et al. (2005) find a total of 43 reliable K-band matches to the 65 radio sources located within this subfield, corresponding to a completeness of $\sim$ 66% which is significantly lower than the 88.7% completeness achieved in this work. This improvement can be ascribed to the greater depth of the VIDEO survey, which has factor of $\sim$12 greater integration time over the Iovino catalogue with a telescope of similar aperture. Furthermore the $q(m)$ distributions and LR in Ciliegi et al. (2005) are derived from the VVDS optical catalogues from McCracken et al. (2003) available over the whole 1 square degree radio field. As $q(m_{opt})$ distributions are not precisely equivalent to $q(m_{NIR})$ it is likely that their use of the optical magnitude distribution in the matching procedure contributes to an underestimate of the significance of some of the fainter NIR matches.

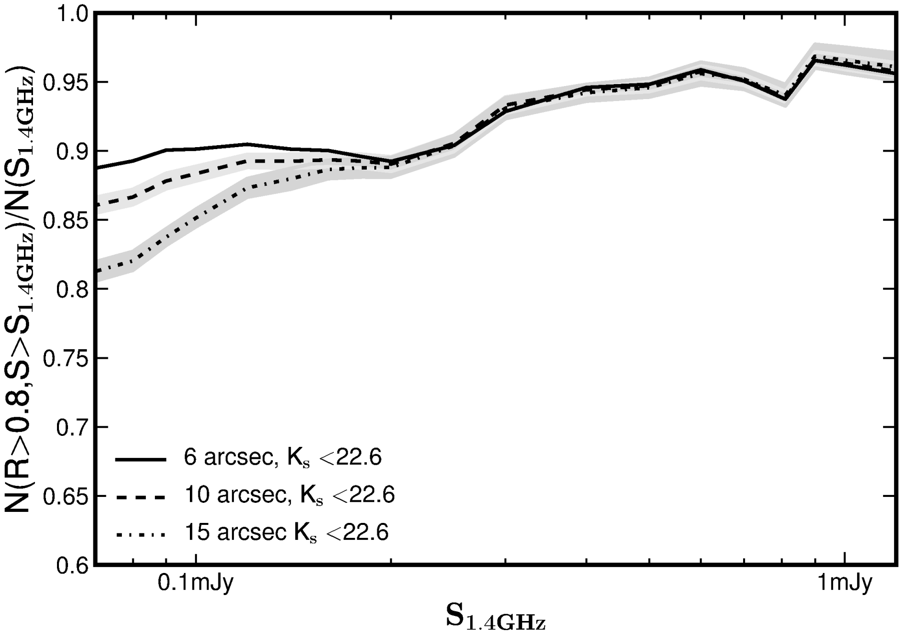

Figure 3.8: Close-in plot of the fraction of reliable counterparts detected for the faint radio sources (< 1 mJy) at 6,10 and 15 arcsec resolution when matching against the VIDEO NIR catalogue restricted to detections with $K_\mathrm{s} < 22.6$. The greyscale filled bands represent the 1σ variation between the 100 simulated low resolution radio catalogues and do not include the Poisson errors.

3.6.2 *Counterparts as a function of near-infrared magnitude*

In the case of matching against the VIDEO catalogue limited to the depth of the VHS, table 3.3 reveals a similar increasing trend in the number of contaminating sources with decreasing resolution from 0.8% at 6 arcsec to 1.4 and 2.3% at the lower resolutions. However the completeness of the cross-matched catalogue is nearly identical at all three resolutions, indicating that the depth of the complementary near-infrared data is a more relevant limiting factor at these shallower survey depths than radio survey resolution. This trend can be understood by examining the middle plot in figure 3.4, which indicates that NIR counterparts with magnitudes lower than $K_\mathrm{s} < 20.0$ are assigned higher $q(m)/n(m)$ fractions than fainter NIR matches. The intrinsic rarity of brighter NIR sources thus increases the significance of these bright NIR matches allowing us to partially overcome the limitation of poorer positional accuracy. In contrast at deeper NIR magnitudes the increasing density of faint sources dictates that resolution, or equivalently positional accuracy, is increasingly relevant in determining the correct counterpart.

Figure 3.9 shows a plot of the fraction of reliably identified counterparts as a function of K_s band magnitude. This demonstrates that deep near-infrared and/or optical data are

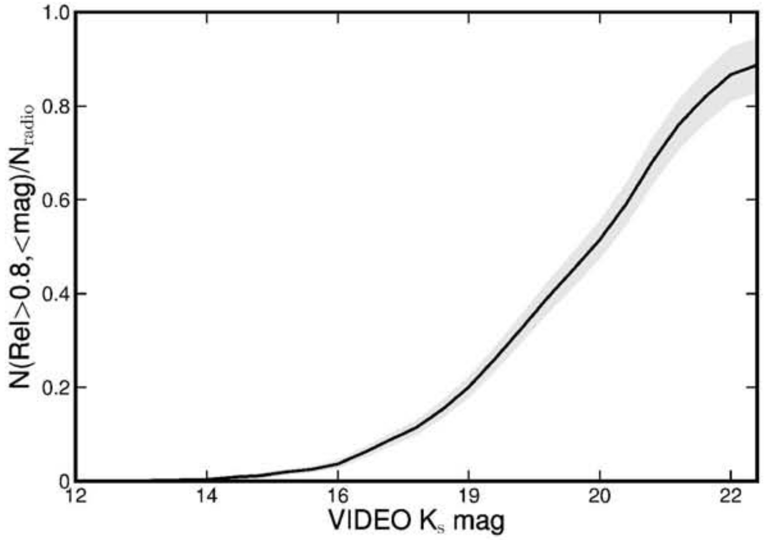

Figure 3.9: The fraction of reliably associated counterparts as a function of K_s magnitude at 6 arcsec resolution for the depth of the radio imaging data. The greyscale bands represent the 1σ Poisson error on the cross-matched fraction.

crucial for successfully identifying faint radio sources, at least to the depth of the VLA radio imaging data used in this study. This will only become more of an issue for yet deeper radio imaging such as those planned with the MeerKAT (e.g. Jarvis 2011). I note that once again the reliably identified fraction of radio sources is very close to the Q_0 estimate indicating that the LR is identifying nearly all the available counterparts in the NIR catalogue to $K_s < 20.0$.

Early works using the LR method to identify optical counterparts to radio sources in the WENSS to flux-density limits of ∼1 mJy were thus hampered by the relatively shallow optical data available at the time. Consequently Windhorst et al. (1984) identify only 45% of the radio sources in optical plates taken with the Kitt Peak Mayall telescope, while de Ruiter et al. (1977) are only able to identify 15% of the 1 mJy radio source counterparts in observations taken with the Palomar 48“ Schmidt telescope. These authors also noted the trend for fainter radio sources to be identified with fainter optical counterparts and the importance of obtaining deeper observations to identify counterparts to faint radio sources.

3.6.3 *Mis-identified counterparts at low resolution*

Apart from considering changes to the overall completeness with resolution it is also of interest to determine whether there are differences between the low and high resolution catalogues in terms of the subset of radio sources that have reliably identified counterparts and whether these radio sources are associated with the same NIR counterpart in all cases. Changes in the exact composition of the output cross-matched catalogues occur because the Gaussian scatter introduced to the positions of the simulated low resolution radio sources will alter their relative position to any possible near-infrared counterparts, furthermore the lower resolution catalogues have larger positional uncertainties $\sigma_{\rm pos}$. These two factors result in changes to the $f(r)$ term of the LR and consequently alter the overall statistical significance of a match between any pair of sources. Changes in the cross-matched low resolution catalogues compared to the original VLA cross-matched catalogue occur in three different forms, radio sources with secure identifications at 6 arcsec no longer have secure identifications in the low resolution catalogue, these are referred to as $\rm R_{lose}$, radio sources with no reliable counterparts at 6 arcsec have an identified counterpart at lower resolution $\rm R_{gain}$. Radio sources with secure identifications at both resolutions $\rm R_{common}$ are identified with a different NIR counterpart at different resolutions $\rm R_{diff\ id}$. The average changes in the composition of the output catalogues are listed in tables 3.4 and 3.5, these are relative to the original VLA cross-matched catalogue in all cases. These tables indicate that differences in the exact composition of the output cross-matched catalogues at the three different resolutions are usually small. When matching against the deeper VIDEO catalogue 95 and 88% of the radio sources in the original cross-matched catalogue are identified with the identical NIR counterpart in the 10 and 15 arcsec catalogues. The catalogue with shallower NIR magnitude limits produced even fewer discrepancies with 98 and 95% of the identifications remaining unchanged at lower resolution. This clearly illustrates the increased difficulty in associating the radio sources with their correct counterparts when matching against very deep complementary datasets.

Table 3.4: Summary of differences between the cross-matched catalogues created when matching against the original 6 arcsec resolution catalogue and the simulated low resolution catalogues at 10 and 15 arcsec. This table summarises the differences when matching against the VIDEO NIR catalogue limited to $K_{\rm s} < 22.6$.

	10 arcsec	15 arcsec
$R_{\rm lose}$	42 ± 5	94 ± 6
$R_{\rm gain}$	14 ± 3	17 ± 3
$R_{\rm common}$	873 ± 5	821 ± 6
$R_{\rm diff\ id}$	5 ± 3	10 ± 3

Table 3.5: Summary of differences between the cross-matched catalogues created when matching against the original 6 arcsec resolution catalogue and the simulated low resolution catalogues at 10 and 15 arcsec resolution. This table summarises the differences when matching against the VIDEO NIR catalogue limited to $K_\mathrm{s} < 20.0$.

	10 arcsec	15 arcsec
R_lose	10 ± 3	24 ± 4
R_gain	14 ± 2	23 ± 3
R_common	476 ±3	462 ± 4
$R_\mathrm{diff\ id}$	1 ±1	2 ±1

3.6.4 *Redshift distributions of identified radio sources*

Photometric redshifts for the combined VIDEO and CFHTLS-D1 datasets have been derived using SED fitting techniques with the photometric redshift package Le Phare (Arnouts et al., 1999; Ilbert et al., 2006), based on simulations these redshifts have accuracies of σ_z ~0.1 for sources with $K_\mathbf{s} < 22.6$, and for a small sample of real objects with spectroscopic redshifts from the VVDS survey (Le Fèvre et al., 2007) σ_z ~0.095. Further details of the procedure used to estimate these photometric redshifts and their errors are presented in section 4.4 of chapter 4. Figure 3.10 presents the redshift distribution of sources matched at 6 arcsec to almost the full depth of the VIDEO survey with those restricted to matches with $K_\mathbf{s} < 20.0$. Unsurprisingly there is clear evidence for a decline in the fraction of high redshift sources detected in the survey with shallower magnitude limits. It is clear that while the VHS survey will allow us to identify a significant fraction ~ 83%, of the sources with z< 1.2 a large fraction of the radio sources at redshifts higher than this threshold will not be present in this shallower wide-field survey. The histogram indicates that only 14% of the identified counterparts at z > 1.2 had magnitudes brighter than the $K_\mathbf{s} < 20.0$ limit. There is also evidence for a loss of a significant (~40%) number of counterparts in the $1 \lesssim z \lesssim 1.2$ redshift bin.

3.7 *Blended sources*

As mentioned in section 3.5, this LR investigation makes no attempt to consider the possible effects of an increased number of blended sources at lower resolutions on the completeness produced by the LR technique. To estimate the increase in the number of radio sources which will be blended by the beam in 10 and 15 arcsec images, compared to the 6 arcsec resolution

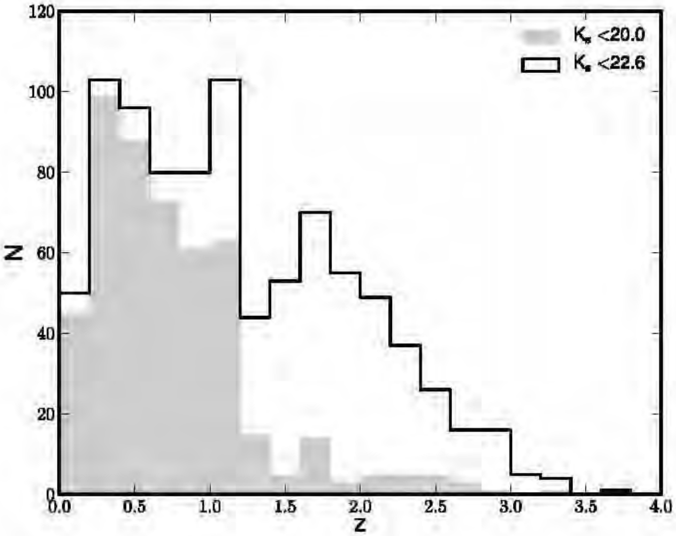

Figure 3.10: The photometric redshift distribution of the counterparts in the matched catalogues restricted to sources with magnitudes $K_\mathrm{s} < 22.6$ and $K_\mathrm{s} < 20.0$.

image, I used the size and spatial distribution of radio sources predicted in the Square Kilometer Array Simulated Skies (Wilman et al. 2008; 2010). From this simulation I extracted a list of radio source components with $S_{1.4\mathrm{GHz}}$ greater than the predicted 5σ flux density limit of the EMU survey of 50 μJy over a 1 square degree field of view. The size of the radio components were adjusted to simulate the effect of convolution with a Gaussian beam of FWHM size of 6, 10 and 15 arcsec respectively.

Separating close components in an astronomical image is a complex problem and source extraction packages adopt a variety of approaches to this task. For instance the AIPS SAD task attempts to separate emission features into multiple components based on the level of residual flux present after a single component Gaussian fit, whereas SEXTRACTOR maps the detected emission at a number of sub-thresholds to detect junctions in the emission profile of the blended source (Bertin and Arnouts, 1996). Consequently the probability of separating a pair of close sources is difficult to quantify and depends on the characteristics of the pair including their separation, relative angular sizes, orientations and peak fluxes as well as the details of the deblending technique in question. To obtain an estimate of the fraction of blended pairs in the catalogues I make the simplifying assumption that a source extraction algorithm will be unable to separate a pair of sources if their separation is less than the mean of their FWHM. In this determination I disregarded the contribution of very extended sources (> 17 arcsec) as

Table 3.6: The number of blended sources detected at 6, 10 and 15 arcsec resolution predicted by the SKA Simulated Skies (Wilman et al. 2008; 2010). Column 1 indicates the number of components blended per detected source.

Number of components	6 arcsec	10 arcsec	15 arcsec
	unrelated blends		
2	22	36	62
	multiple component blends		
2	218	218	219
3	41	41	41
4 or more	2	4	4

these should be fully resolved by the beam, these extended sources constitute less than 5% of the total source population at the chosen flux density limits.

To confirm that this simplification is reasonable I created maps of the simulated radio source components at 6, 10 and 15 arcsec resolution using the Simulated Skies S3Map tool (Levrier et al., 2009). The AIPS SAD task was used to extract a source list from these images and an inspection of the output component lists confirmed that the pairs selected using the separation criteria were detected as a single Gaussian component by the SAD algorithm. Based on the separation criteria and an inspection of the SAD outputs I determined the number of detected radio sources in the simulated field which consist of a blend of two or more underlying radio source components. I separate these blended sources into two classes, detected radio sources which consist of a blend of multiple radio components arising from the same radio galaxy (i.e. radio lobes from an FRI/FRII source blended together) and sources which are a blend of unrelated radio galaxies, the results of this analysis are presented in table 3.6.

The initial simulated component list consisted of 1908 components with $S_{1.4\mathrm{GHz}} > 50\,\mu$Jy, these are reduced to 1579, 1557 and 1531 detected sources of which 283, 299 and 325 detections are blended sources in the 6, 10 and 15 arcsec catalogues respectively. As the LR is not designed to account for the possibility of two or more counterparts per radio source it is reasonable to assume that sources which consist of a blend of unrelated radio galaxies will not be reliably associated with an appropriate counterpart. The total contribution of these unrelated blends increases from 1.4% at 6 arcsec resolution to 2.3 and 4.0% at 10 and 15 arcsec resolutions respectively. Thus I conclude that the contribution of this effect to incompleteness in any LR based cross-matching routine in future surveys will be small, at the level of approximately 1$\sim$2.5%. The real contribution of this effect will depend on the baseline distribution and uv coverage of the survey in question. I did not attempt to estimate to what extent the blended multiple component radio sources will contribute towards incompleteness when cross-matching as the symmetric nature of the SKADS simulation radio sources will not allow a realistic determination of the expected deviation in the position of the final blended radio sources from the expected position of the NIR counterpart.

3.8 *Towards deeper surveys with MeerKAT*

Although this chapter has concentrated on the LR's ability to cross-match radio continuum sources from surveys such as those proposed for ASKAP and APERTIF, it is clear that similar techniques may also be appropriate for much deeper ($\sim$ 100 nJy) and narrower surveys such as the MeerKAT International Giga-Hertz Tiered Extragalactic Exploration (MIGHTEE) Survey (Jarvis, 2011). Although we currently do not have the necessary data to test how well the LR can recover counterparts to the radio sources at these depths, it is clear that its ability to identify shorter wavelength counterparts becomes worse towards fainter flux densities (e.g. Figure 3.8) due to both the declining signal-to-noise and increasing density of counterpart sources. However resolution of the radio maps is also a contributing factor. The issue of spatial resolution will only become more difficult to deal with at deeper flux densities due to the edging closer to the classical confusion level of $\sim$25 beams per source (Condon, 1974). The current design of MeerKAT, incorporating 20 km maximum baselines, will provide a spatial resolution of $\sim$ 3 arcsec at 1.4 GHz which for a 10μJy flux-density limit corresponds to $\sim$ 40 beams per source according to the simulated skies of Wilman et al. (2010). Thus as we approach the new parameter space in flux-density and survey area offered by MeerKAT, and eventually the SKA, the crucial aspect of telescope design will be how to achieve $\sim$ 1 arcsec resolution coupled with high surface brightness sensitivity.

3.9 *Conclusions*

This chapter has presented a comparison of the infrared counterparts identified by the LR technique to radio sources observed with synthesised beamwidths of 6, 10 and 15 arcsec resolution when matched against a NIR catalogue at depths of $K_{\mathbf{s}} < 22.6$ and 20.0. The results of this analysis indicate that the LR is able to reliably associate nearly all the available radio source counterparts in the NIR catalogue, limited to $K_{\mathrm{s}} < 22.6$, with the appropriate radio source. Furthermore ∼93 and 88% of the identifications made by this technique remain unchanged when matching the lower resolution 10 and 15 arcsec catalogues to the deeper NIR catalogue respectively. At all resolutions the technique delivers a catalogue with a high degree of completeness and a low percentage of contaminating misidentified sources. When matching against the shallower NIR catalogue the fraction of unchanged counterparts increases to 97 and 94% in the 10 and 15 arcsec cases.

Although changes in completeness and contamination fractions in this study were all relatively small as a function of resolution it is clear that both of these quality indicators degrade systematically as the depth of the matching complementary data increases and the resolution of the radio data decreases.

I conducted a brief investigation into the question of unrelated radio sources being blended together at lower resolutions and reducing the completeness achieved by the LR cross-matching technique. This simple analysis concluded that at flux density limits of ∼50 μJy, comparable to the EMU wide-field survey, the contribution of this effect is likely to be small at the level of only a few percent. Finally the distribution of photometric redshifts in the matched catalogues indicates that a significant fraction of the radio sources at z$\gtrsim$1.2 will not be detected in the shallower wide-field VISTA Hemisphere survey.

Chapter 4

Further evolution of radio sources

4.1 *Introduction*

Chapter 2 of this thesis presented an investigation of the cosmic evolution of low luminosity radio sources in a subsection of the XMM-LSS field simultaneously covered by low frequency GMRT observations and the UKIDSS-DXS NIR observations. This investigation suffered from a number of drawbacks including the large uncertainty in the redshift estimates obtained using the K-z relation as well as the small number ($\sim$ 131) of cross-identified radio sources in the field due to the relatively shallow radio and NIR observations. This chapter aims to extend this work and present improved constraints on the evolution of the low-luminosity radio source population by utilising the much deeper VLA radio survey of Bondi et al. (2003) (discussed in chapter 3) in combination with the multi-band photometry available over this region from the VIDEO and CFHTLS-D1 surveys. The radio data thus increases the depth from approximately 1 mJy to $\sim$ 100 μJy compared to the data presented in chapter 2 and can be matched to NIR K-band data to a depth of 22.6 mag (AB), an improvement of the order of $\sim$1.5 mags over the $\sim$21.0 (AB) completeness limit of the UKIDSS DXS survey. As discussed in chapter 3 the depth of the NIR data together with the improved positional accuracy of the VLA observations, 1σ positional accuracies of $0.72''$ rather than $2''$, allowed me to use the LR to identify counterparts to a large fraction of the radio sources. Thus this chapter makes use of a considerably expanded sample of over 900 cross-matched radio sources. A further improvement is the use of SED fitting techniques and multi-band ($\geq$ 9) photometry to estimate photometric redshifts, these redshift estimates have considerably smaller uncertainties than those produced via the K-z relation.

The drawback that this investigation suffers from is its relatively small area ($\sim$ 1 square degree). As such this dataset will not detect a statistically significant number of the intrinsically rarer high-power radio sources and thus any study of their evolutionary properties will clearly be limited. Small area surveys are also vulnerable to cosmic variance, which complicates the generalisation of specific results in this field to the radio population as a whole. Small areas ($\leq$2 degrees^2) have been a feature of most current sub-mJy radio surveys due the sensitivity limits of existing radio telescopes. The need to expand studies of the faint radio source population to larger areas is a primary motivation for the construction of the next generation of radio telescopes, the study presented in this chapter thus joins the swelling ranks of detailed small area studies of faint radio sources which hope to preview the results of these much anticipated surveys.

An important new consideration is that, contrary to the case in chapter 2, the deeper radio observations used in this improved study are no longer primarily sensitive to radio-loud AGN but will also detect a significant number of star-forming galaxies. The contribution of star-forming galaxies will only become significant at lower, sub-mJy, flux densities. As it is not trivial to separate these populations this chapter will only attempt to constrain the evolution of the luminosity function of the combined population of star-forming galaxies and AGN using similar techniques to those employed in chapter 2. The chapter is outlined as follows: section 4.2 outlines additional details of the radio observations used in the RLF determination. Section 4.3 provides details of cross-matching the radio sources with the multi-band optical and NIR data. Section 4.4 outlines the procedure used to obtain photometric redshift estimates[1] and provides details on the expected accuracy of the redshifts estimated via this technique. The radio luminosity function and its evolution are presented in section 4.5 and section 4.6 presents my concluding remarks.

4.2 *Radio observations*

Details of the VLA observations used during the investigation of the LR cross-matching technique were discussed in section 3.1. Further observations of this field were performed by Bondi et al. (2007) using the GMRT at 610 MHz. The GMRT observations covered the whole square degree of interest with 5 pointings observed for ∼5.5 hours each and were used to produce a catalogue of 514 radio sources complete to a limiting flux density of ∼200μJy. The catalogue extracted from the GMRT observations was produced in an identical manner to the VLA catalogue in Bondi et al. (2003). The GMRT has a synthesised beam of ∼6 $''$ at 610 MHz, as such

---

[1] This description is included for purposes of clarity and completeness as the photometric redshifts were produced by the VIDEO survey team and do not form part of the work completed for this thesis.

the resolutions of the 610 and 1400 MHz observations over this field are very well matched allowing Bondi et al. (2007) to obtain accurate spectral index estimates for the VLA sources detected in the low frequency observations. The 1400 MHz sources in the VLA catalogue were associated with their low frequency counterparts by searching for 610 MHz sources within a $3''$ search radius. Using this procedure 448 sources were found to have counterparts above the 5σ noise limit of the 610 MHz image, 293 sources had counterparts detected with peak fluxes in the range 3–5σ and a further 313 sources in the VLA catalogue were not detected in the GMRT observations. Upper limits on the spectral indices of the non-detected sources were estimated from the 3σ noise levels of the GMRT image at the position of the VLA radio sources (Bondi et al., 2007). Throughout this chapter, wherever a spectral index estimate is required, e.g. in the case of determining radio luminosities, I use the estimates and upper limits obtained via this procedure.

Although the noise distribution of the 1400 MHz observations of this field was fairly uniform, strong sources still affected the dynamic range in several regions of the image. Figure 4.1 thus presents the visibility area as a function of flux density for the VLA survey which can be seen to rise very rapidly to one square degree between 0.06 and 0.1 mJy. This visibility area was used to correct for incompleteness at the faintest flux densities by estimating the generalised accessible volume parameter V_a as described in section 2.6.3 of chapter 2.

4.3 *Cross-matching*

I used the cross-matched catalogue produced by the LR in chapter 3 to match single-component radio sources with their counterparts in the combined VIDEO-CFHTLS multi-band catalogue. Radio sources not included in the LR matching procedure due to their unusual morphologies or their status as a multiple component radio source were matched using the visual inspection method of plotting the radio contours over the VIDEO K_s band images. A further 10 radio sources were associated with counterparts due to this process.

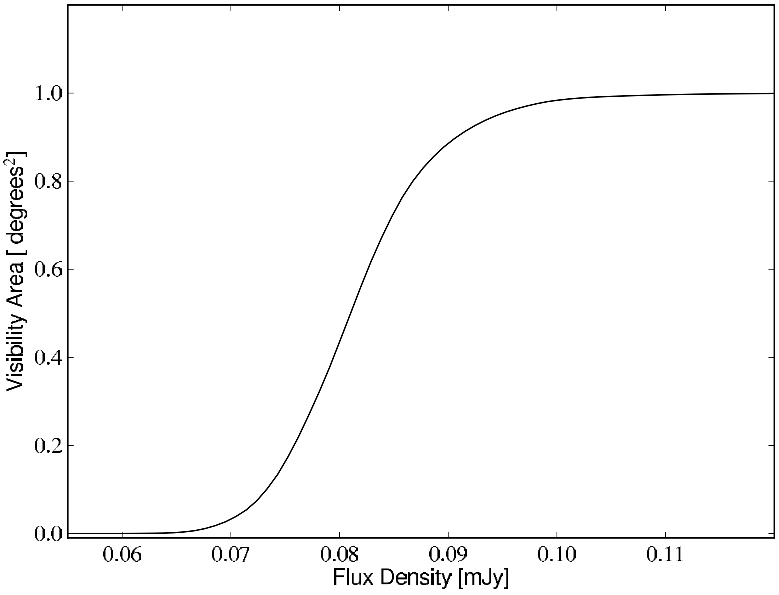

Figure 4.1: The visibility area as a function of flux density for the Bondi et al. (2003) VLA survey.

4.4 *Photometric redshifts*

Redshift estimates are a fundamental prerequisite for a wide-range of proposed scientific enquiries with SKA precursor telescopes. These include detailed studies of the processes that govern the evolution of accretion and star-formation activity in the universe, using radio sources to trace the evolution of large scale structure in the universe and determining a range of cosmological parameters via Cosmic Magnification and Integrated Sachs-Wolf effects (see Raccanelli et al., 2012). The potential to supply accurate redshift estimates for a large sample of galaxies is thus an exceptionally valuable enhancement in scientific return provided by cross-matching to multi-wavelength datasets. Follow up spectroscopic observations at the position of the counterpart source provide the most accurate redshifts, although even this gold-standard technique is acknowledged to be prone to error when observing very faint objects at the limits of the spectrograph (Fernández-Soto et al., 2001). Unfortunately improved accuracy demands a heavy price in the form of increased observing time, as increased resolution results in a corresponding decrease in the signal to noise detected per resolution element. A typical faint object spectroscopic observation ($\frac{\lambda}{\Delta\lambda}$ ~1000) thus requires an order of magnitude increase in observing time over a typical broad band photometric observation ($\frac{\lambda}{\Delta\lambda}$ ~5) to obtain a detection with comparable signal to noise. As such photometric surveys will always provide wider and deeper coverage than the largest and deepest spectroscopic surveys. Photometric redshifts thus represent the most efficient means to obtain redshifts for a large fraction of galaxies detected in planned very deep surveys and are the only means of determining redshifts for the very faintest sources with magnitudes below the spectroscopic limit. Photometric redshift estimation operates by identifying strong spectral features in the source's spectral energy distribution (SED), such as the Lyman and Balmer continuum breaks, which are still discernible in the observed photometry after convolution with the filter transmission profile. These features will be shifted to higher wavelengths at high redshift and as such their position in the detected photometry can be used to obtain a rough estimate of redshift. This method is therefore best used at redshifts where these strong identifiable features continue to be well sampled by the available multi-band photometry.

Methods of photometric redshift estimation generally fall into one of two broad categories, empirical or template-fitting based methods. Empirical methods use a large 'training set' of spectroscopic observations to determine the relationships between redshift and observed magnitudes and colours, these methods include artificial neural networks and other machine learning techniques (see Firth et al., 2003; Vanzella et al., 2004; Bonfield et al., 2010) as well as empirical reconstructions of the colour-redshift relation (see Sawicki et al., 1997; Wang et al., 1998). This method can produce more precise redshift estimates when the 'training set' is sufficiently representative of the sample for which you require redshifts. The obvious drawback of this method is that it requires the *a priori* existence of a suitable reference training set, furthermore such a training set will unavoidably be composed of brighter objects and empirical relationships inferred from it may not necessarily be reliably extended to fainter magnitudes.

Template fitting methods operate by assuming that the intrinsic SED of the observed sources can be represented by a set of input reference galaxy templates, these may be real observed spectra or synthetic galaxy templates predicted from theoretical models. The theoretical flux detected from a reference template source at redshift z is then constructed for each filter by redshifting the template and multiplying it by the instrument filter response curves. By comparing these theoretical fluxes with the actual observed photometry it is possible to use a straightforward χ^2 minimisation routine to determine the most likely template and redshift. The template fitting method is widely used (e.g. HYPERZ; Bolzonella et al., 2000; IMPZ;

Babbedge et al., 2004; EAzY; Brammer et al., 2008; Le Phare; Ilbert et al., 2006), is straightforward to implement and has the advantage that it does not require ancillary spectroscopic data. Its degree of success is however dependent on the appropriateness of the input template library, i.e. how well they reproduce the emission profiles of individual classes of galaxies and whether they represent the full range of spectral types of galaxies present in the survey. It is of particular concern that empirical templates are necessarily derived from observations of bright local galaxies and these may not provide accurate representations of galaxies at higher redshifts. On the other hand theoretical SEDs, capable of modelling a wide range of evolutionary scenarios, introduce extra degrees of freedom in the fitting procedure possibly creating degeneracies in the parameter space and degrading the final quality of the redshift estimates. Biases may also occur due to imperfect characterisations of the instrument response curves. A number of hybrid methods have been developed to improve on this traditional template fitting method. These make use of available spectroscopic samples to optimise the input template libraries (ZEBRA; Feldmann et al., 2006; Assef et al., 2008), to apply Bayesian priors to the expected redshift distribution (BPZ Benítez, 2000; Mobasher et al., 2004) or to remove systematic offsets in the photometry (Le Phare; Ilbert et al., 2006).

4.4.1 *Photometric redshifts in the combined VIDEO-CFHTLS survey*

The VIDEO survey team has derived photometric redshift estimates for the combined VIDEO–CFHTLS-D1 survey using the publicly available redshift code Le Phare[2] (Ilbert et al., 2006). This code makes use of the template fitting method discussed in the previous section with a number of optional refinements including the ability to use spectroscopic samples to calibrate and minimise systematic offsets between the photometric bands and to implement a Bayesian prior on the redshift probability distribution similar to that employed by Benítez (2000).

The VIDEO photometric redshifts were estimated using the optimised galaxy templates produced by Arnouts et al. (2007). These are based on the four observed spectra in Coleman et al. (1980) an elliptical (Ell), two spirals (Sbc,Scd) and and irregular galaxy (Irr) as well as two observed starburst (SB) templates from Kinney et al. (1996). These templates have been linearly extrapolated to NIR and ultraviolet wavelengths using the GISSEL synthetic models (Bruzual and Charlot, 2003) and optimised using data from the VIMOS Very Large Telescope

---

[2] http://www.cfht.hawaii.edu/ arnouts/LEPHARE/lephare.html

(VLT) Deep Survey (VVDS; Le Fèvre et al., 2004, 2005). This is a deep spectroscopic survey complete to a depth of I_{AB} <24.0 undertaken with the VIMOS VLT telescope.

The process of constructing these optimised templates is described in detail in Ilbert et al. (2006), they proceed by determining rest-frame SED's for all objects with secure redshifts and separating these into 4 categories based on the best-fit Coleman et al. (1980) template. Optimised templates are constructed from the median flux of the rest-frame spectra in each of these four categories, at wavelengths not sampled by the spectroscopic survey the original extrapolated Bruzual and Charlot (2003) flux was retained. The two starburst galaxy templates were not optimised in order to retain emission lines. The final set of optimised templates are linearly interpolated to produce 64 reference templates used in the photometric redshift fitting procedure, these are plotted in figure 4.2. For Scd and later spectral types the fitting also allowed for dust attenuation with permitted reddening excesses E(B-V) of 0.0, 0.05, 0.1, 0.15, 0.2 and 0.3. Dust attenuation was modelled using the interstellar extinction law measured by Prevot et al. (1984) in the Small Magellanic Cloud. The opacity of the intergalactic medium is also included according to prescriptions of Madau (1995).

The templates were redshifted in increments of Δz ~0.04 and convolved the u^*,g',r',i',z' MegaCAM and the Y,J,H,K_s VISTA instrumental response curves to produce a set of theoretical observed fluxes for all templates, redshifts and reddening excesses $\mathrm{F}_{pred}(z, T, \mathrm{E(B\text{-}V)})$. The MegaCAM and VISTA transmission curves are presented in figure 4.3. The most likely redshift, template and level of dust extinction is then determined by comparison with the observed fluxes in these filters and minimising the expression:

$$\chi^2(z, T, \mathrm{E(B\text{-}V)}) = \sum_{f=1}^{N_f} \left(\frac{F^f_{obs} - A \times F^f_{pred}(z, T, \mathrm{E(B\text{-}V)})}{\sigma^f_{obs}} \right)^2 \tag{4.1}$$

where F^f_{obs} and σ^f_{obs} are the observed flux and associated error in the filter f. The A term is free parameter in the minimisation and is used to scale the arbitrary flux densities of the input templates to the observed flux. Redshifts were estimated from photometry measured in 2 arcsec apertures and the associated errors were determined by measuring the rms noise in randomly placed apertures of the same size and adding Poissonian noise. To adjust for uncertainties in the relative calibration of the observed bands additional uncertainties of 0.01 magnitudes were added in quadrature to the measured errors.

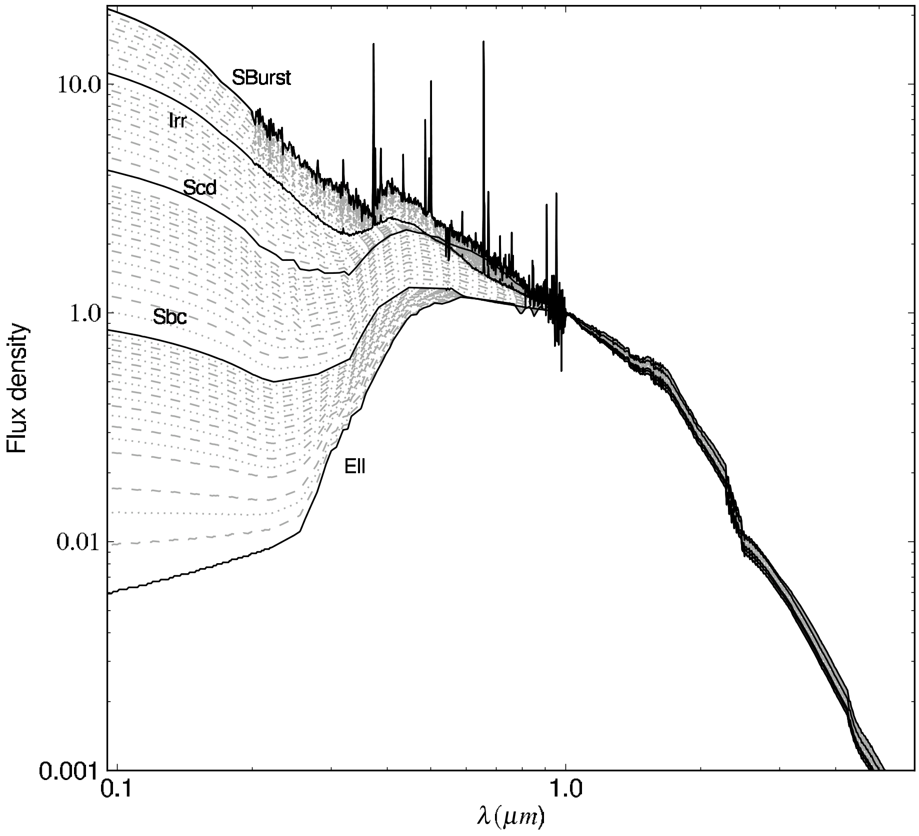

Figure 4.2: Empirical galaxy template SED library used by Le Phare in estimating photometric redshifts. The original optimised templates from Arnouts et al. (2007) are plotted as solid black lines and all extrapolated templates are plotted as grey dotted and dashed lines.

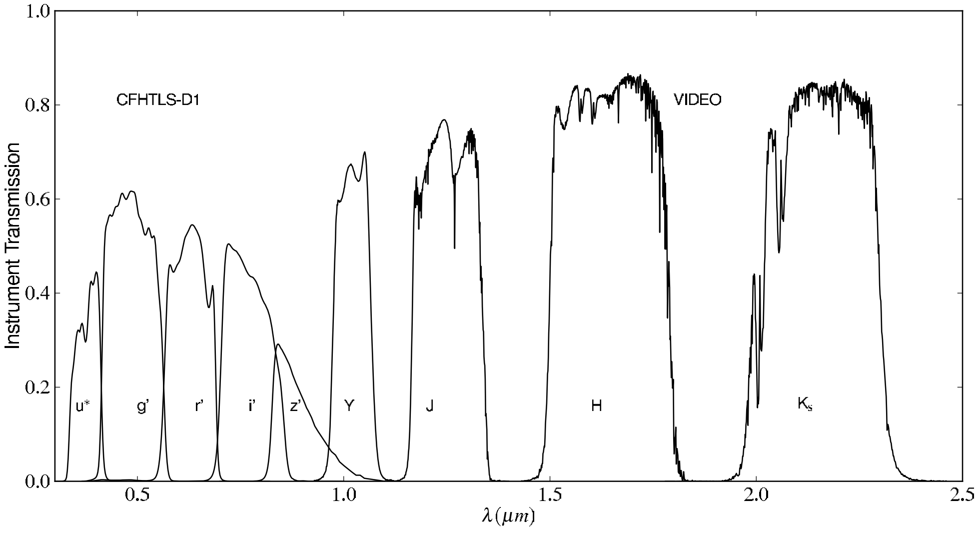

Figure 4.3: Instrumental response profiles for the 9 bands used in photometric redshift determination.

Table 4.1: Table of systematic offsets between the nine bands used to estimate photometric redshifts. These were determined by calibrating against a sample of approximately 3000 objects with spectroscopic redshifts in the VVDS.

Filter	offset [mag]	Filter	offset [mag]
u^*	0.162	Y	0.084
g'	-0.025	J	0.076
r'	-0.042	H	0.111
i'	-0.108	K_{s}	0.093
z'	-0.071		

Systematic offsets in the photometric calibrations were also removed using a sample of approximately 3000 objects with spectroscopic redshifts in the VVDS-DEEP survey. This is achieved by determining the best fitting template when fixed at the spectroscopic redshift and calculating the predicted observed flux for this template as $A \times F^f_{obs}$, where A is the scaling factor in equation 4.1. The systematic offsets in each filter s^f are then found by minimising :

$$\psi^2 = \sum_0^{N\mathrm{gal}} \left(\frac{A \times F^f_{pred} 10^{-0.4 s^f} - F^f_{obs}}{\sigma^f_{obs}} \right)^2 \tag{4.2}$$

where s^f would be a zero-mean random Gaussian variable for no systematic offset. These systematic offsets for the VIDEO survey were all found to be small and are listed in table 4.1,

To account for stars and quasars detected in the VIDEO survey the Le Phare code independently fits a set of stellar and AGN templates to the observed photometry in the same manner as equation 4.1 and reports the results as χ_{star} and χ_{QSO}. In the case of the quasar templates this process also reports the most likely redshift for a source with an intrinsic SED corresponding to the best fitting AGN template z_{QSO}. The AGN templates are those used and described in detail in Polletta et al. (2007), the library consists of empirically determined spectra for 3 Type 1 AGNs, 5 Type 2 AGN and two composite AGN and starburst galaxy objects. Plots of their SED's are presented in figure 4.4.

Photometric redshifts determined from AGN templates are known to be much less reliable than those obtained for galaxies due the absence of strong spectral break features which provide the strongest constraints in the minimisation procedure (see e.g. Richards et al., 2001; Babbedge et al., 2004; Mobasher et al., 2004; Polletta et al., 2007). Quasar SED's are generally well represented by a power-law continuum overlaid with a series of broad emission line

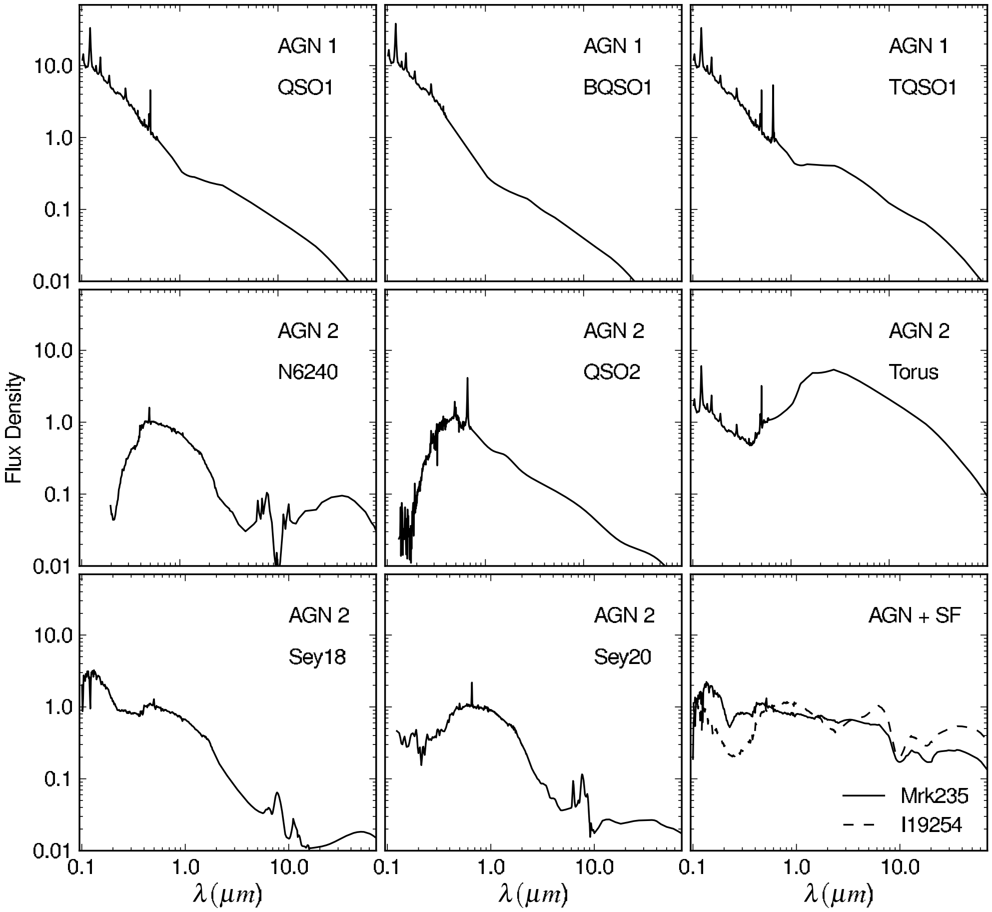

Figure 4.4: Empirical AGN templates from Polletta et al. (2007) used to determine redshifts for AGN in the VIDEO survey. The first top three are Type 1 AGN, the next five are Type 2 AGN and the plot in the bottom right corner are the two composite AGN and starburst galaxy SED's. The names of the templates in the original library are given in the top right corners of each plot.

features. As the continuum spectrum is approximately invariant under redshift, constraints in the minimisation procedure rely on these emission features containing sufficient flux to influence the broad-band photometric measurements. These emission lines are difficult to identify and localise accurately based solely on the final integrated flux measurements and may also fall between gaps in the filter coverage. At higher redshifts Lyα forest absorption provides an additional redshift dependent feature in the SED which can be used to improve quasar photometric redshift estimates. Further sources of error include the possibility of strong contamination of the AGN SED by the host galaxy as well as the intrinsic variability of quasars. As most surveys have non-simultaneous photometry this variability hampers the construction of a typical snapshot SED for fitting. All of these factors culminate in the effect that the most accurate photometric redshifts for quasars using a variety of complex techniques to mitigate these limitations produce z_{qso} with dispersions σ_z of $\sim$0.35 (see Ball et al., 2008; Salvato et al., 2009, 2011) whilst much simpler techniques routinely report estimates σ_z $\sim$0.1 or even much lower values for normal (inactive) galaxy samples (Wolf et al., 2004; Ilbert et al., 2006, 2009; Cardamone et al., 2010). It is thus important to bear this likely reduced accuracy in mind while classifying sources and determining the reliability of the final redshift estimates.

4.4.2 *Comparison with spectroscopic redshifts*

Despite advances in the technique, photometric redshifts are still less accurate than spectroscopic redshifts and this method is known to produce ‘catastrophically’ poor redshift estimates for some fraction of the sample. The ‘catastrophic’ failure label refers to sources whose predicted redshifts differ from their spectroscopic redshifts by a margin considerably greater than the expected/predicted uncertainties. It is thus necessary to evaluate the expected error and fraction of these outliers in the sample before proceeding with any scientific investigation. The most direct method of determining the accuracy of a photometric redshift procedure is by comparison with available spectroscopic data and figure 4.5 presents such a comparison for galaxies with counterparts in the VVDS (Le Fèvre et al., 2005).

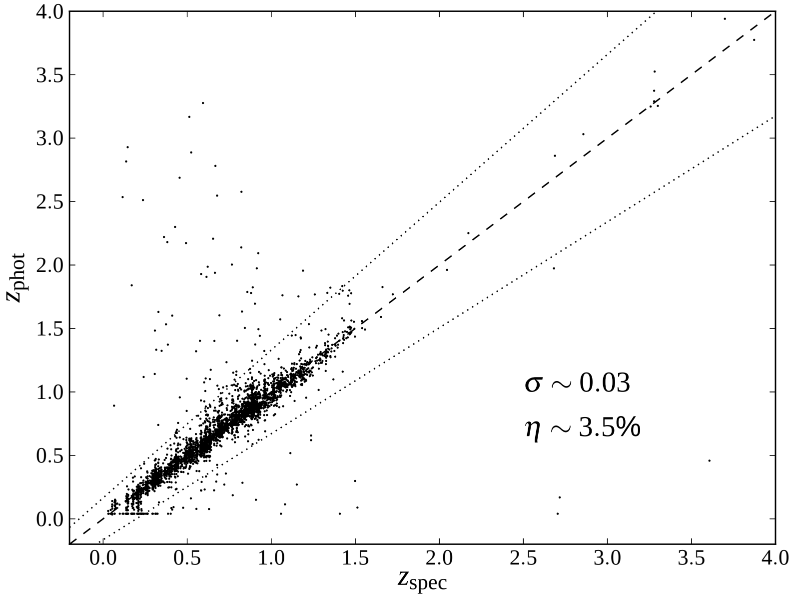

Figure 4.5: Comparison of secure spectroscopic redshifts z_{spec} (flags 3,4) in the VVDS-DEEP surveys with photometric estimates produced by LE PHARE z_{phot}. After removing outliers this sample has $\frac{\Delta z}{(1+z)}$ variance of σ ∼0.03 and only 3.5% of the objects have 'catastrophic' failures with $\frac{\Delta z}{(1+z)} > 5\sigma$. The two dotted guiding lines represent the calculated 5σ error on the photometric redshifts.

4.4.2.1 *The galaxy sample*

Counterparts were identified by cross-matching the VIDEO and VVDS source positions to within 1 arcsec tolerance. The VVDS catalogue provides quality flags indicating confidence in the reported redshift. Quality flags 2, 3 and 4 indicate confidence levels of 75, 85 and 100% respectively whilst objects with a flag of 1 have only indicative redshifts based on the continuum with very few supporting spectral features (∼ 50% confidence). The least secure redshifts are those with quality flag 9 which are based on only a single emission line assigned a tentative redshift. To evaluate the accuracy of the VIDEO photometric redshifts I neglected sources in the VVDS sample with less secure redshifts and retained only those with quality flags of 3 & 4. I also removed objects classified as stars by the colour selection criteria in section 3.2.1 and sources classified as quasars in the VVDS survey. This provided a sample of ∼ 3837 secure spectroscopic redshifts for comparison. After removing outliers, the variance in $\frac{\Delta z}{(1+z)}$[3] was found to be ∼0.03 and the fraction of outliers η, defined as sources with $\frac{\Delta_z}{(1+z)} > 5\sigma$, was 3.5%. To investigate whether the fraction of outliers increases towards fainter magnitudes

---

[3] $\Delta z = z_{spec} - z_{phot}$

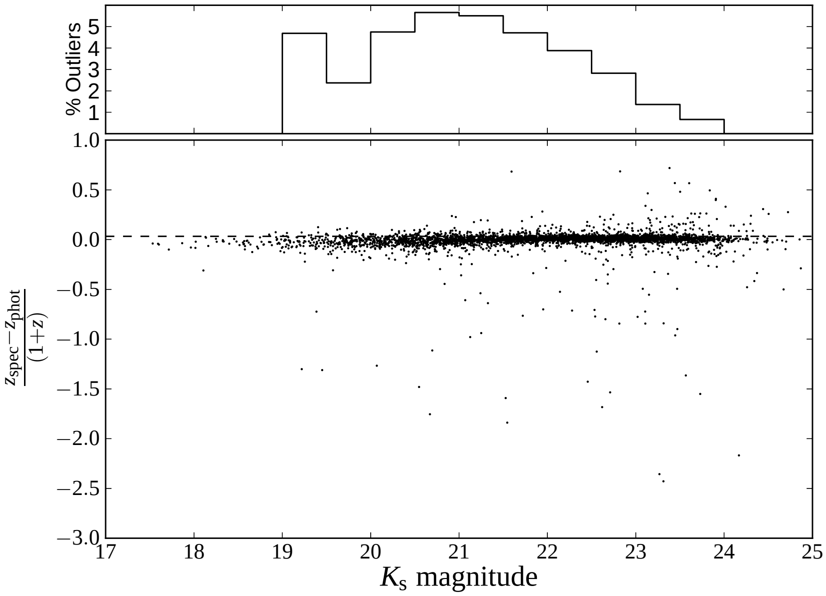

Figure 4.6: The error in photometric redshifts $\frac{\Delta z}{(1+z)}$ as a function of K_{s}-magnitude for objects with secure spectroscopic redshifts. The histogram in the top plot gives the fraction of outliers as a function of magnitude.

figure 4.6 presents $\frac{\Delta_z}{(1+z)}$ and the fraction of outliers as a function of K_{s} magnitude. This plot demonstrates that the fraction of outliers does not increase significantly towards fainter K_{s}-magnitudes thus the majority of these outliers are not produced by greater uncertainties in the photometry at faint magnitudes. As many objects at K_s ∼23 will be too faint in i band to be included in the VVDS spectroscopic sample the errors derived from this comparison should be considered as lower limits on the true errors. The photometric redshifts will be worse for objects which are faint in both the optical and near-infrared.

Figures 4.5 and 4.6 also indicate that majority of failures scatter objects with low intrinsic redshifts upwards to high redshift whilst comparatively few objects with high spectroscopic redshifts are assigned low photometric redshifts. This biased behaviour of the method has implications for studies of cosmic evolution as it systematically reduces the number of observed sources at low redshift whilst simultaneously enhancing the number of observed sources at higher redshifts. The effect, whilst systematic, is nevertheless quite small and as such should not have a large impact on the conclusions of this study. However as the total number of objects at high redshift $2 \leq z \leq 3$ is small and a larger fraction of these are catastrophic. Future work should aim to determine the likely impact of this source of error on the derived luminosity function at higher redshifts.

4.4.2.2 *The quasar sample*

As discussed in section 4.4.1 the redshift estimates for quasars detected in the VIDEO survey are likely to be less accurate than those for normal galaxies and I thus present a separate analysis of the spectroscopic redshifts of quasars. The VIDEO data has two independent estimates of photometric redshifts based on separate input SED libraries, a library composed of normal galaxies and another of active galactic nuclei and hybrid AGN-starburst galaxies. I compared these independent estimates of photometric redshift to determine which of these two libraries produces the most reliable results for quasars in the VIDEO survey. For clarity photometric redshifts estimated from the quasar template library are referred to as z_{qso} and those produced from the galaxy library as z_{phot} throughout the rest of this section. The VVDS has 45 quasars with accurate spectroscopic redshifts (flags 3 & 4), these are identified based on broad emission line features detected in their spectra. These known quasar redshifts are compared with galaxy and AGN template photometric redshifts in figure 4.7. In this figure there is a clearly discernible threshold in z_{phot} and z_{qso} below which the redshift estimates are unreliable. Reassuringly, remaining sources above the threshold are well correlated with spectroscopic redshift, although the relationship has a much larger variance than that determined for the normal galaxy population. After removing sources below the threshold values, which is slightly higher for the z_{qso} estimates, and clipping outliers the $\frac{z_{spec}-z_{phot}}{(1+z)}$ and $\frac{z_{spec}-z_{qso}}{(1+z)}$ distributions have measured variances of σ_{phot} and σ_{qso} of ~0.26 and ~0.21 respectively. These distributions are presented in figures 4.7 and 4.8. The total fraction of 5σ outliers, excluding sources below the thresholds, is low for both samples at 2.8% and 7.4% for galaxy and quasar templates respectively. The threshold values can only be determined very approximately because of the small number of quasars but seem consistent with values ~0.2 for z_{phot} and ~0.32 for z_{qso}. Further investigations demonstrated that for both samples $\frac{\Delta z}{(1+z)}$ does not depend on magnitude or colour. The most notable difference produced by the two libraries is that a larger number of sources fall below the threshold for bad redshift estimates when using the quasar templates, there are 18 (40%) such sub-threshold sources for quasars and only 8 (17%) in the galaxy based estimates.

To investigate the origin of the larger number of failures in the z_{qso} case I examined the continuum emission in the spectra of the quasar candidates and separated them into sources with strong blue emission profiles and those with flattened or weak continuum emission. The latter case corresponds to obscured quasars where the host galaxy emission may contribute significantly to the total SED resulting in a poor fit to the templates in the AGN library. Figure 4.9 presents the photometric versus spectrosopic redshifts of these two quasar classes and demonstrates that, contrary to expectation, the reddened obscured quasars are not associated with a greater number of failures in the photometric redshift procedure, thus the origin of these failures remains unclear.

Based solely on the observation that these produced fewer failed redshift estimates I elected to use the galaxy based redshift estimates for quasars in the radio sample and reject quasar objects with z_{phot} <0.2.

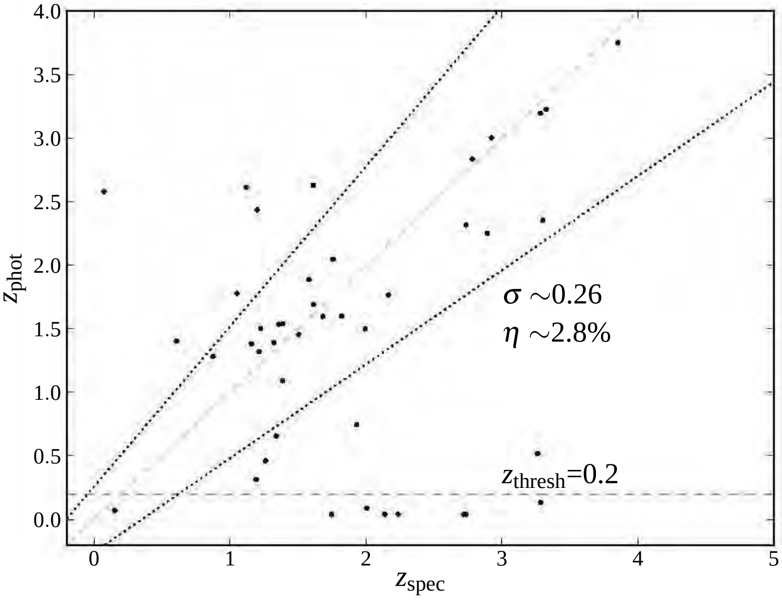

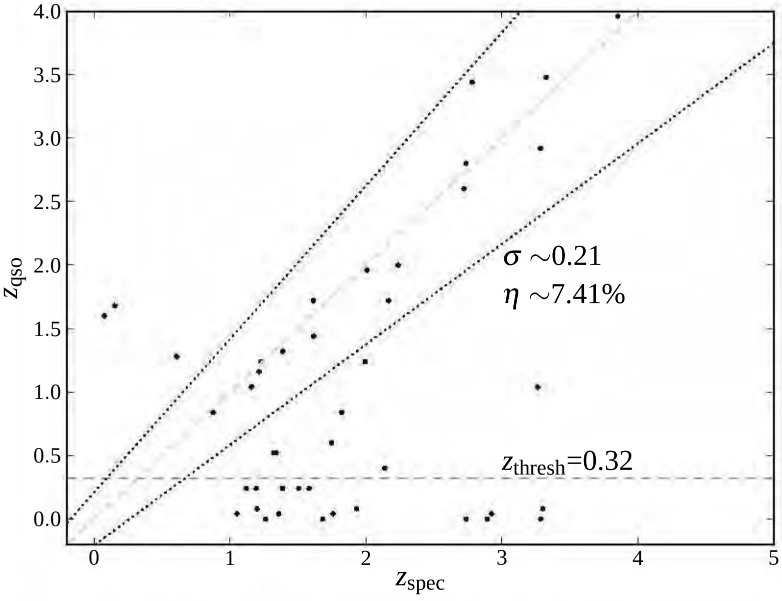

Figure 4.7: Top: Photometric redshifts of quasars estimated using galaxy templates. Photometric redshifts below the z_{thresh} level, plotted as a dashed line, are clearly not reliable. Excluding these sources produces an estimated dispersion in $\frac{\Delta_z}{(1+z)}$ of ∼0.26 with 2.8% 5σ outliers. Dotted lines are plotted at 1σ. Bottom: Photometric redshifts of quasars estimated using quasar templates. Photometric redshifts below the z_{thresh} level are clearly not reliable. Excluding these sources produces an estimated dispersion in $\frac{\Delta_z}{(1+z)}$ of ∼0.21 with 7.4% 5σ outliers. Dotted lines are plotted at 1σ.

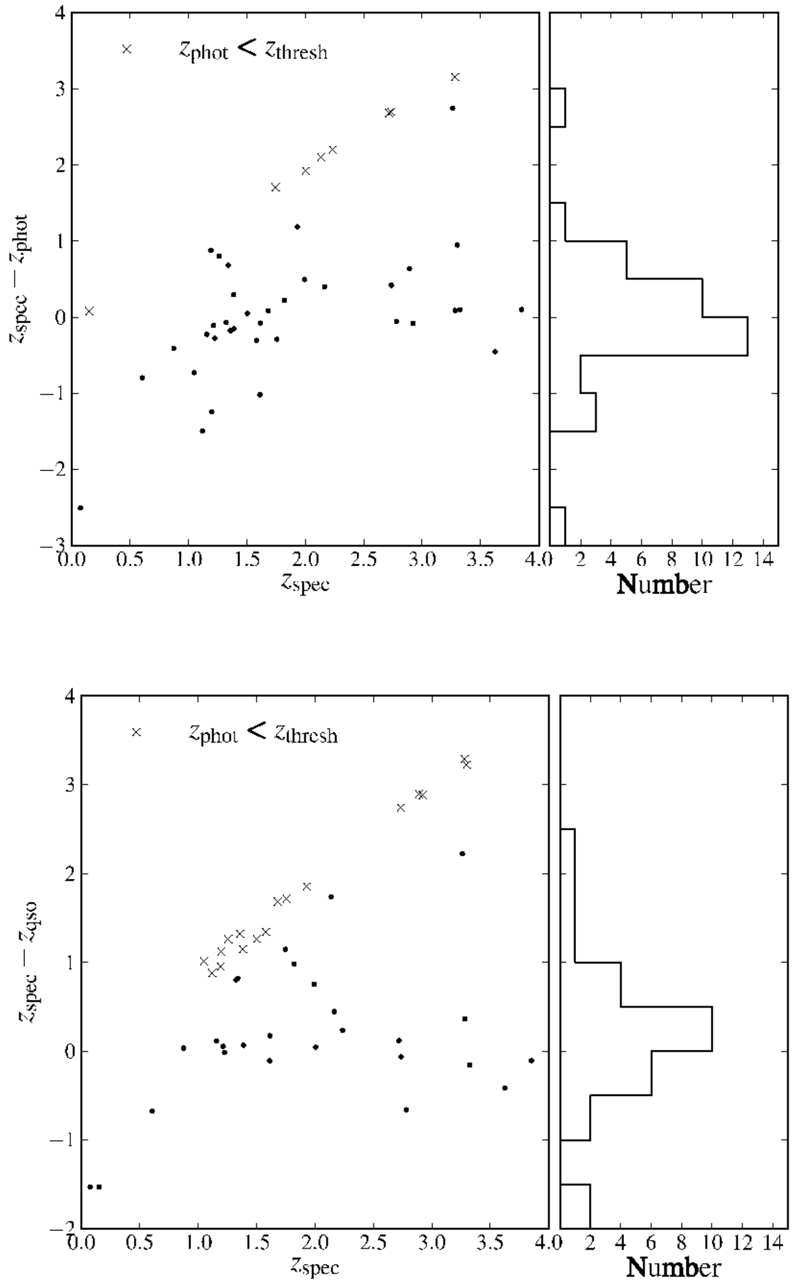

Figure 4.8: Top: $z_{spec} - z_{phot}$ estimated using galaxy templates for quasars in the VVDS. Bottom:$z_{spec} - z_{qso}$ estimated using quasar templates for quasars in the VVDS. Photometric redshifts below the z_{thresh} level in figure 4.7 are plotted as crosses, these are not included in the histogram presented in the right hand side of the figure.

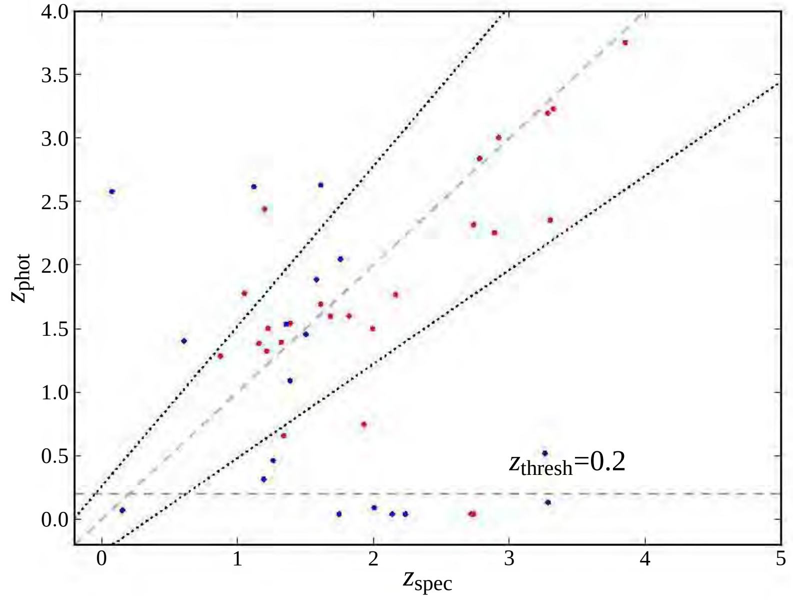

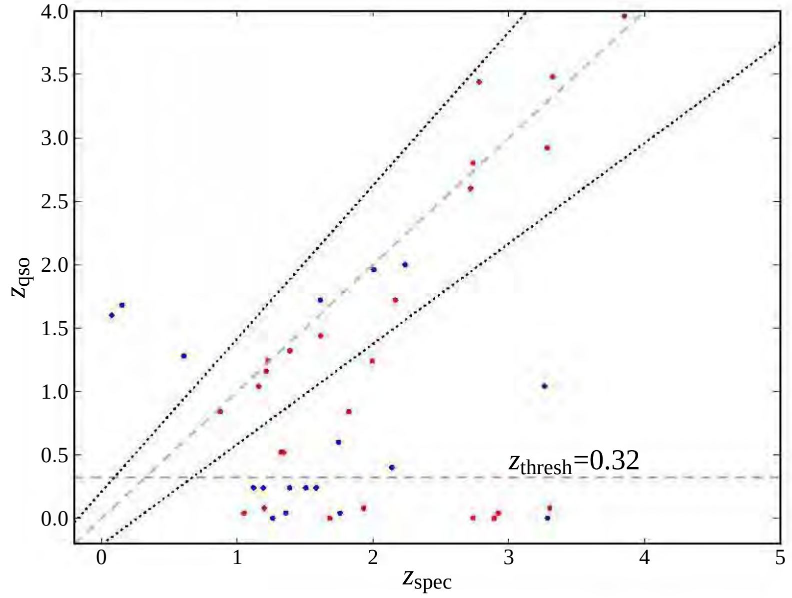

Figure 4.9: Top: Photometric redshifts of quasars estimated using galaxy templates Bottom: Photometric redshifts of quasars estimated using quasar templates, quasars with strong blue continua are plotted in blue, while those with flattened or weak continua are in red.

4.4.3 *Predicted errors*

Comparison with spectroscopic redshifts provides an important characterization of the variance and fraction of failures in the z_{phot} estimates, however this process cannot be used to identify the photometric redshifts in the full sample which are most likely to be unreliable. Extra information regarding the reliability of individual redshift estimates can be extracted by considering whether the fitting procedure used to produce it was well constrained by the available photometry or not. A measure of the uncertainty in the photometric redshift estimate can thus be obtained directly from the fitting χ^2 distribution and the full redshift Probability Distribution Function (zPDF) for each object can be calculated as:

$$z\mathrm{PDF} \propto \exp\left(-\frac{\chi^2(\mathrm{z})}{2}\right) \tag{4.3}$$

where the total zPDF is subsequently normalised to unity over the full range of allowed redshifts. A second redshift solution is likely when a second peak is detected in the zPDF above a given threshold, or put in another manner when a different combination of parameters (template, dust extinction and redshift) provided an almost equally good fit to the observed photometry. Results from Ilbert et al. (2006) show that when such a second peak is detected with a probability of greater than 5% the fraction of 'catastrophic' errors increases dramatically, from approximately 7% to 44% in their sample. Secondary peaks usually occur due to a misidentification of the Lyman and Balmer break features. An estimate of the error of each derived redshift is determined from the χ^2 distribution of the fitting procedure, 1σ errors are determined as the redshift corresponding to a χ^2 value of:

$$\chi^2(z) = \chi^2_{min} \pm \Delta\chi^2 \tag{4.4}$$

where $\Delta\chi^2$=1, 3σ confidence intervals are determined at an increment of $\Delta\chi^2$=9. These error estimates can be useful in the case of selecting a sub-sample of objects, with minimal spectroscopic data, where the possibility exists that the criteria used to define the sample is selecting some particularly poorly constrained region of the full dataset. In this instance larger error estimates provided by equation 4.4 could be properly accounted for before drawing final conclusions. Errors produced by this method do not account for intrinsic uncertainties in the photometry not included in the measured photometric errors such as those caused by blending or the presence of bright neighbours, nor can they account for inadequacies in the input template library. They are nevertheless useful indicators of reliability in the absence of spectroscopic data and Ilbert et al. (2006) demonstrated that 68% and 92% of the spectroscopic redshifts are located within the 1σ and 3σ errors respectively.

Figures 4.10 and 4.11 present comparisons of the spectroscopic and photometric redshifts in the VIDEO survey with the 1σ error bars overlaid for galaxies and quasars. It is clear from figure 4.10 that for galaxies a large fraction of the outlier sources are accompanied by larger error estimates, however some non-negligible fraction of the outlier sources have misleadingly low error estimates. The contribution and effect of such uncharacterised bad redshift estimates in any sample is clearly difficult to estimate and scales with total number of expected outliers. Figure 4.10 presents a comparison of the distribution of errors for sources whose $\frac{\Delta z}{(1+z)}$ are greater and less than the 5σ variance of the sample, and demonstrates that $\sim 50\%$ of the outlier sources are not identified as objects with less certain χ^2 fits. Additionally figure 4.11 demonstrates that χ^2 errors for quasars produced by fitting either galaxy/quasar templates are hopelessly optimistic and not indicative of the true reliability of the photometric estimate. This is to be expected as the dominant source of errors in this case are the inadequacies of the input templates. These figures serve as a powerful illustration of a point made earlier in this discussion about the limitations of error estimates derived solely from the fitting procedures.

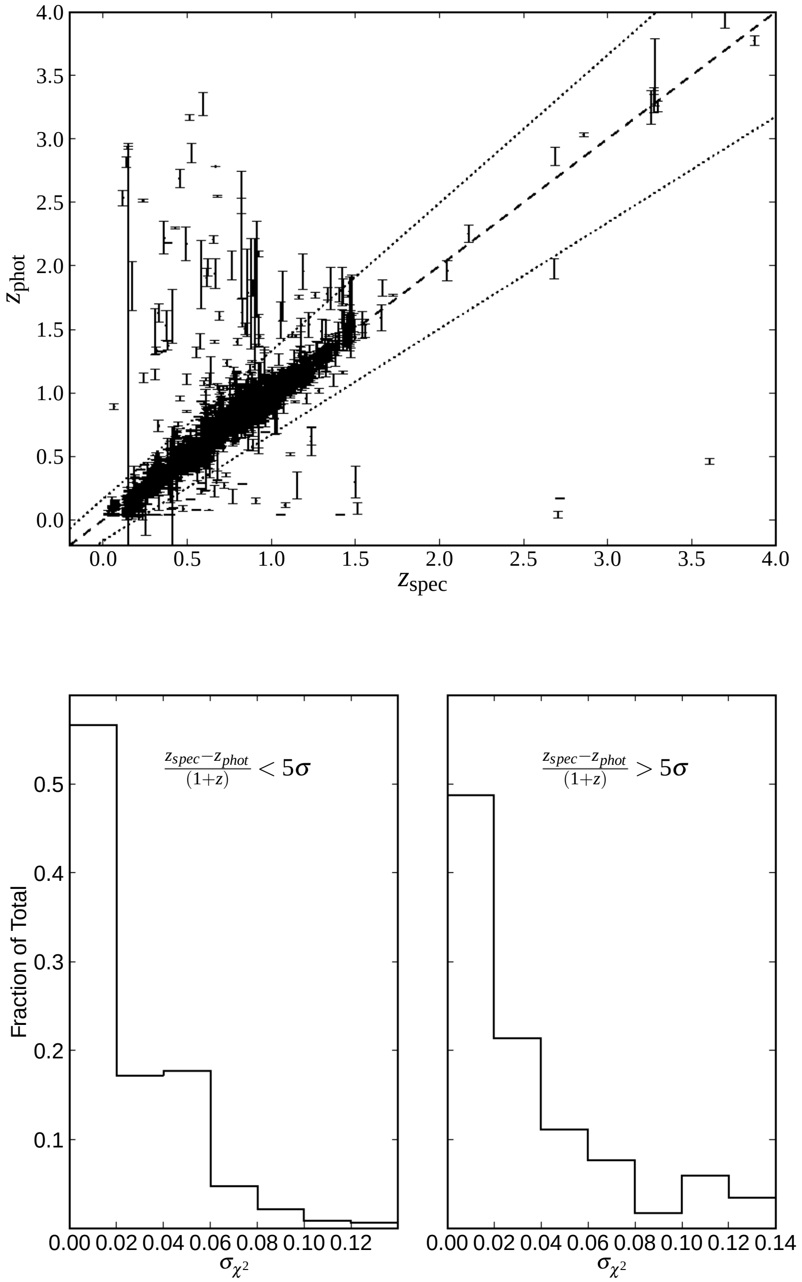

Figure 4.10: Top:Comparison of spectroscopic and photometric redshifts for galaxies with secure redshifts in the VVDS including error bars σ estimated from the χ^2 fitting procedure as in equation. Bottom: Comparison of the distribution of errors estimated from the χ^2 distribution for sources with $\frac{\Delta z}{(1+z)} < 5\sigma$ and $\frac{\Delta z}{(1+z)} > 5\sigma$

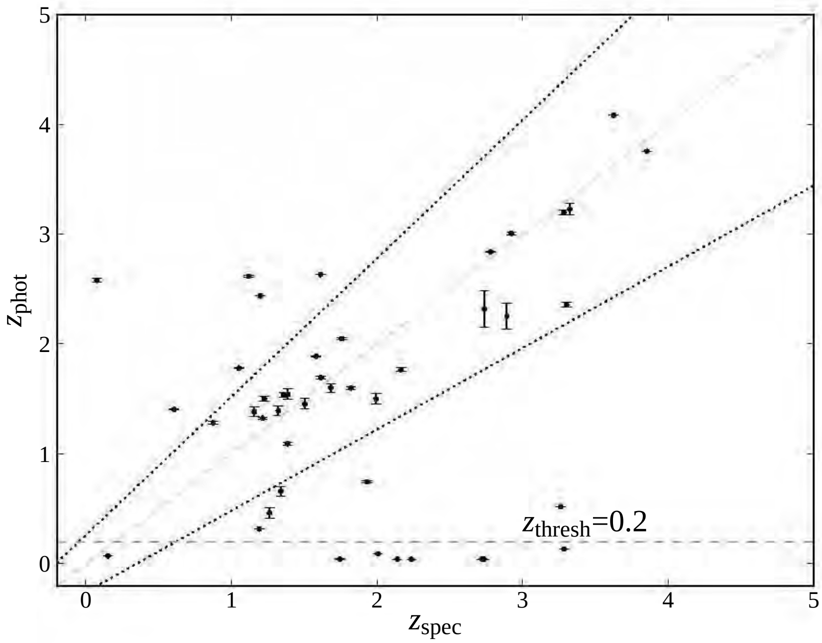

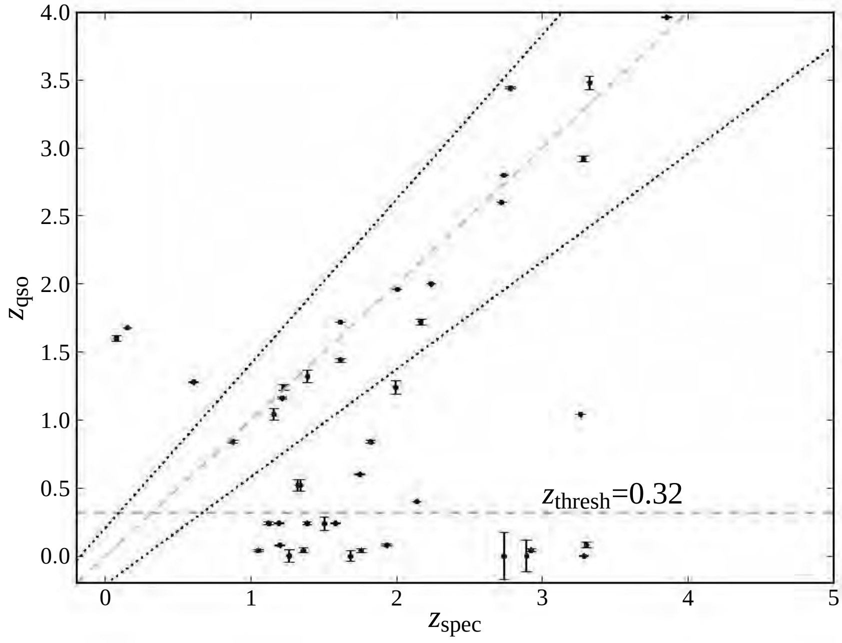

Figure 4.11: Top: Photometric redshifts for quasars estimated from galaxy templates versus spectroscopic redshift including error bars σ estimated from the χ^2 fitting procedure as in equation 4.4. Bottom: Photometric redshifts for quasars estimated from quasar templates versus spectroscopic redshift including error bars σ estimated from the χ^2 fitting procedure as in equation 4.4

4.4.4 *Photometric redshifts of VLA radio sources*

The cross-matched sample of VLA radio sources consists of 911 single component radio sources with 2 arcsec aperture magnitudes in the $K_{\rm s}$ band <23. The least squares fit in the photometric redshift algorithm failed converge for three of these objects with very faint photometry, leaving 908 single component sources and 10 multiples identified in section 4.3. Quasars in the VLA sample were identified based on the SEXTRACTOR CLASS_STAR parameter which provides a measure of how well resolved an object is in the infrared image. The neural network based method used to estimate this parameter in SEXTRACTOR is known to break down for the faintest objects. In order to determine whether this parameter is still reliable at the chosen magnitude limit I show the CLASS_STAR estimates versus $K_{\rm s}$ magnitude in figure 4.12. The break down in the classification process can be identified by the merging of the two initially distinct populations at CLASS_ STAR either 1 or 0 into a single indistinguishable mass with CLASS_STAR values ∼0.5. Based on figure 4.12 the CLASS_STAR estimates should still permit a reasonably secure means of identifying unresolved sources below the $K_{\rm s} < 23.0$ limit. A criteria of CLASS_STAR >0.8 identified 78 quasars in the VLA survey, eight of these have photometric redshifts of <0.2 and were excluded from the sample based on the observation in section 4.4.2.2 that quasars with redshift estimates below this threshold are likely to be extremely unreliable.

In figure 4.13 I present the photometric redshift distributions of the quasars and the full population of cross-matched radio sources. The redshift distribution of the whole sample is compared to that predicted by the SKADS simulations for a 1 square degree field with a variable flux density limit corresponding to that presented for the VLA radio catalogue in section 4.2. A notable feature of both these plots is the slight peak in the distributions at a redshift of ∼1. To investigate whether this peak is likely to be a real feature indicative of some large scale structure in the observed field or an artefact of the photometric redshift procedure I plotted the photometric and spectroscopic redshift distributions of the whole catalogue of $K_{\rm s}$ detected objects in the VIDEO field. I present these distributions for the sample limited at $K_{\rm s}$ magnitudes < 22.0 and 23.0 in figure 4.14. In these figures there appears to be a peak at redshift *sim* 0.9 in both the spectroscopic and photometric redshifts and this peak is still visible when the sample is limited at brighter magnitudes. Ilbert et al. (2006) produced a

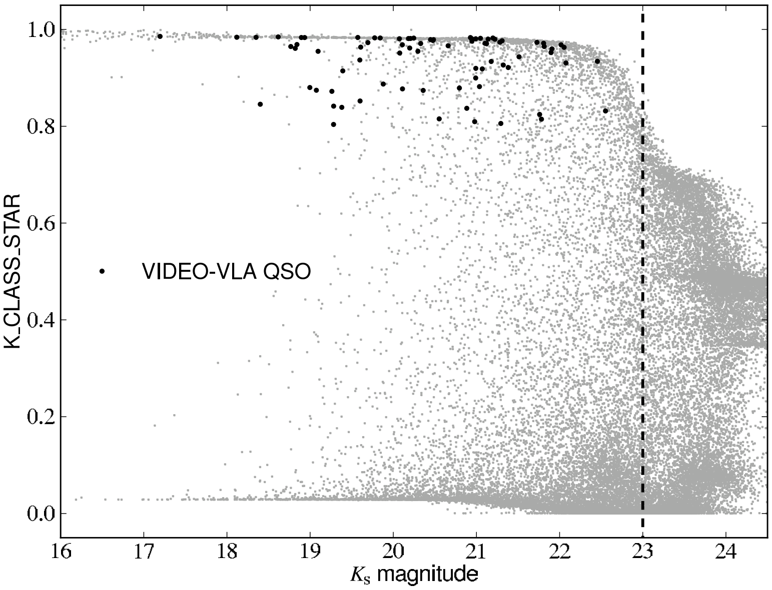

Figure 4.12: SEXTRACTOR CLASS_STAR parameters versus K_s magnitude. The dashed line corresponds to the K_s <23.0 magnitude limit. Black dots indicate radio sources identified as quasars based on their CLASS_STAR estimates.

photometric redshift catalogue over this field using CFHTLS-D1 and VVDS photometry in $u*$,g',r',i',z', $BVRI$ J and K_s bands and report that a peak at redshift ~0.9 is also discernible in their photometric redshift distribution.

The most likely mechanism by which a failure in the photometric redshift procedure could produce an over prediction of sources at a particular redshift bin arises due to systematic offsets in the photometry of two neighbouring filters. In this scenario the template fitting procedure identifies this small offset with either the Lyman or Balmer break features in the template SED's and systematically places the objects at redshifts where these features fall approximately between the two slightly offset filters. At brighter magnitudes the improved photometry and larger total flux measurements will minimise the contribution of such small systematic errors, and any redshift artefacts should disappear. The persistence of the peak in the redshift distribution when limited at brighter magnitudes thus tends to rule out this scenario. Figure 4.5 showed no evidence of a larger number of failures or a greater variance in the $z_{spec} - z_{phot}$ relation at a redshift of 1 and the peak is also marginally discernible in the spectroscopic redshift distributions which are clearly independent of errors produced by the photometric redshift method. These three considerations suggest that the observed peak is a real feature of the radio source distribution in this field.

When comparing to the distribution produced by the SKADS simulations it is clear that the number of sources in the lowest redshift bin is much lower than the predicted values. Simpson et al. (2012) also noted a similar deficit of low redshift sources compared with SKADS predictions in their radio survey of the *Suburu/XMM-Newton* Deep field, and attributed this to the effects of resolution bias. Resolution bias refers to the number of faint resolved sources missing from a peak flux density limited survey because their extended emission is not detected by the radio interferometer. Bondi et al. (2003) performed detailed simulations to determine the effect of this bias on their VLA catalogue and their estimates place the number of undetected sources due to this effect at ∼141. This number of resolved low redshift sources would bring the total count in figure 4.13 well in excess of the SKADS predictions. However the correction for resolution bias depends on the assumed angular size distribution of sources in the field and is obviously subject to some uncertainty. Furthermore at redshift ≤ 0.5 the cosmic volume probed by a 1 degree^2 survey is very small ($\sim 7\mathrm{e}^5$ Mpc^3) and there are likely to be large field to field variations in the number of detected low redshift sources. To investigate this question I determined the redshift distributions of 100 1 degree^2 fields in the SKADS simulations and plot the variation in low redshift source counts between these 100 fields in figure 4.15. This process implies that an estimate of ∼141 undetected sources would be consistent with the very upper end of the SKADS predictions for low redshift sources in a square degree field. The resolution bias effect is not corrected for in the final determination of the luminosity function but figure 4.13 suggests that it is only significant at the low redshift bins where the small volume ($\sim 7e^5$ Mpc^3) probed by the survey and low number of sources already dictate a high degree of uncertainty.

Finally figure 4.16 presents the photometric redshift errors estimated from the χ^2 distributions of the fitting procedures. This figure demonstrates that, as expected, the uncertainty in the fitting procedure increases at higher redshifts where the errors on the photometry are greater.

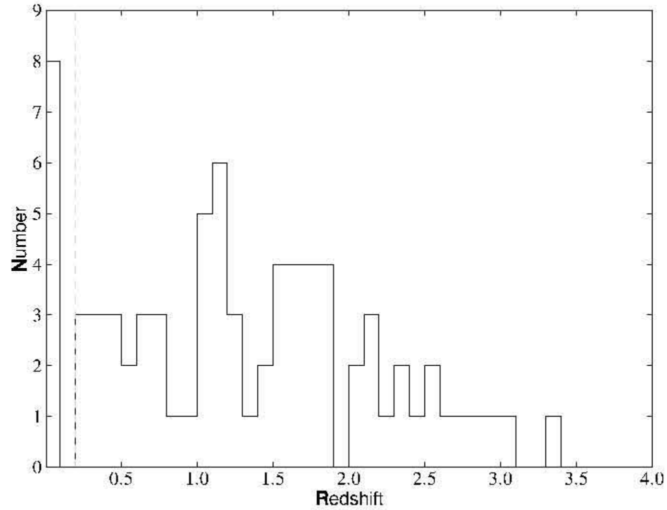

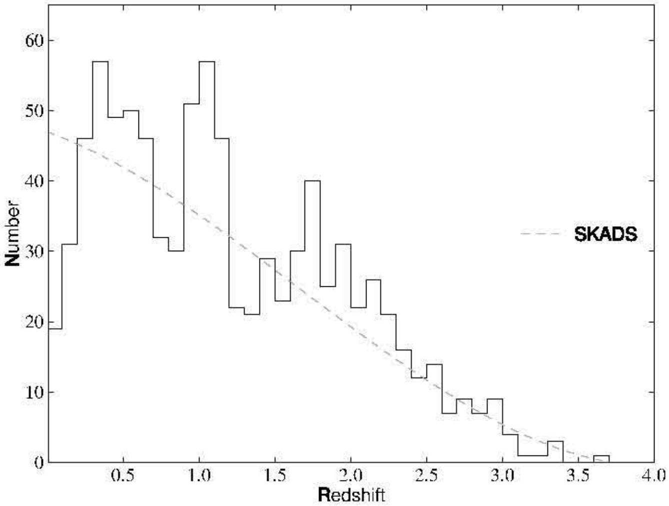

Figure 4.13: Top: Photometric redshift distribution of quasars in the VLA-VIDEO field. These were identified by the criteria CLASS_STAR>0.8, the dashed line represents the threshold z_{phot} <0.2 used to reject quasars with unreliable redshift estimates. Bottom: Redshift distribution of all cross-matched radio sources. The dashed line represents the photometric redshift distribution of radio sources in 1 square degree field complete to 100 μJy is the SKADS simulations.

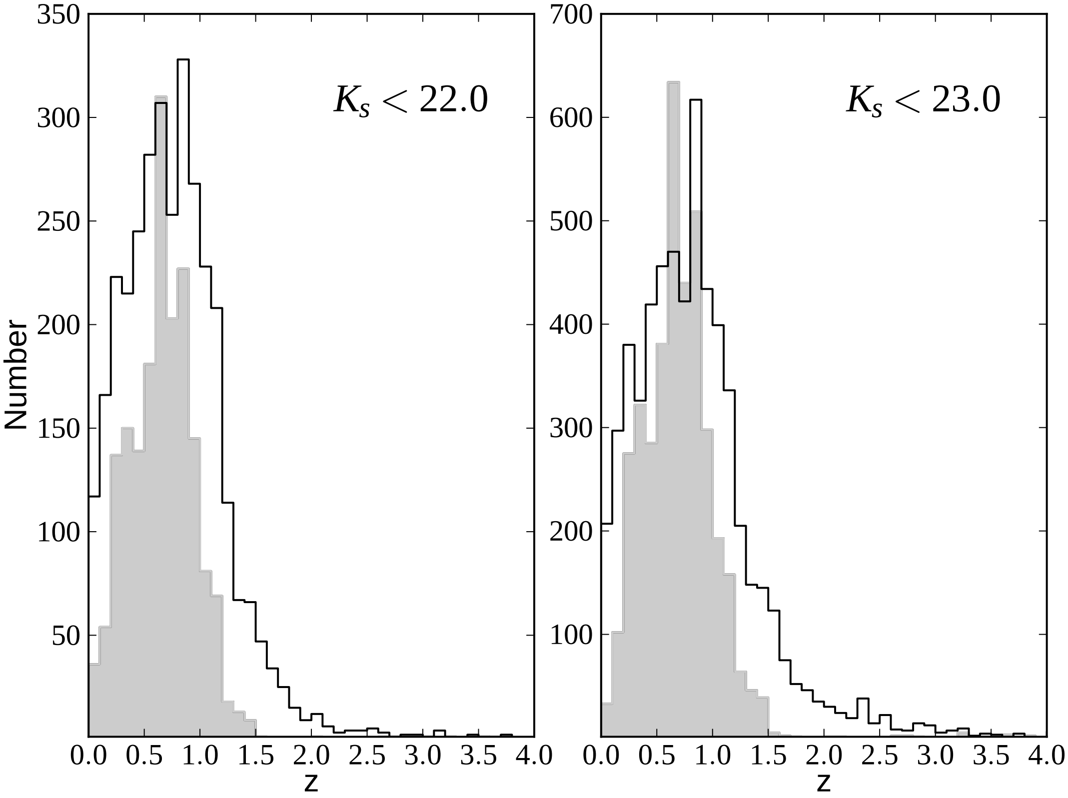

Figure 4.14: Photometric and spectroscopic redshift distributions for all K_s detected objects in the VIDEO survey limited to $K_\mathrm{s} < 22.0$ and 23.0. The shaded histograms are for objects with spectroscopic redshifts in the VVDS.

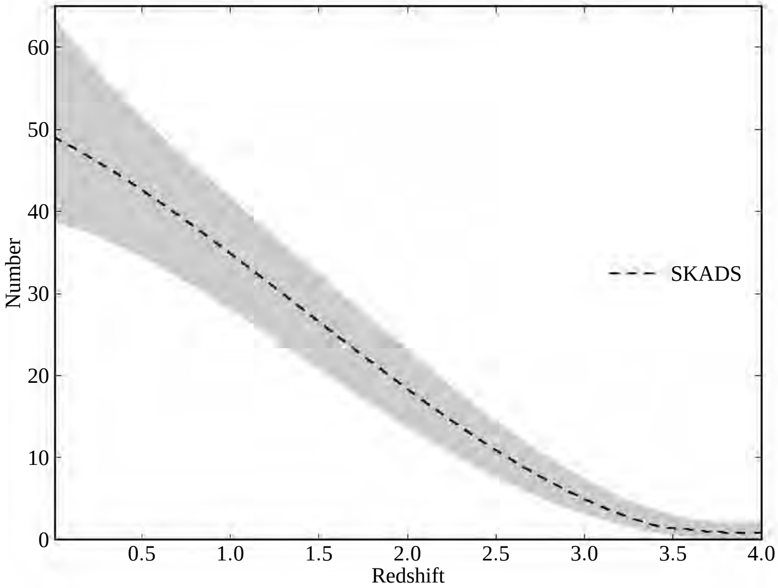

Figure 4.15: The 5σ variation in redshift distribution between 1 degree^2 fields in the SKADS simulations. The dotted line corresponds to the SKADS field plotted in figure 4.13 for purposes of comparison. The y-axis gives the number of radio sources per redshift bin, with redshift bin widths of 0.1.

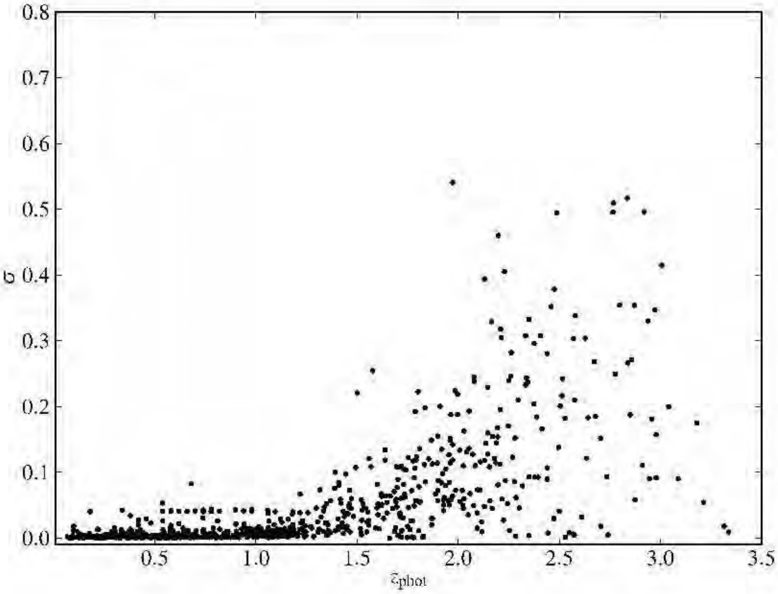

Figure 4.16: The errors in photometric redshift for radio sources in the combined VIDEO-CFHTLS survey field.

4.5 *The radio luminosity function*

The radio luminosity function for the VIDEO-VLA survey was constructed using the same binned $\sum \frac{1}{V_{\max}}$ method employed in chapter 2. Radio luminosities and maximum observable redshifts were once again calculated using the standard spectral index based k-correction factor and the luminosity distance relationship presented in equations 2.8 and 2.9 in chapter 2. The calculated luminosities and redshifts for this sample are presented in figure 4.17.

As was the case in chapter 2, the final $V_{\max}$ estimate used in the RLF must account for the cases where the NIR $\mathrm{K_s}$ magnitude limits, rather than the radio survey limits, determine the maximum observable distance of a source in the cross-matched sample. This is an especially relevant consideration, as figure 3.9 in the cross-matching chapter demonstrated that a large number of the radio counterparts are faint in the NIR. To determine the NIR limited $\mathrm{z_{max}}$ I assumed that the true NIR source SED's were well represented by the best-fitting template SED's determined by Le Phare during the photometric redshift estimation procedure. These templates are scaled to the observed photometry by a scaling factor A determined in the fitting procedure (see equation 4.1). I determined the predicted observed fluxes at any given redshift in the VIDEO K_{s} filter by redshifting the scaled SED template and multiplying with the VISTA $\mathrm{K_s}$ band instrumental response to determine $A \times F_{pred}^{K_s}(z, \mathrm{T_{best}}, \mathrm{E(B-V)_{best}})$. Redshifting the

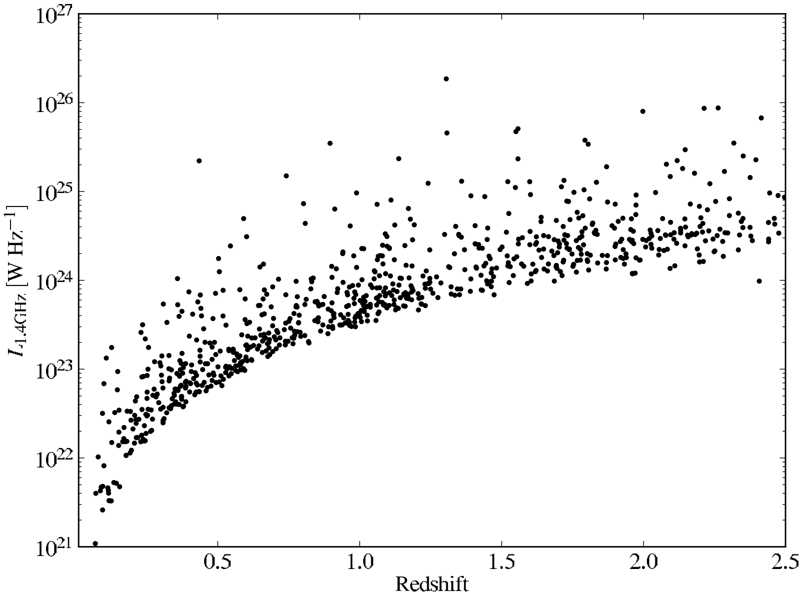

Figure 4.17: Radio luminosity versus redshift for radio sources in the combined VIDEO-CFHTLS survey field.

templates was achieved by :

- Converting emitted wavelength λ_e to observed wavelength λ_o by multiplying by 1+z.
- Correcting for cosmological dimming using the relationship between observed flux F, intrinsic luminosity L and luminosity distance D_L as $F = \frac{L}{4\pi D_L}$.
- Correcting the template flux densities F_λ to account for redshift stretching of the $\Delta\lambda$ interval by dividing F_λ by 1+z.

In all cases I used the best fitting template and, where appropriate, dust-extinction reddening excess corresponding to the predicted photometric redshift produced by LE PHARE. The final $\mathrm{z}_{\mathrm{max}}^{\mathrm{NIR}}$ parameter is then found as the minimum redshift for which

$$A \times F^{f}_{\nu\, pred}(z, \mathrm{T}_{\mathrm{best}}, \mathrm{E(B-V)}_{\mathrm{best}}) \leq 10^{-0.4(\mathrm{K}_{\mathrm{lim}}+48.6)} \tag{4.5}$$

where $\mathrm{K}_{\mathrm{lim}}$ is the limiting magnitude of K_{s} <23.0. As a consistency check on the synthetic photometry code used to estimate $z_{\mathrm{max}}^{\mathrm{NIR}}$ I compared the χ^2 and scaling factor A values produced by my redshifting code to those determined by LE PHARE and found these to be in good agreement.

Figure 4.18 presents the RLF of the VLA-VIDEO survey in six redshift bins in the interval z∼0.05–2.5. The error bars in these plots consider only errors due to the sample size per bin with no contribution due to the errors in the photometric redshifts. The RLF in this work is compared to the local RLF determined in Mauch and Sadler (2007) using NVSS radio sources with spectroscopic redshifts in the 6 degree Field Galaxy Redshift Survey (6dFGRS; Jones et al., 2004). The Mauch and Sadler (2007) luminosity function is constructed from separate fits to the luminosity functions of star-forming and AGN radio galaxies and the individual contributions of these two populations are plotted as dotted and dashed lines in figure 4.18 respectively. It clear from the plot that the local radio luminosity function is dominated by star-forming and AGN contributions at low and high luminosities respectively, with the division falling at roughly $\sim 10^{23}$W Hz^{-1}. The VLA-VIDEO local RLF determined in this work appears to be in reasonably good agreement with the Mauch and Sadler (2007) star-forming galaxy luminosity function at low luminosities. The absence of higher luminosity

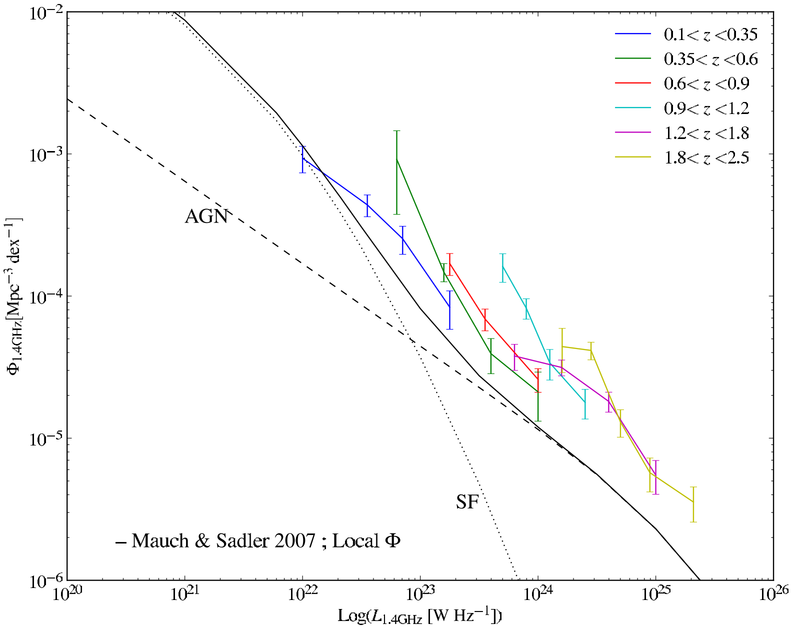

Figure 4.18: Radio Luminosity Function in 6 redshift bins for the VIDEO-CFHTLS field. The solid line represents the local radio luminosity function determined by Mauch and Sadler (2007) with the individual contributions of star-forming and AGN radio sources plotted as dashed and dotted lines respectively.

radio sources in the lowest redshift bin precludes me from making a direct comparison with the local AGN luminosity function, however at higher redshifts the VIDEO RLF would seem to be reasonably consistent with a basic prescription of pure density or pure luminosity evolution of their local AGN LF. Whilst far from conclusive this provides some measure of reassurance that the Mauch and Sadler (2007) local LF is an appropriate representation of radio galaxies in the VIDEO field and can be used as a local benchmark against which to search for evidence of evolution.

Figure 4.18 appears consistent with a fairly rapid increase in the space density of radio galaxies up to a maximum at redshifts of $z \sim 1.2$, with hints of either a slowing down of this process or even negative evolution of the source densities between redshifts $z = 1.2 - 2.5$. To quantify these broad evolutionary trends I used models of pure density evolution and pure luminosity evolution of the combined star-forming and AGN RLF, such that:

$$\begin{aligned}\Phi(z) &= (1+z)^{\alpha_d}(\Phi_{\mathrm{SF}} + \Phi_{\mathrm{AGN}}) \\ \Phi(z) &= \Phi_{\mathrm{SF}}\left(\frac{L}{(1+z)^{\alpha_l}}\right) + \Phi_{\mathrm{AGN}}\left(\frac{L}{(1+z)^{\alpha_l}}\right) \qquad (4.6)\end{aligned}$$

where $\Phi_{\rm SF}$ and $\Phi_{\rm AGN}$ are the star-forming and AGN luminosity functions of Mauch and Sadler (2007) respectively. Such models are clearly limited in their ability to accurately represent the behaviour of the three sub-classes of potentially independently evolving radio sources present in the sub-mJy VLA-VIDEO sample.

The parametrization simply provides a convenient means to quantify the overall strength and sense of the evolution taking place at different cosmic times. Based on the tentative evidence in figure 4.18 that the evolutionary behaviour of these sources changes at a redshift of ~ 1.2, I fitted three possible evolutionary scenarios to the data, the first is of pure density evolution with a single α_d parameter for the entire redshift range from z$\sim$0–2.5. The second is of pure density evolution out to a redshift of z=1.2 and no further evolution taking place beyond this, and the third fits independent pure density evolution parameters α_{d1} and α_{d2} in the redshift z$\sim$0–1.2 and 1.2–2.5 ranges. I repeated the fitting procedure for these three scenarios assuming pure luminosity evolution. The evolution parameters and χ^2 values produced by these fits are presented in tables 4.2 and 4.3, and figures 4.19, 4.20 and 4.21 present a comparison of the data points to the evolved luminosity function produced by the three models assuming pure density evolution. In all three cases the data implies an increasing source density out to z$\sim$1, with density enhancements at this redshift by a factor of $\sim$2.5–4 over the local values. The independent α_{d2} determined in model 3 implies a decrease in space density towards earlier cosmic times but is also consistent with the scenario of no evolution beyond z$\sim$1.2. Whereas an assumed constant positive evolution across the entire redshift range in model 1 clearly provides the worst fit to the data. Recalling the marked peak in objects at z$\sim$1 in the photometric redshift distribution of the VIDEO-VLA sources and the potential this has to enhance the inferred evolution out to z$\sim$1 as well as to create the observed negative evolution in the post z= 1 interval I excluded the points in the $0.9 \lesssim z \lesssim 1.2$ bin, refitted these same three models and found the results of the fitting procedure to be nearly identical. However if a large cluster of sources exists in the $0.9 \lesssim z \lesssim 1.\ 2$ and some reasonable fraction of these are scattered into the neighbouring redshift bins by photometric redshift errors this redshift peak may still bias the results of the fit even when explicitly excluding the z$\sim$1 bin.

The reduced χ^2 values in tables 4.2 and 4.3 indicate that all three pure density and pure luminosity evolution scenarios are formally poor fits to the data. A possible explanation for this

Table 4.2: Results of fitting three different evolutionary scenarios to the RLF in six redshift bins. Pure density evolution is assumed in all three cases.

	z=0–1.2	z=1.2–2.5		
	α_{d1}	α_{d2}	χ^2	reduced χ^2
model 1	1.25±0.10		69	3.63
model 2	1.60±0.11	0±0	52	2.74
model 3	1.77±0.18	-0.19±0.17	48	2.67

Table 4.3: Results of fitting three different evolutionary scenarios to the RLF in six redshift bins. Pure luminosity evolution is assumed in all three cases.

	z=0–1.2	z=1.2–2.5		
	α_{l1}	α_{l2}	χ^2	reduced χ^2
model 1	1.68±0.13		67	3.52
model 2	2.07±0.13	0±0	51	2.68
model 3	2.24±0.18	-0.23±0.20	48	2.67

is that the assumed functional forms of pure density evolution or pure luminosity evolution are not adequate representations of the evolution taking place in the faint radio source population, luminosity dependent density evolution may provide a better fit to the evolution of the RLF.

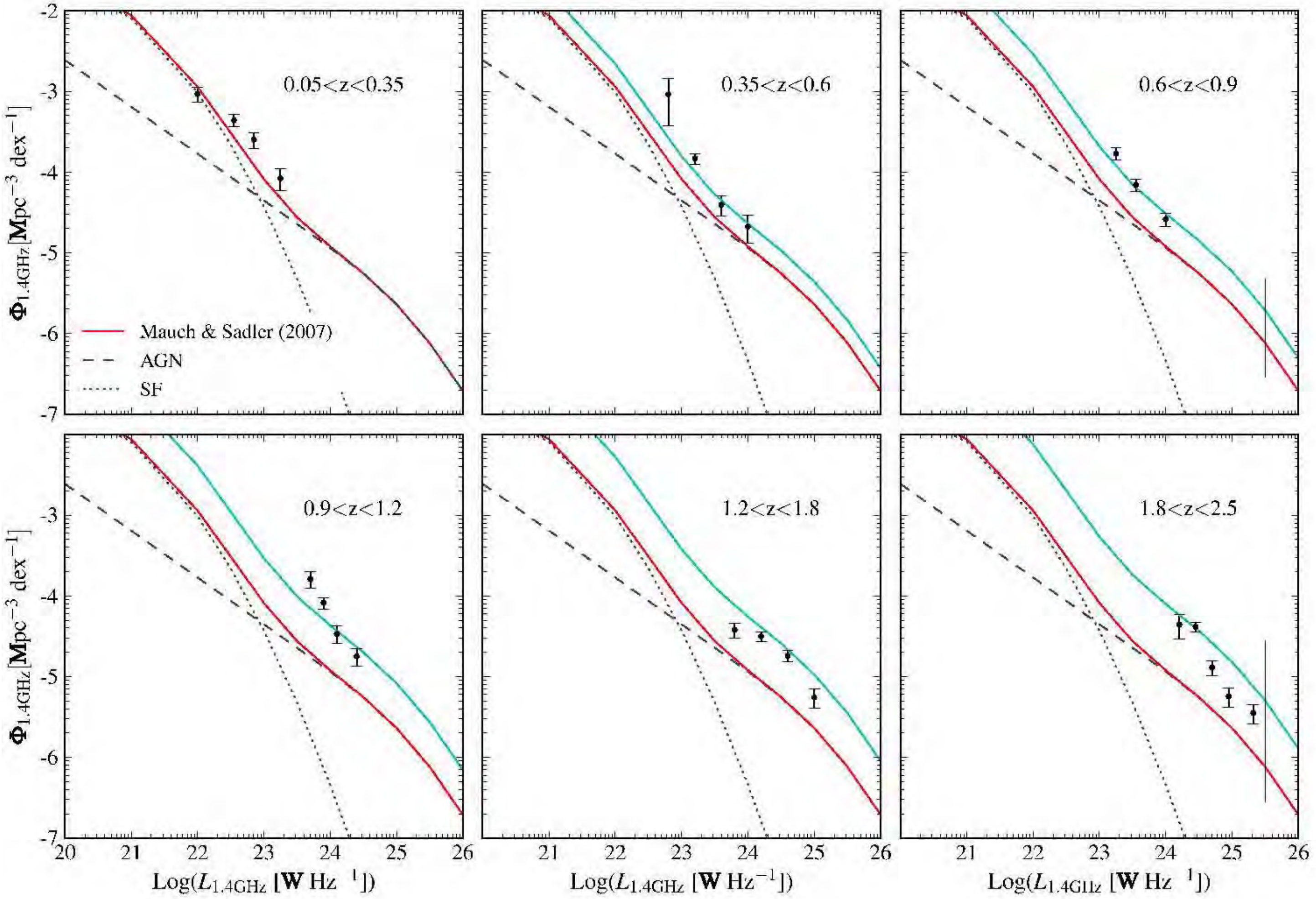

Figure 4.19: The radio luminosity function fitted by pure density evolution of the local AGN and star-forming luminosity functions. The blue curve represents the evolved local luminosity function corresponding to model 1 in table 4.2 with positive PDE out to $z \sim 2.5$ with α_d=1.25

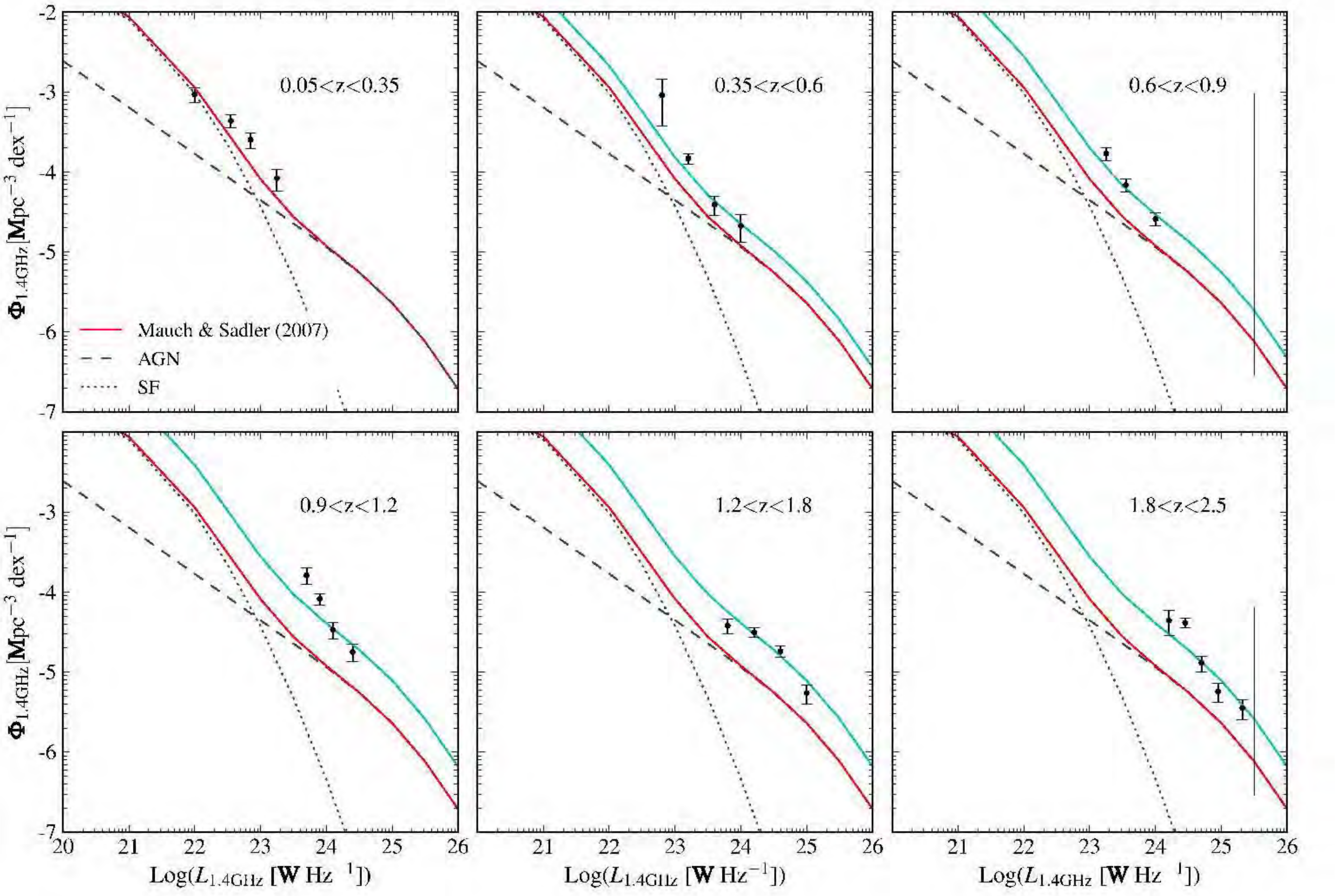

Figure 4.20: The radio luminosity function fitted by pure density evolution of the local AGN and star-forming luminosity functions. The blue curve represents the evolved local luminosity function corresponding to model 2 in table 4.2 with positive PDE out to $z \sim 1.2$ with α_d=1.6 and zero evolution thereafter.

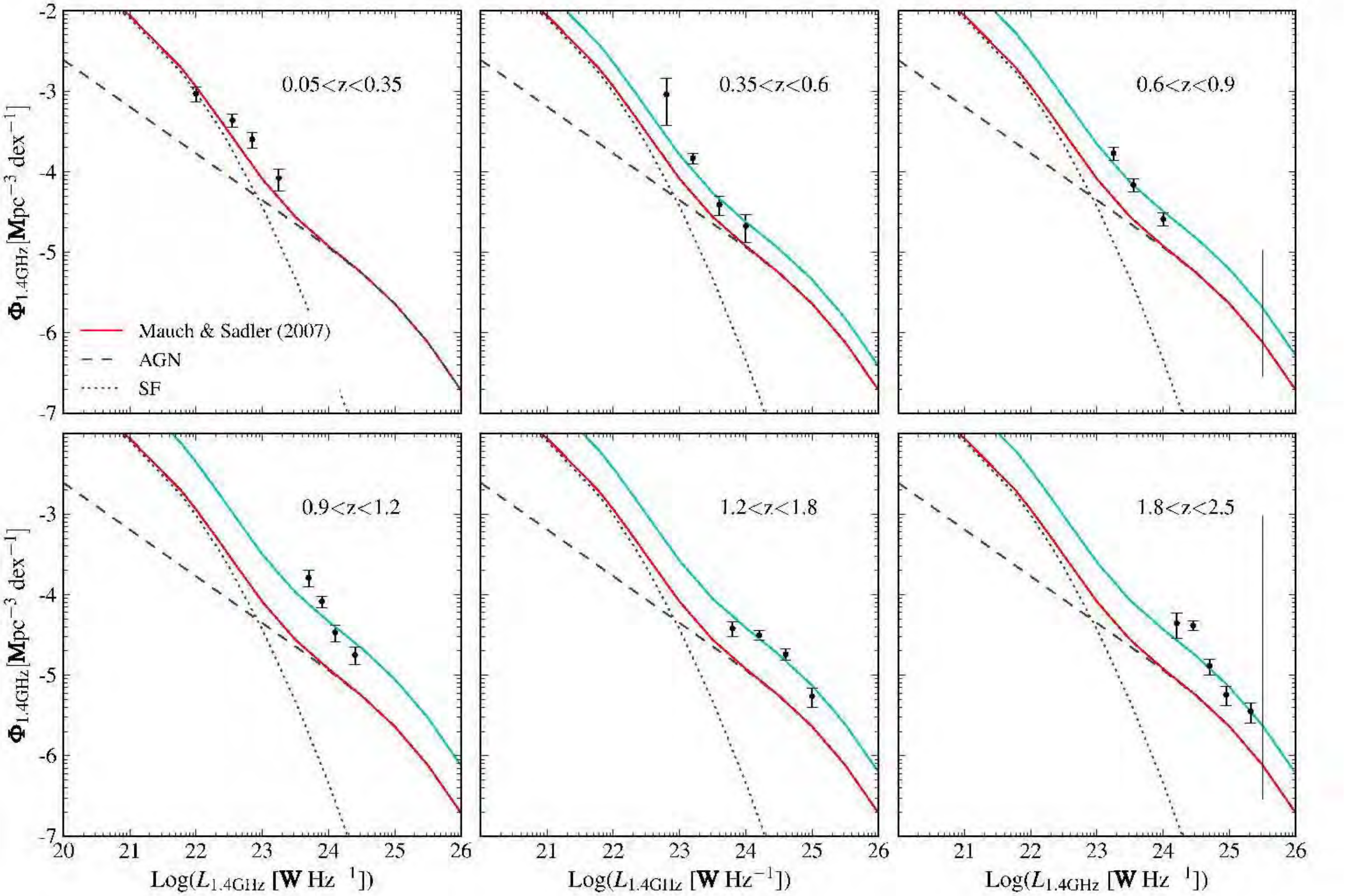

Figure 4.21: The radio luminosity function fitted by pure density evolution of the local AGN and star-forming luminosity functions. The blue curve represents the evolved local luminosity function corresponding to model 3 in table 4.2 with positive PDE out to z ∼1.2 with α_{d1}=1.77 and negative evolution with α_{d2}=-0.19 in the interval $z = 1.2 - -2.5$

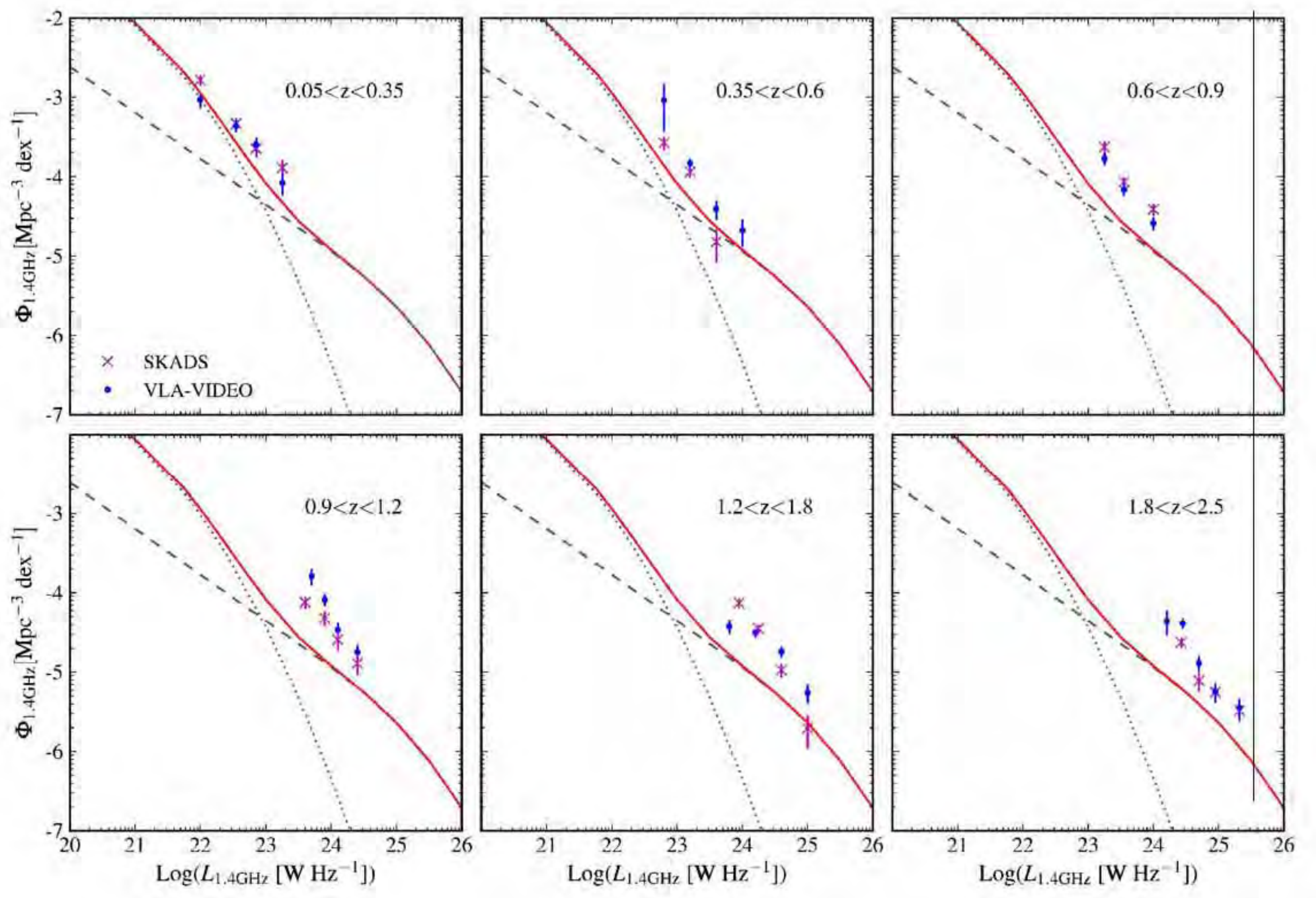

Figure 4.22: Comparison of the VLA-VIDEO RLF with a RLF derived from a square degree field in the SKADS simulation. The dashed red curve represents the local luminosity function of (Mauch and Sadler, 2007) with the individual contributions of star-forming galaxies and AGN represented as dashed and dotted lines respectively.

Recent results from Simpson et al. (2012) identified tentative evidence of a decline in the RLF of radio sources at redshifts $\gtrsim 1.5$ in the luminosity range $10^{24-25.5}$ W Hz^{-1} (see their figure 11), which would be consistent with the trend observed in the VIDEO-VLA dataset. Rigby et al. (2011) also identify a luminosity dependent turnover in the luminosity function, with lower luminosity objects experiencing a decline in their number densities at lower redshifts than their high luminosity counterparts. Their results imply a turnover at z$\gtrsim$ 0.7 for objects with luminosities in the 10^{25-26} W Hz^{-1} range, which is at a slightly lower redshift than seen in the VIDEO-VLA RLF. The points in figures 4.18 do not betray any hint of such a luminosity dependent effect, but clearly the narrow luminosity range probed in each redshift bin hampers any attempt to confirm this. When interpreting the results suggested by the luminosity function towards the higher redshifts it is important to recollect figure 4.16 which illustrated the large increase in photometric redshift uncertainty towards higher redshift bins. These errors are not included in the error bars in the plots in figure 4.18 or in the χ^2 fits of the 3 simplistic models of evolution and including these photometric redshift uncertainties is an important consideration when determining the robustness of this suggested high redshift decline. However, as noted earlier, the trend is for photometric redshift errors to preferentially scatter low redshift objects up to higher redshifts making it unlikely that these more typical systematic errors are responsible for the observed decline, although this clearly doesn't rule out all possible sources of error in the redshift estimates. A further possible explanation for this observed decline is that the low redshift bins primarily probe luminosities dominated by star-forming galaxies and whereas the higher redshift bins are appear to be primarily sensitive to the AGN populations and this observed decline may be the result of relatively slower evolution by the AGN populations compared to the star-forming galaxies in the z$\lesssim$1.2 interval.

Figure 4.22 compares the RLF derived from the VLA-VIDEO survey with a RLF determined using the SKADS simulations. The luminosity function was determined over a 1 degree^2 field with a flux density limit of $\sim$100 μJy. The VLA-VIDEO results seem in reasonable agreement with the SKADS simulations.

To determine whether excluding the $\sim$116 radio sources without reliably identified counterparts in the VIDEO survey is likely to significantly alter the RLF calculated in this chapter I used the monte-carlo technique of chapter 2. Using the K-z relation I determined that the mean

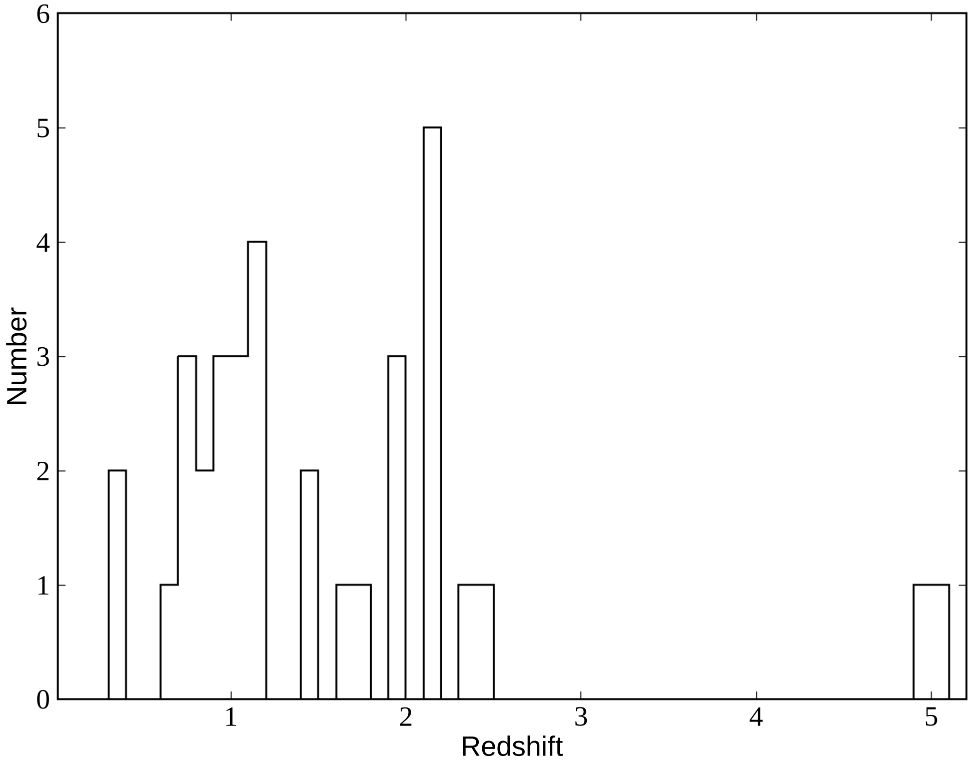

Figure 4.23: Redshift distribution of all counterparts with high likelihood ratios (LR>1) and low reliabilities (Rel<0.8).

redshift of sources fainter than $K_s = 23.5$ is ∼4.0. Thus it is reasonable to assume that a large fraction of the sources without counterparts have redshifts higher than 2.5, which is the limit of the study presented here. In chapter 3 there were a small number of sources (∼17) whose counterparts have LR> 1 but low reliabilities (<0.8). These are sources whose counterparts are brighter than $K_s = 23.5$ that are not reliably identified due to the presence of two highly likely counterparts within the search radius. The photometric redshift distribution of all the possible counterparts to these 17 sources is presented in figure 4.23, which demonstrates that these counterparts are clustered at redshifts of ∼1 and 2. As there are only a small number of such sources they should only have a small impact on the RLF, but the redshift distribution of figure 4.23 would suggest that their inclusion would strengthen the evolution out to z∼1 and slightly increase the RLF at z∼2–2.5.

4.6 *Conclusions*

This chapter has presented a determination of the RLF for the VLA-VIDEO survey field using reliably identified sources with ∼9 band photometric redshifts $\lesssim$2.5. The luminosity function broadly implies an increase in the space densities of low luminosity radio sources by a factor of ∼2.4–4 in the $z = 0 \sim 1.2$ range and no evolution or possibly negative evolution thereafter.

Interpreting and comparing these results to previous studies is complicated as the radio population at these lower flux densities contains contributions from radio-loud and radio-quiet AGN as well as star-forming galaxies, and these populations may all evolve independently. Previous investigations by Clewley and Jarvis (2004); Sadler et al. (2007); Donoso et al. (2009) of large samples of bright NVSS and FIRST radio samples, with flux limits of a few mJy, imply that the low luminosity population ($\lesssim 10^{25}$W Hz^{-1}) increases by a factor of ∼2 in the z=0–0.55 range. These studies also found evidence that the strength of the evolution taking place increases towards higher luminosities. Further support of a luminosity dependent behaviour was presented in Rigby et al. (2007) who found slightly stronger positive evolution for a smaller,fainter sample of FRI objects to redshift ∼1. Their results imply density enhancements of ∼5–9 for sources brighter than the 10^{25}W Hz^{-1} threshold. As this work used morphologically identified FRI candidates their sample is free from contamination from star-forming galaxies and these three studies should be primarily sensitive to evolution taking place in radio-loud AGN.

There have also been several characterisations of the evolution of radio sources using very deep surveys over smaller fields, these utilise a variety of criteria to separate contributions from the different underlying populations present at fainter flux densities. Their results are thus affected by uncertainties in the completeness and contamination produced by the specific classification method employed in each case and the use of different classification methods on a per study basis also complicates attempts to make direct comparisons between them. A summary of the results of these deeper narrower studies, which probe the luminosity function over a similar redshift range as the VIDEO study in this thesis, is presented in table 4.4. These works include the Smolčić et al. (2009a,b) studies of the COSMOS field which use a colour based separation criteria developed from the BPT diagram to identify AGN and star-forming galaxies. Their results found pure luminosity evolution with $L^* \propto (1+z)^{0.8}$ for AGN and slightly stronger

Table 4.4: Comparison of current determination of the evolution of the Radio Luminosity Function out to a redshift of ~1.3. Numbers quoted are the α_L parameters determined by fitting pure luminosity evolution.

Reference	Field	AGN		Star-forming		All
		R-Quiet	R-Loud	Strong	Intermediate	
Strazzullo et al. (2010)	SWIRE	2.7±0.3		$3.2^{+0.4}_{-0.2}$	$3.7^{+0.3}_{-0.4}$	3.5±0.2
Smolčić et al. (2009a,b)	COSMOS	0.8±0.1		2.1±0.2		
Padovani et al. (2011)	*Chandra* DFS	$3.8^{+0.7}_{-0.9}$	—	$3.1^{+0.8}_{-1.0}$		
Simpson et al. (2012)	SXDF	+ve	None [a]			+ve

[a] $L_{1.4GHz} \leq 10^{24}$ W Hz^{-1}

evolution in star-forming galaxies with α_L ~2.1, with no separate classification for radio-quiet AGN.

In the SWIRE field Strazzullo et al. (2010) employed a method based on SED template fitting to separate their very faint sample ($5\sigma \sim 14\mu$Jy) into strongly and intermediately star-forming galaxies and AGN and found similar pure luminosity evolution parameters of α_L ~3.0 for all three of these populations. This is slightly higher for the AGN population than implied by the results of Sadler et al. (2007) and Smolčić et al. (2009b), but quite consistent with previous estimates of the evolution taking place in radio-selected star-forming populations. The results of Smolčić et al. (2009b) and Strazzullo et al. (2010) hold for $z < 1.2$. Padovani et al. (2011) identified pure luminosity evolution at levels comparable to the Strazzullo et al. (2010) results taking place in both their star-forming and radio-quiet quasar samples. However they find evidence that the low luminosity radio-loud AGN population undergoes no evolution in the redshift range probed by the Smolčić et al. (2009b) study and suggested the evolution detected for low-luminosity AGN in the COSMOS study is driven by radio-quiet AGN included by their selection criteria.

Simpson et al. (2012) also see evidence of density enhancements of low luminosity sources at up to a redshift ~ 1, and they identify this as being predominantly driven by evolution of the radio-quiet objects. Radio quiet objects in their sample are identified based the ratio of mid-infrared (24 μm) to radio flux and this definition encompasses both star-forming and radio-quiet AGN. Whereas they see no evidence of evolution for low-luminosity radio-loud AGN. While it is not clear which sub-population is primarily driving the observed positive evolution the result determined in this work of density enhancements out to $z \sim 1.2$ is thus broadly consistent with a number of previous investigations. However it implies a stronger evolution of the Sadler et al. (2007) AGN RLF function, dominant above 10^{23}W Hz^{-1} in the local universe, than obtained in chapter 2 of this thesis and in Smolčić et al. (2009b).

Beyond the $z\sim$1.2 threshold there have been some suggestions of a cutoff in the RLF in the works of Rigby et al. (2007, 2011) and Waddington et al. (2001). The LF of Simpson et al. (2012) also implies systematically lower space densities for objects at redshifts >1.5 whilst Padovani et al. (2011) claim evidence of strong negative evolution in the more powerful radio-loud populations which they suggest might be the result of a high redshift cutoff in these source populations. Thus the decline observed at $z > 1.2$ in the VIDEO RLF may be tentatively supported by evidence in the literature, however the caveat of much larger photometric redshift errors applies at these higher redshifts and I hope to incorporate these errors via Monte Carlo simulations in future work. Disentangling the contributions of the various low-luminosity radio populations is clearly a difficult proposition and has important implications for our ability to deduce their evolutionary behaviour and make inferences about links between AGN and star-forming processes. The discussion above which presents the myriad of evolutionary scenarios currently postulated ranging from luminosity dependent evolution, to the possibility of very significant high redshift contributions from rapidly evolving radio-quiet quasar populations serves to illustrate how much uncertainty remains in this area and the vitally important role of multi-wavelength datasets in constraining these increasingly complex scenarios.

More complicated modelling of the evolution of radio sources could be carried out by combining a range of deep fields,e.g. COSMOS (Smolčić et al., 2009a,b), *Suburu/XMM Newton* Deep field (Simpson et al., 2012) and the VLA-VIDEO field in this work. This combined dataset would provide enough objects to pin down the evolution beyond z$\sim$1, furthermore combining surveys with different flux limits provides much better coverage of the luminosity-redshift plane.

Chapter 5

Properties of faint radio sources

The potential that large radio surveys have to probe the relationship between accretion activity and star-formation throughout the history of the universe is dependent on multiwavelength datasets. These are crucial in that they provide both a means to classify the intrinsically mixed population of objects at low radio flux densities and to obtain estimates of relevant properties of the host galaxies including their mass, accretion rate and mode as well as their star-formation histories. As multi-band studies of faint radio sources are still in their infancy there is some uncertainty as to the most effective strategy to separate these populations and how different methods used to identify and characterise sub-classes of radio objects compare.

This chapter thus presents a brief investigation into the possibility of using multi-band SED fitting techniques to separate the faint radio population into its AGN and star-forming constituents and to study the properties of their host galaxies. Optically selected galaxies in the local universe are known to exhibit a strongly bimodal distribution in their colour-magnitude diagram and these separate populations are commonly referred to as the 'blue cloud' and 'red sequence'. As galaxy colours are representative of the underlying dominant stellar populations in the galaxy this bimodality represents a separation between galaxies which are still actively star-forming with blue optical and UV colours and those in which star-formation has largely ceased with redder colours. Morphologically red sequence galaxies are predominantly early-type galaxies with Ell, S0 or Sa classifications while blue cloud galaxies are spiral Sb, Sc and later morphological types (Strateva et al., 2001; Bell et al., 2004a,b; Baldry et al., 2004). Thus galaxy colours and morphological types can potentially be used as rough indicators of star-formation history.

Radio-loud AGN in the local universe are known to be preferentially hosted in massive red elliptical galaxies. However there is growing evidence that the HERG quasar mode accretors are preferentially associated with bluer colours and evidence of ongoing star-formation in contrast to their low-luminosity LERG counterparts which are primarily located in 'dead and red' ellipticals (Baldi and Capetti, 2008; Herbert et al., 2010; Smolčić and Riechers, 2011; Best and Heckman, 2012). The small survey area and faint flux limits of the VLA radio survey in this work dictates that the radio sample will primarily consist of low-luminosity AGN and star-forming galaxies with only a very small contribution from powerful HERG/FRII-type sources. As the dominant AGN population in this sample is thus expected to be associated with passively evolving elliptical galaxies and star-forming radio sources will primarily be associated with blue spiral host galaxies I used the classification of fitted template SEDs to classify the radio sources as AGN or star-forming. Such an approach is very similar to using a colour-magnitude diagram relationship for classification but has the advantage of utilising information in all the available photometric bands to obtain the most accurate characterisation of the underlying source SED and the best possible constraints on dust-extinction parameters. Without far-infrared observations to independently constrain the total dust content of a galaxy it is very difficult to distinguish between objects that are intrinsically red and dust-reddened star-forming galaxies. Arnouts et al. (2007) demonstrated that full SED template fitting can correctly identify a greater fraction of these dust-reddened star-forming galaxies compared to a straightforward colour magnitude cut, although at high redshifts ($\geq$1.5) the quiescent/red sample identified by this method may still contain a significant fraction ($\sim$15%) of contaminating star-forming objects. Strazzullo et al. (2010) used a similar template based classification system for faint radio sources in the Deep SWIRE field and demonstrated that this method is broadly consistent with two other commonly used methods of radio source classification. Namely the rest-frame colour based classification system of Smolčić et al. (2008) used for the COSMOS field and 4000-Å break strength versus radio luminosity per unit stellar mass (L/M_*) developed by Best et al. (2005a) from NVSS and FIRST radio galaxies with SDSS counterparts.

5.1 *Classification using SED fitting*

To separate the radio source hosts into red/quiescent and blue/actively star-forming populations I made use of the empirical SED templates used in the photometric redshift estimation procedure. These were described in detail in section 4.4.1 in chapter 4 and consist of 62 templates interpolated from 6 observed local galaxies. I used two approaches to the classification process.

- Method 1

  The first of these is based on the method used by Arnouts et al. (2007) to classify NIR selected galaxies in the SWIRE-VVDS fields. This method discards all the interpolated templates and uses only the 6 original empirically constructed templates based on the Ell, Sbc, Scd and Irr galaxies observed by Coleman et al. (1980) and 2 starburst galaxies from Kinney et al. (1996). The radio source host is classified according to which of these 6 templates is the best fit to the measured photometry after fixing the redshift of the templates at the photometric redshift determined by Le Phare in section 4.4.1. Galaxies which are best fit by the elliptical template galaxy are considered to be quiescent/red and all other templates are classified as star-forming/blue. Dust reddening was permitted for the templates with spectral type later than Scd.

- Method 2

  By retaining only the best fitting template the above method discards information about how strongly the observed photometry prefers this best fitting template over any of the alternative templates. This second method thus attempts to incorporate this extra information by constructing a probability density function as a function of template $\mathrm{PDF}_{\mathrm{temp}}$ from the χ^2 values determined during the photometric redshift fitting procedure. As was the case in section 4.4.3 the probability P that a given template and redshift is a true representation of the radio source host galaxy is given by the expression:

$$P \propto \exp\left(-\frac{\chi^2(z, \mathrm{temp})}{2}\right) \tag{5.1}$$

  where a χ^2 value was generated by Le Phare for every one of the 62 original templates, for redshifts between 0 and 6 in increments of 0.04 and for all permitted dust-reddening parameters. The 62 templates are separated into two classes quiescent/red and star-forming/blue and the probability P of all the templates in each class is summed to produce an overall probability that an object belongs to either class. The ratio between these summed probabilities $R_{\mathrm{class}} = \sum_{red} P_{\mathrm{temp}} / \sum_{blue} P_{\mathrm{temp}}$ is used to classify the radio source. Sources with ambigious photometry which could be equally well represented by templates in either class would then be associated with R_{class} ratios close to one. In practice the PDF is strongly peaked at the best-fitting template and consequently the ratio R_{class} is very much larger or smaller than unity for the entire population of objects. An additional complication when using this method is determining where in the spectrum of ~20 interpolated templates between the Coleman et al. (1980) Ell and Sbc templates to draw the distinction between red and blue objects. A plot of the histogram of best-fitting templates revealed that only a relatively small number of objects were fit by these interpolated templates and so the exact choice of cutoff between these two classes should not strongly influence the outcome of this classification procedure. As such I elected to use only the four templates most similar to the elliptical template as the red class and all other templates were classified as members of the blue/star-forming class.

The photometric redshift procedure permitted dust reddening for templates with spectral types later than Scd. As such the classification procedure may be slightly biased towards objects for which dust-reddening is permitted due to the extra degrees of freedom introduced into the fitting procedure for those templates. To compensate for this possible source of bias I weighted the χ^2 probabilities of all the potentially dust extincted templates by a factor of 5, corresponding to the 5 permitted values of reddening excess E(B-V).

5.2 *Comparison with colour magnitude classification*

A useful consistency check of the classification methods used above is to compare with those produced by more conventional colour magnitude relationships. Galaxies with predominantly old passively evolving stellar populations can be separated from actively star-forming galaxies on the basis of their optical colours using the $(u-r)_{\mathrm{abs}}$, or $(U-B)_{\mathrm{abs}}$ relationships determined by Baldry et al. (2004) and Bell et al. (2004b) or on their $(NUV-r)_{\mathrm{abs}}$ properties as suggested by Salim et al. (2005), where the subscript abs is used to indicate absolute magnitudes. The latter colour is more sensitive to very recent star formation which has occured within the last 10^8 yr of the galaxy's lifetime.

In order to compare the SED fitting classification with the NUV-r' colour classification I calculated the rest-frame absolute magnitudes in the NUV and r' passbands according to the method of Ilbert et al. (2005). This method minimises the template dependence of the calculated absolute magnitudes in the reference band by determining which observed band is the closest to the redshifted reference band and using this observed magnitude, the distance modulus and a small template dependent k-correction in the final $\mathrm{M}^{\mathrm{ref}}$ determination. Absolute magnitude is calculated as (Ilbert et al., 2005):

$$M^{\mathrm{Ref}} = m^{\mathrm{Obs}} - DM(z_0, H_0, \Omega_m, \Omega_\lambda) - KC(z, \mathrm{SED}) \tag{5.2}$$

where M^{Ref} is the absolute magnitude in the desired reference band, m^{Obs} is the observed magnitude in the band closest to $(1+z)$ times the reference band, $DM(z_0, H_0, \Omega_m, \Omega_\lambda)$ is the distance modulus and $KC(z, \mathrm{SED})$ is the template dependent $k-$correction calculated as:

$$KC(z, \mathrm{SED}) = (K^{\mathrm{Ref}}(z) + m^{\mathrm{Obs}}(z) - m^{\mathrm{Ref}}(z))^{\mathrm{SED}} \tag{5.3}$$

where $K^{\mathrm{Ref}}(z)$ is the k-correction of the reference band and $m^{\mathrm{Obs}}(z)$,$m^{\mathrm{Ref}}(z)$ are the observed magnitudes of the template SED in the observed and reference bands.

Figure 5.1 presents the rest-frame $(NUV - r')_{\mathrm{abs}}$ colour of sources classified as red/quiescent and blue/star-forming by the two SED classification systems described in section 5.1. As expected the SED fitting method produces classifications which are very consistent with a colour-based selection criteria. These figures also illustrate that, unlike optical and NIR selected samples, the region of the colour magnitude diagram between the peaks in the red and blue populations, referred to as the green valley, is not underpopulated. Strazzullo et al. (2010) also noted the presence of a large number of objects with green or intermediate colours in their faint radio sample in the Deep SWIRE field. The nature of these objects with intermediate colours is unclear, they may represent transitional objects which are shutting off their star-formation as a result of AGN activity in the galaxy, or be very dusty star-forming galaxies whose dust-reddening has not been properly accounted for in the template fitting procedure. Conversely they may also be passively evolving 'dead and red' galaxies whose spectra are affected by blue emission from a central AGN. Probing the nature of these intermediate objects and any potential role they have in AGN feedback processes requires further data at mid- and far-infrared wavelengths to obtain better constraints on their accretion, star-formation and dust properties. It is interesting to note that the two different methods of SED classification disagree most frequently in this intermediate colour region indicating that for many of these objects the photometry could be reasonably well-described by either a dust-extinguished star-forming or an intrinsically red elliptical galaxy template.

5.3 *Comparison with SKADS predictions*

To compare the results of this classification procedure with the SKADS Simulated Skies predictions figure 5.2 presents the total number of FRI, radio quiet quasars (RQQ) and star-forming (SF) galaxies in a one square degree field with a flux density limit of ∼100 μJy. Assuming that the majority of FRI sources are hosted in red ellipticals and the majority of radio quiet quasars and star-forming galaxies are hosted by galaxies with blue optical colours (see e.g Baldi and Capetti, 2008; Herbert et al., 2010; Simpson et al., 2012) the SKADS population predictions can be converted to a rough estimate of the expected number and fraction of red and blue sources as a function of redshift. The fractional contribution of these two classes of sources in the SKADS simulations are plotted in the bottom panel of figure 5.2, and can be compared with those produced by the two SED fitting classification procedures plotted in figure 5.3. It is immediately clear that the classification system produces fractions of red and blue sources which are reasonably consistent with the SKADS predictions in the local universe with approximately 80% star-forming galaxies at z∼0 decreasing to 60% at z∼1.0. However proceeding to higher redshifts beyond z∼1 the method dramatically over and under predicts the number of blue and red sources respectively. There are two possible explanations for this discrepancy towards higher redshifts. The first is that fainter photometry and greater uncertainty in the level of dust-extinction towards high redshift objects make it much harder to accurately constrain their intrinsic underlying SEDs, thus the colour classification at these redshifts may no longer be reliable. A second possibility is raised by the results of Janssen et al. (2012) who demonstrate that in the local universe a sub-population of LERGs are hosted in blue galaxies, with these blue LERGs becoming increasingly important at higher radio powers. Thus it is possible that the contribution of such blue LERGs increases towards higher redshifts, rendering the initial assumption that all FRI sources in the SKADS simulations are hosted in red galaxies invalid and accounting for the apparent discrepancy between the SKADS simulations and the SED classification systems.

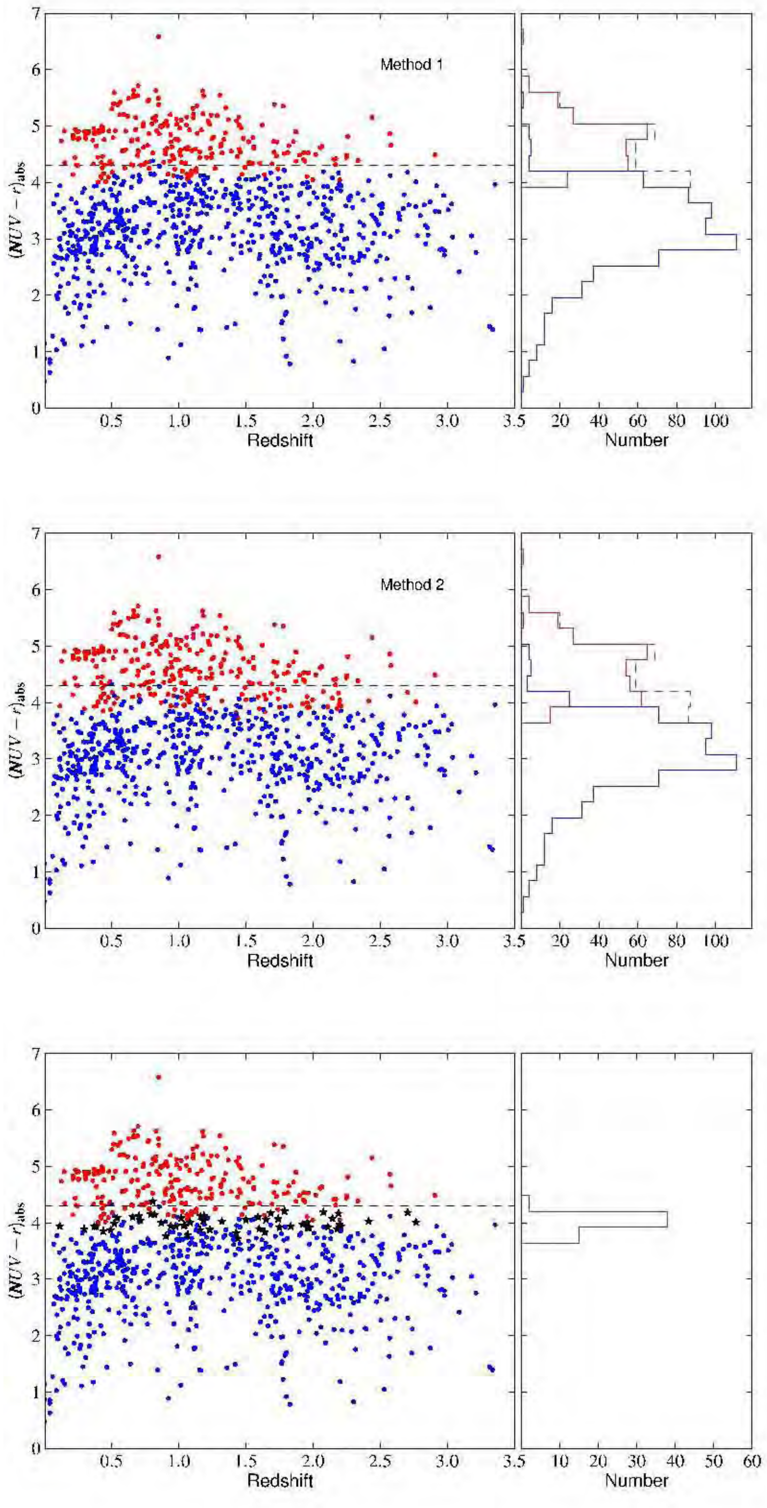

Figure 5.1: Rest-frame $NUV - r'$ colours of objects classified as red/quiescent and blue/star-forming according to their best fitting template SED's. The dashed black line at $(NUV - r')$=4.3 indicates a colour cut used to separate quiescent and star-forming galaxies (e.g. Arnouts et al., 2007), The top two panels present the classifications made by Method 1 and 2 respectively while the dashed black line in the histogram indicates the colour distribution of the whole population of radio objects. The bottom panel plots ambiguous objects as black stars.

The SED classification system used in this chapter predicts an approximately 80/20% split between star-forming and AGN galaxies in the local universe in good agreement with the SKADS predictions. At higher redshifts greater uncertainty about the nature of the host galaxies of the radio sources complicates any evaluation of the success of the SED classification method and further observations to constrain the properties of high redshift LERG and HERG host galaxies are required to address whether this classification method can be extended to higher redshifts (≥ 1). In the following sections I use stellar mass estimates obtained via SED fitting techniques as well as radio and UV-derived star-formation rates to investigate the properties of these two populations.

5.4 *Galaxy stellar masses*

The VIDEO survey team has derived stellar mass estimates for all sources in the combined CFHTLS-VIDEO survey area utilising multi-band SED fitting techniques. Physical parameters of galaxies are widely estimated by such techniques which are based on a similar premise to that used in photometric redshift estimation via template fitting (see eg. Fontana et al., 2004; Salim et al., 2005; Arnouts et al., 2007; Pozzetti et al., 2007). Namely that by fitting the observed photometry to an input set of galaxy templates whose physical parameters are known, the best fitting template can provide a reasonable estimate of the physical parameters of the observed galaxy. Parameters estimated in this fashion are influenced by the details of the chosen input galaxy templates, including their initial mass functions (IMF) and assumed star-formation histories, a detailed discussion of the effects produced by these template parameters on stellar mass estimates is presented in Pozzetti et al. (2007).

The VIDEO survey stellar masses were estimated using the Bruzual and Charlot (2003) stellar population synthesis models assuming a Chabrier (2003) IMF. The templates have exponentially declining star-formation histories with τ=(0.1, 0.3, 1, 2, 3, 4, 10, 15,30) and dust extinction is modelled according to Calzetti et al. (2000) with reddening excesses E(B-V) in the range $0 - 5$. The fitting procedure fixes the template redshifts at the best-fitting photometric redshift estimated by Le Phare.

Stellar masses estimated via this procedure for the radio sample are presented in figure 5.4. There are a number of objects in this figure whose stellar masses are considerably

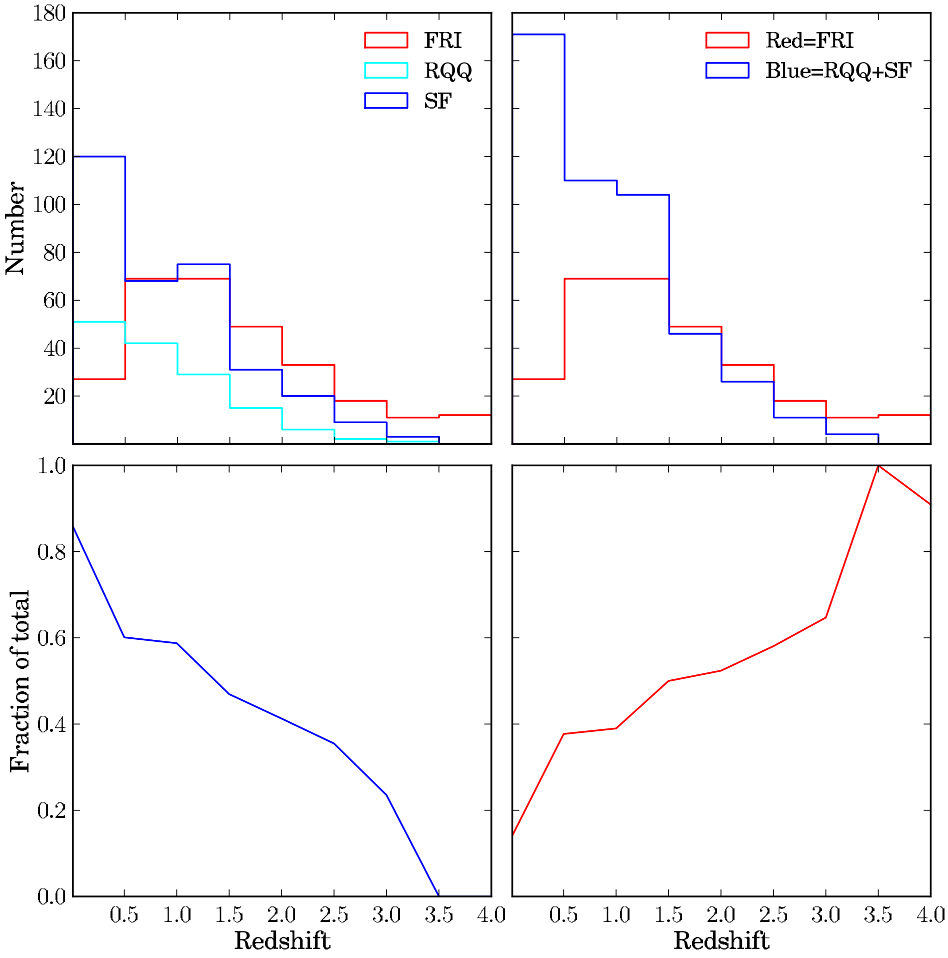

Figure 5.2: SKADS predicted number of FRI, radio-quiet quasars and star-forming galaxies in a 1 square degree field with flux density limits of ∼100 μJy. These are translated into a prediction of the number of red and blue objects in the field by assuming that FRI sources are predominantly red ellipticals while RQQ and star-forming galaxies have predominantly blue colours. Bottom panels show the fraction of these SKADS predicted red and blue objects as a function of redshift.

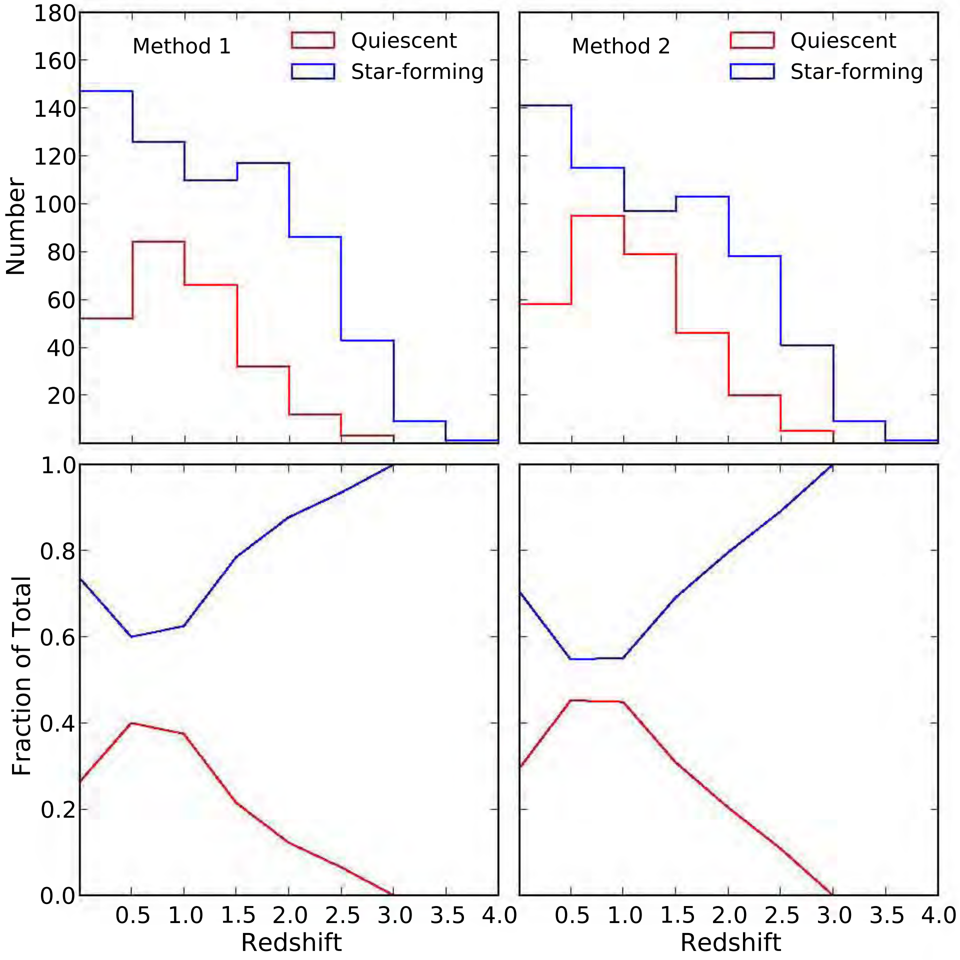

Figure 5.3: The number and fraction of red/quiescent and blue/star-forming galaxies in the VLA radio survey determined by the two methods of SED classification.

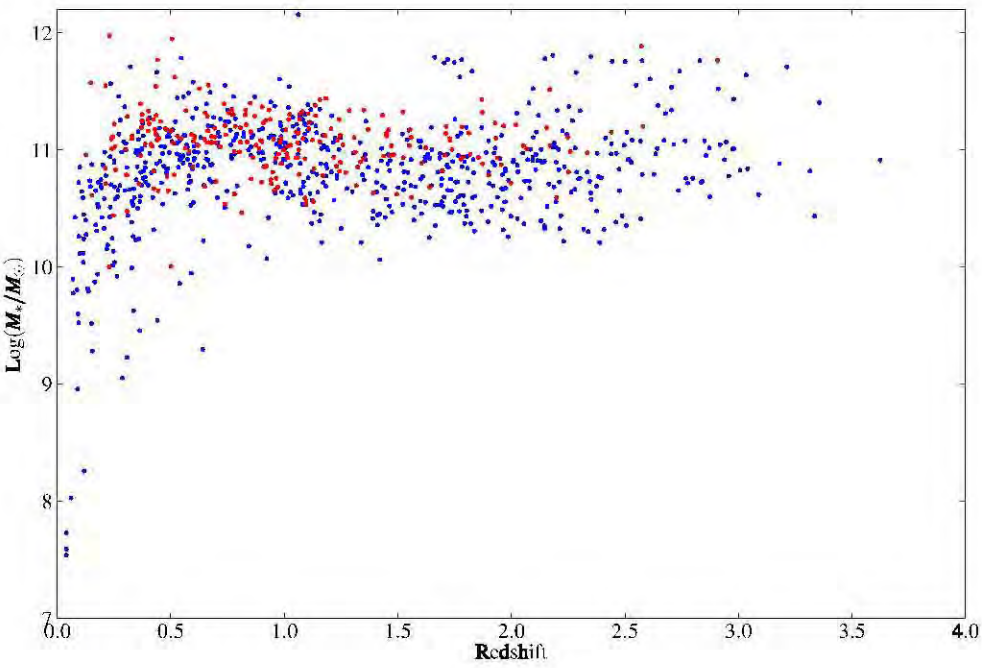

Figure 5.4: Galaxy stellar mass versus redshift for the radio sources in the VIDEO survey. Galaxies classified as red/quiescent or blue/star-forming are plotted as red and blue points respectively.

higher than the general population of radio sources, with Log($M_*/M_\odot$) > 11.5, the mass estimates for these objects should be treated with caution and may result from an underestimation of the dust content of these galaxies in the template fitting procedure. Stellar masses estimated from SED fitting are more uncertain at z≥1.5 in the absence of data at wavelengths longer than K_s band. However powerful radio-galaxies are known to be hosted by massive elliptical galaxies with typical stellar masses approaching Log($M_*/M_\odot$) > 11.5 (Seymour et al., 2007).

5.5 *Correlation of radio luminosity with black hole mass*

The first evidence that radio luminosity might be correlated with the mass of the central black hole ($M_{\rm bh}$) of an AGN was provided by Franceschini et al. (1998) who found a tight correlation between total and nuclear radio luminosity at 5 GHz with $M_{\rm bh}$ for a small sample of local AGN. As optically luminous quasars with quite comparable optical properties can differ in their radio luminosities by several orders of magnitude it was postulated that the mass of the central AGN might be the key to understanding why certain quasars are more radio-loud than others. However the results of more recent studies of the correlations between $M_{\rm bh}$ and radio luminosity and loudness have produced contrasting results, studies by Laor (2000); Lacy et al. (2001); McLure et al. (2004) and Herbert et al. (2011) suggest that radio luminosity is loosely correlated with M_{bh} while Laor (2000); McLure and Dunlop (2001) and McLure and Jarvis (2004) find evidence of a statistical difference in the M_{bh} of radio-loud and radio-quiet quasar populations. In contrast works by Ho (2002) and Woo and Urry (2002) find no evidence of such correlations. Investigations into this question have also suggested that the presence or absence of a correlation may be influenced by the accretion mode or morphological classification of the radio sources, in McLure et al. (2004) evidence of a correlation was only found when restricting the sample of radio sources to those with HERG spectra or fat-double/FRII morphological classifications.

To determine whether there was evidence of a correlation between radio luminosity and black hole mass in the sample of AGN in the VIDEO survey in figure 5.5 I show the stellar mass versus radio luminosity of all the red/quiescent objects identified below z$\sim$1. As a result of the well-known correlation between stellar bulge mass and black hole mass in bulge-dominated galaxies (Kormendy and Richstone, 1995; Magorrian et al., 1998; McLure and Dunlop, 2002) any correlation between luminosity and M_{bh} should still be approximately discernable in these stellar mass versus luminosity relationships. As a flux limited survey has an increasing detection threshold in luminosity and stellar mass towards higher redshifts the sample was binned into four redshift bins to minimise the bias introduced by this selection effect. The sample was restricted to detections below z$\leq$1 as a result of the uncertainty surrounding the reliability of the SED fitting classification procedure beyond this threshold. I performed a Kendall τ and Spearman rank ρ correlation test on each of the four redshift bins, the results of these tests are summarised in table 5.1. In these tests the correlation was found to be significant only in the lowest redshift bin z<0.4, the results in this bin could be strongly influenced by the selection of higher mass and higher luminosity objects with increasing redshift in the redshift range 0$\leq$z$\leq$0.4. To determine whether the observed correlation between mass and luminosity is produced by the underlying correlation of both these quantities with redshift I performed a Spearman rank partial correlation test (Macklin, 1982). This test yielded a partial correlation co-efficient of ρ=0.38 (2.17σ), thus it would seem unlikely that a correlation between mass and luminosity exists at low redshifts.

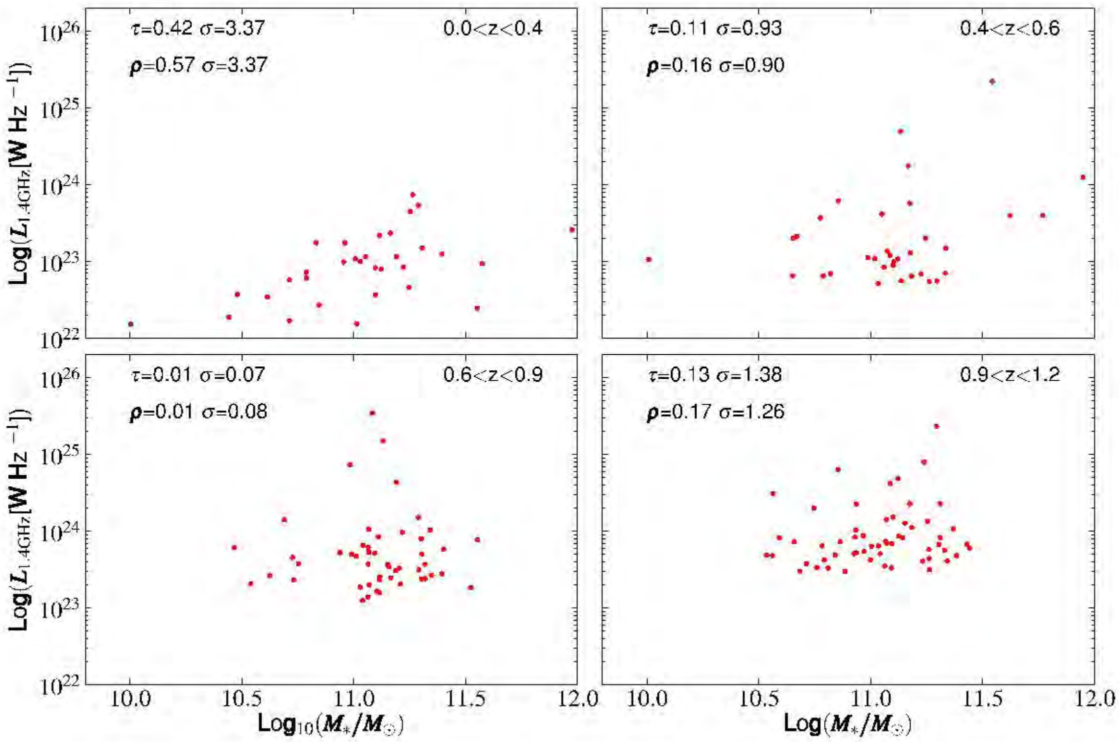

Figure 5.5: Radio luminosity versus stellar mass for galaxies classified as red/quiescent by Method 1 of section 5.1. The results of the Kendall τ (τ,σ) and Spearman rank (ρ,σ) tests performed in each redshift bin are indicated in the top left corner of the plots.

Table 5.1: Results of the Spearman rank (ρ, σ) and Kendall τ (τ, σ) tests for correlation between stellar mass and radio luminosity. The tests were performed on the Red/Quiescent population identified by the two different classification methods outlined in section 5.1

Method 1					Method 2				
z	τ	σ	ρ	σ	z	τ	σ	ρ	σ
0<z< 0.4	0.42	3.37	0.57	3.37	0.0<z< 0.4	0.45	3.84	0.60	3.89
0.4<z< 0.6	0.11	0.93	0.16	0.90	0.4<z< 0.6	0.14	1.18	0.20	1.12
0.6<z< 0.9	0.01	0.07	0.01	0.08	0.6<z< 0.9	0.04	0.47	0.06	0.44
0.9<z< 1.2	0.13	0.08	0.17	1.26	0.9<z< 1.2	0.09	1.10	0.13	1.01

In all other redshift bins there is no evidence of a correlation, if the red population selected in this chapter comprises primarily low luminosity LERG's or FRI sources then the results towards higher redshifts ($\geq$ 0.4) are in rough agreement with the results of McLure et al. (2004).

5.6 *Star-forming galaxies*

Radio emission from star-forming galaxies generated by synchrotron emission from supernovae explosions has the potential to provide a high resolution, dust unbiased tracer of star-formation activity out to high redshifts (Condon, 1992; Yun et al., 2001). However the physics linking star-formation to radio emission is highly complex and the strongest evidence in favour of radio emission as a reliable tracer of star-formation activity is provided by its observed tight correlation with far-infrared emission. AGN contamination of radio selected star forming samples may also provide a significant source of bias when trying to accurately constrain the cosmic star-formation history, as AGN emission will result in higher estimates of star-formation rates and these sources may evolve quite differently to the general star-forming population (e.g. Smolčić et al., 2009b,a). I thus compare the star-formation rate (SFR) estimated from the radio emission ($\mathrm{SFR_{radio}}$) to another commonly used star-formation rate estimator, based on UV continuum emission ($\mathrm{SFR_{UV}}$), to determine whether SF rates from these two methods are comparable and whether deviations in $\mathrm{SFR_{radio}}$ from $\mathrm{SFR_{UV}}$ can be used to identify contaminating AGN in the radio sample.

In this comparison I used both of the proposed conversions from 1.4 GHz luminosity to SFR rate in the literature, the one proposed by Condon et al. (1998) and Condon et al. (2002) is given by:

$$\mathrm{SFR_{radio}}(\mathrm{M_{\odot}yr^{-1}}) = 1.2006 \times 10^{-21}\mathrm{L_{1.4GHz}}. \tag{5.4}$$

While Bell (2003) calculate the conversion as:

$$\begin{aligned}\mathrm{SFR_{radio}}(\mathrm{M_{\odot}yr^{-1}}) &= 5.52 \times 10^{-22} L_{1.4\mathrm{GHz}} & L < L_c \\ &= \frac{5.52 \times 10^{-22} L_{1.4\mathrm{GHz}}}{0.1 + 0.9\left(\frac{L}{L_c}\right)^{0.3}} & L < L_c\end{aligned} \tag{5.5}$$

where $L_c = 6.4 \times 10^{21}$W Hz^{-1}. The Bell (2003) conversion implies slightly higher SFRs for low luminosity radio sources below the L_c threshold and lower SFRs overall compared to the Condon et al. (2002) conversion.

UV continuum flux provides an excellent probe of star formation rate as this part of the spectrum is dominated by emission from young stars, with minimal contamination from older stellar populations. Thus at these wavelengths the SFR scales approximately linearly with luminosity. Kennicutt (1998) gives the conversion between UV flux in the wavelength range 1500 – 2800Å and SFR as:

$$\mathrm{SFR_{UV}(M_{\odot}yr^{-1})} = 1.4 \times 10^{-28}\mathrm{L}_{\nu}(\mathrm{erg\ s^{-1}\ Hz^{-1}}) \tag{5.6}$$

To determine an estimate of the UV flux emitted by the radio sources I used the UV emission from the scaled best-fitting template obtained by the photometric redshift estimation procedure. A comparison between the two different SFR estimates is presented in figure 5.6. It is clear that the radio based SFR estimators are higher than those derived from the template UV fluxes, with the Condon et al. (2002) estimates being higher than those produced by Bell (2003). This discrepancy between radio and UV derived star-formation rates has been observed in previous studies (Hopkins et al., 2001) and is ascribed to the effects of dust obscuration at UV wavelengths. Although the templates in this work have been corrected for extinction using a simple prescription based on the correlation between observed reddening excess and UV attenuation (Prevot et al., 1984), this is an inadequate representation of the dependence of total UV attenuation on a range of factors including star-formation rate (Hopkins et al., 2001), the age of the stellar population of the galaxy (Bell, 2002; Calzetti et al., 2005) and the amount and geometry of the dust. Attempts have been made to calibrate these dependencies and correct the observed UV emission for dust-attenuation with varying degrees of success (Hopkins et al., 2001; Salim et al., 2007), despite these efforts accurately constraining dust-attenuation based solely on contraints from optical through to near-infrared wavelengths remains a challenging problem.

There is a clear tendency for the ratio of $\mathrm{SFR_{radio}/SFR_{UV}}$ to increase towards higher redshifts. This is almost certainly due to the increased contribution from AGN at these redshifts but may also be partially due to inadequate corrections for dust extinction in the template fitting. If dust extinction is underestimated objects may be intrinsically bluer and brighter than their templates imply, with the result that the template based UV SFR estimates are systematically low. In the extreme case of a totally obscured starburst component where the star formation makes no contribution to the fitted SED the template fitting procedure will be unable to reconstruct the true SED and star-formation properties of the galaxy. It is encouraging to see that in the local universe (z≤1) the SED template based classification system has preferentially classified objects with a good agreement between their radio and UV based SFR estimates as SF/blue. While objects whose high $\mathrm{SFR_{radio}/SFR_{UV}}$ ratios would tend to suggest that their radio emission is primarily driven by AGN accretion are classified as quiescent/red. There is possible evidence of two slightly diverging populations with galaxies above the dashed line in figure 5.6 having slightly steeper $\mathrm{SFR_{radio}/SFR_{UV}}$ ratios which may indicate a division between the AGN and star-forming populations. It also clear that the SED fitting selection process is not clean, as the blue star-forming galaxies it selects are not associated with a clearly identifiable star-forming population in these diagrams, and a large number of sources with suspiciously high $\mathrm{SFR_{radio}/SFR_{UV}}$ ratios are classified as blue/star-forming. This tendency is exacerbated towards higher redshifts where it is clear that the SF/blue class defined by template fitting contains a large fraction of contaminating AGN.

Another possible method to identify AGN within the radio sample is to compare the results of fitting AGN templates versus galaxy templates to the observed photometry. The Le Phare photometric redshift procedure fitted a set of AGN templates in addition to the galaxy templates and determined χ^2 for the best fitting AGN and galaxy template as χ_{qso} and χ_{best} respectively. It is thus possible to identify sources whose photometry is more consistent with an AGN SED than a galaxy SED by determining whether $\chi_{\mathrm{qso}} \leq \chi_{\mathrm{best}}$. Figure 5.7 indicates the position of AGN candidates selected in this manner in the $\mathrm{SFR_{radio}}$ versus $\mathrm{SFR_{UV}}$ plane. These AGN candidates are predominantly located towards higher ratios of $\mathrm{SFR_{radio}/SFR_{UV}}$ lending support to the notion that these ratios might be useful indicators of AGN activity in radio sources. There is also a cluster of ~ 10 objects at high redshift (z≥1.5) which appear to be radio quiet quasars as they have SED templates consistent with an AGN but low radio luminosities, consequently their $\mathrm{SFR_{radio}/SFR_{UV}}$ ratios are more consistent with those of a star-forming galaxy. Although the AGN template library used to determine χ_{qso} consists of both Type 1 & 2 AGN as well as composite AGN and SF sources this method will clearly have greater difficulty identifying very obscured Type 2 AGNs whose SEDs are strongly influenced by the emission from the host galaxy.

Further differences between normal star-forming galaxies and those hosting an AGN can be discerned in their specific star-formation rates (SSFRs) and M_*. Work by Salim et al.

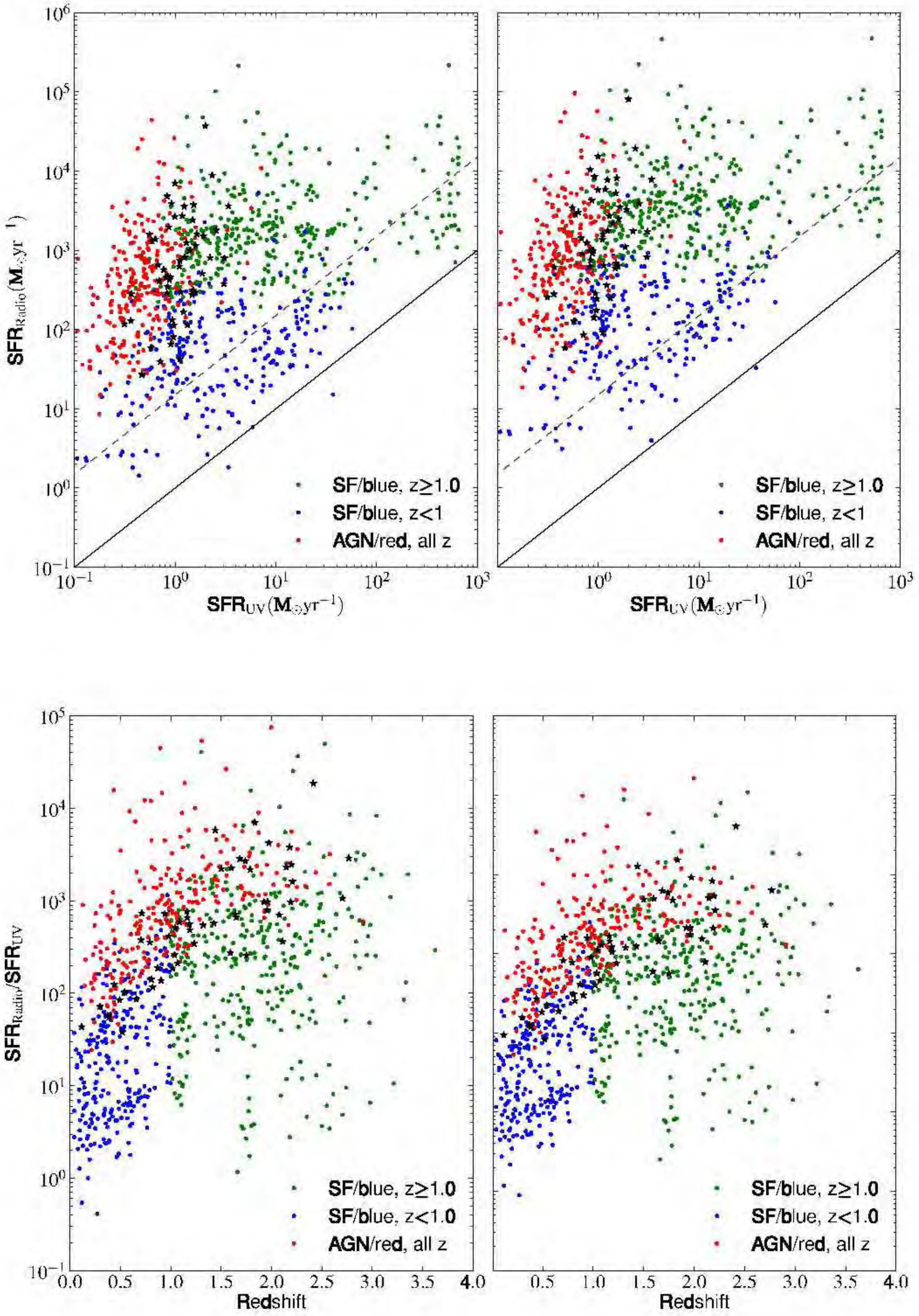

Figure 5.6: Comparison of radio and UV based SFR estimates. Figures on the left hand side are based on the Bell (2003) estimates of SFR$_{\rm radio}$ and those on the right on the Condon et al. (2002) conversions. The solid and dashed black lines in the top figure are there to guide the eye and are plotted at SFR$_{\rm radio}$ =SFR$_{\rm UV}$ and SFR$_{\rm radio}$ =15 SFR$_{\rm UV}$ respectively.

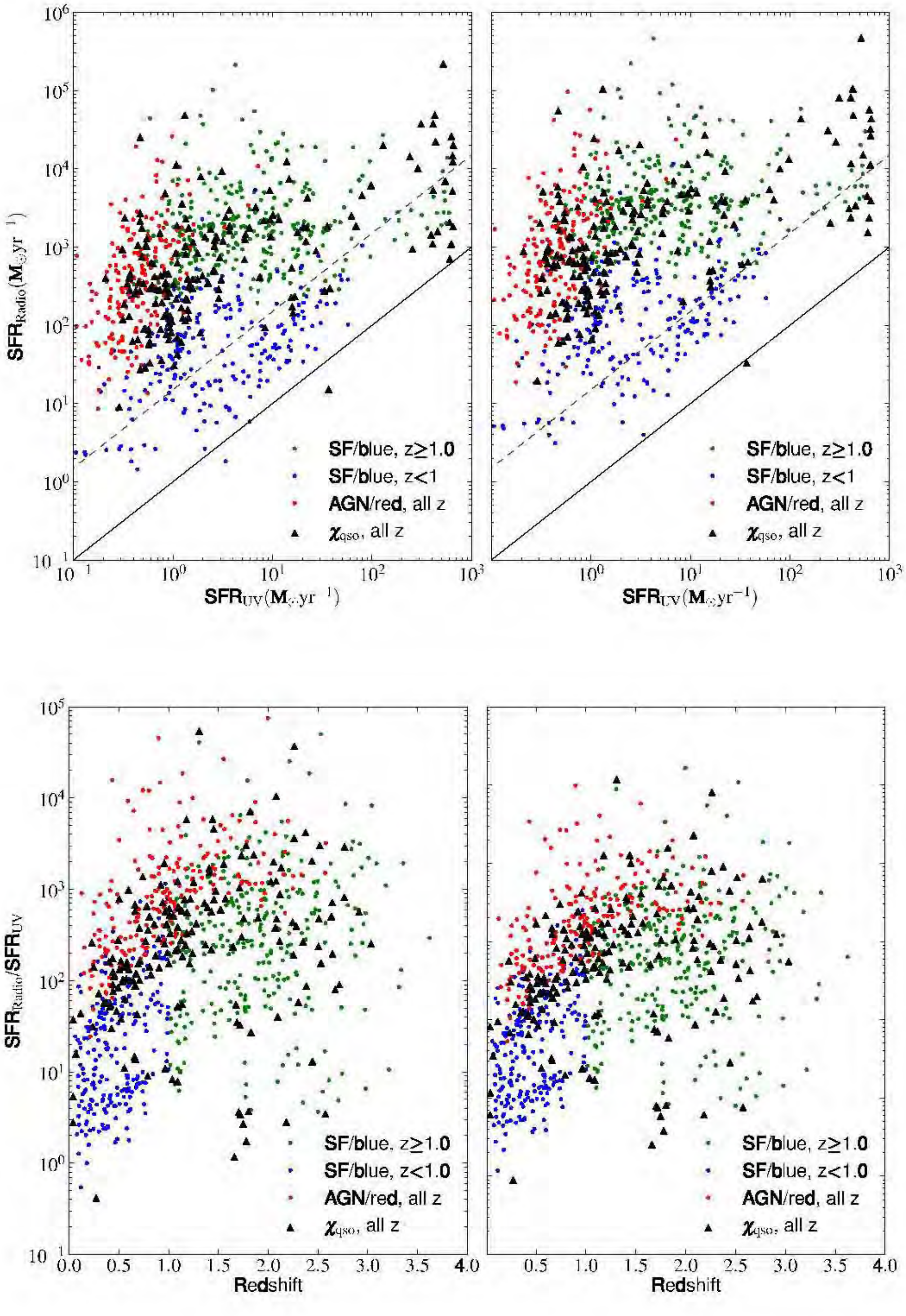

Figure 5.7: Comparison of radio and UV based SFR estimates. Figures on the left hand side are based on the Bell (2003) estimates of SFR$_{\mathrm{radio}}$ and those on the right on the Condon et al. (2002) conversions. The solid and dashed black lines in the top figure are there to guide the eye and are plotted at SFR$_{\mathrm{radio}}$ =SFR$_{\mathrm{UV}}$ and SFR$_{\mathrm{radio}}$ =15 SFR$_{\mathrm{UV}}$ respectively. The black triangles indicate sources whose best fit template SED was an AGN template rather than a galaxy template.

(2007) found that normal star-forming galaxies and galaxies hosting an AGN preferentially occupy different regions of the SSFR versus M_* diagram, although these regions have significant overlap. Their work identifies AGN and star-forming galaxies on the basis of their BPT emission line diagnostics and uses UV continuum emission to estimate star-formation rates. Their sample comprises galaxies in the local universe at z$\sim$0.1. They found that star-forming galaxies form an approximately linear sequence in SSFR versus M_*, and that galaxies whose spectra have some indication of both AGN emission and ongoing star-formation are located towards the higher mass end of this sequence. Galaxies with only AGN emission features form an extended tail towards very low SSFRs. Interestingly when separating the AGN in their sample into strongly and weakly accreting components, the strong accretors appear to be concentrated towards higher SSFR rates with stronger evidence of ongoing star-formation. To compare with their results in figure 5.8 I show the SSFR and M_* of all the radio sources in both a low ($z < 1$) and high redshift ($z > 1$) bin. The regions identified with predominantly star-forming and AGN galaxies by Salim et al. (2007) are indicated by coloured lines in these plots. In the low redshift diagram there is a clear linear sequence of objects in the star-forming region of the diagram which are identified as star-forming/blue galaxies in our radio sample. However there is also a well separated group of objects which are classified as blue/star-forming occupying the region which comprises both composite (AGN+SF) and AGN sources. Only the most extreme red objects with the lowest SSFR are identified as AGN by the SED fitting procedure. Figure 5.9 shows the positions of AGN candidates selected on the basis of having lower $\chi^2_{\rm qso}$ values for an AGN template than a galaxy template. In the low redshift plot these sources are also clearly located in the region of the plot identified as being associated with AGN and composite sources by Salim et al. (2007), and well separated from the main linear sequence of star-forming galaxies. As such figures 5.8 and 5.9 would seem to indicate that at least some fraction of the blue/star-forming sources located in the composite region of the SSFR vs M_* diagram must be associated with AGN activity and further observations are needed to clarify the exact nature of sources in this region of the diagram. This may link with the earlier observation that the radio sample has a population of objects with intermediate colours which are difficult to positively classify as AGN, star-forming (SF) or likely composite AGN+SF sources.

In the high redshift bin ($z>1$) the derived SSFRs are shifted towards higher values and

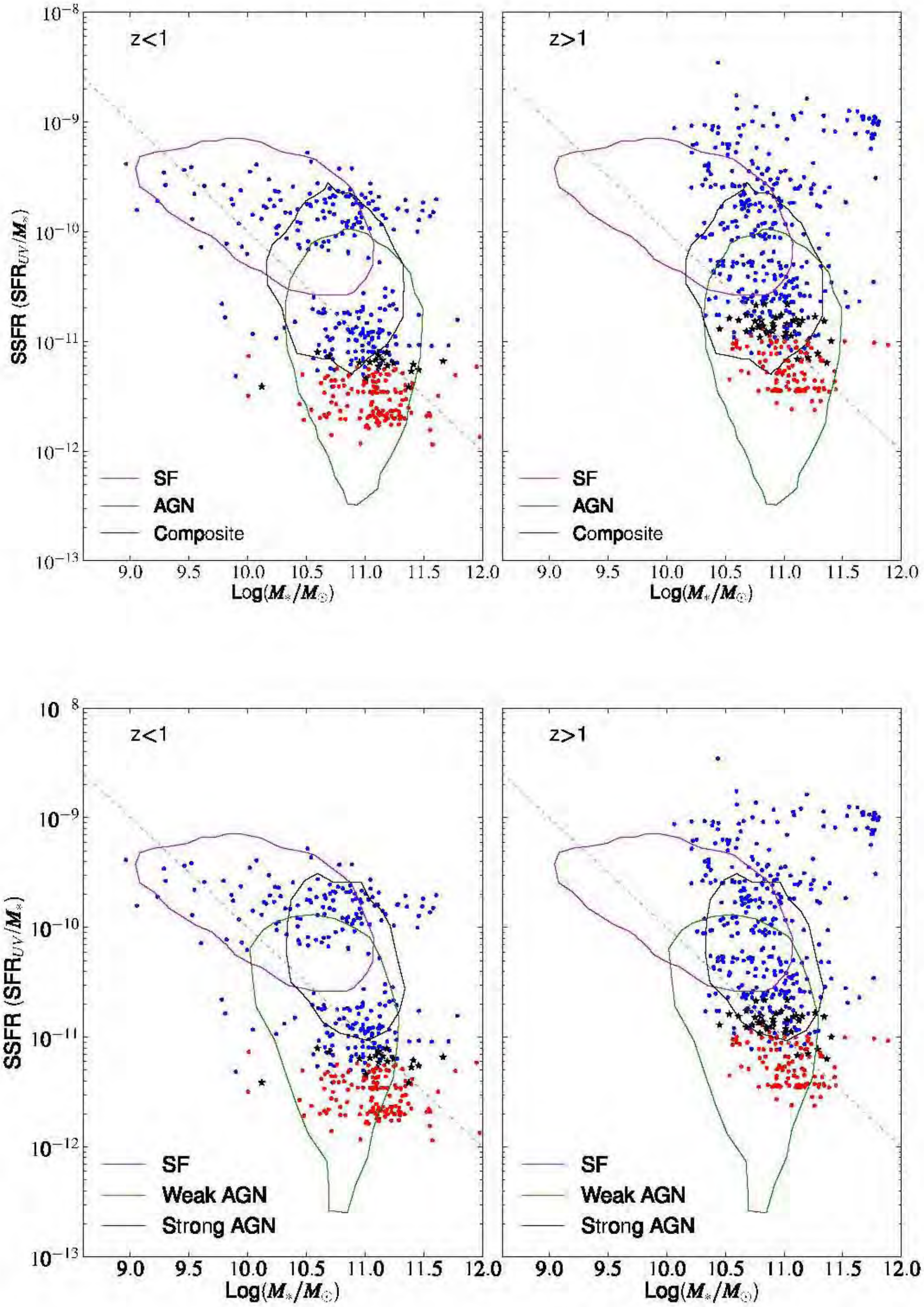

Figure 5.8: SSFR versus M_* for radio galaxies in the VIDEO survey. Objects classified as blue/red are plotted as red and blue points respectively. Ambiguous objects classified as blue by Method 1 and red by Method 2 of section 5.1 are plotted as black stars. The coloured lines indicate the regions occupied by star-forming (SF) galaxies and the different AGN classes in Salim et al. (2007). The grey dashed line is plotted at a SFR of 1 $M_\odot\ yr^{-1}$.

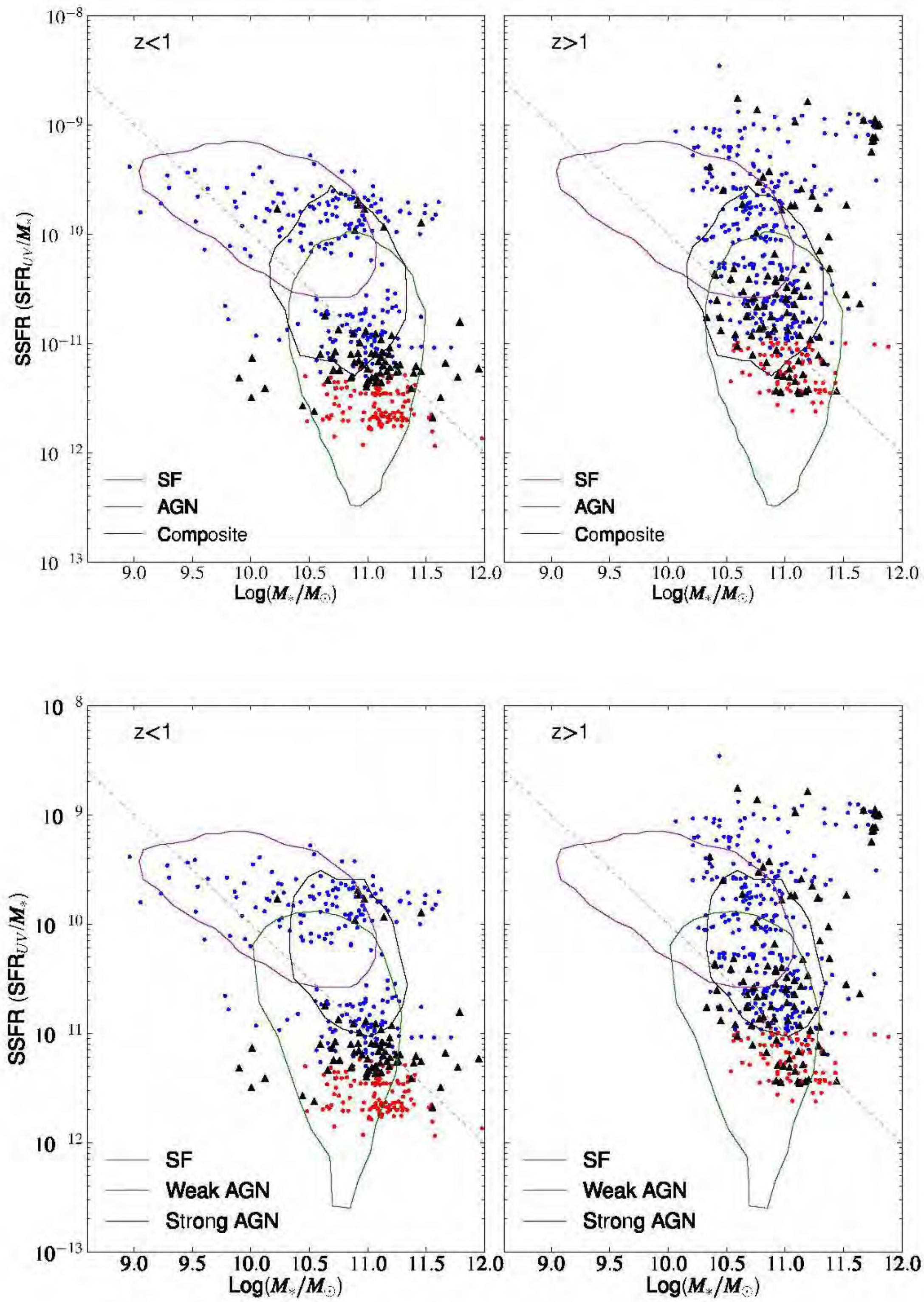

Figure 5.9: SSFR versus M_* for radio galaxies in the VIDEO survey. Objects classified as blue/red are plotted as red and blue points respectively. The black triangles indicate sources whose best fit template SED was an AGN template rather than a galaxy template. The coloured lines indicate the regions occupied by star-forming (SF) galaxies and the different AGN classes in Salim et al. (2007). The grey dashed line is plotted at a SFR of 1 $M_\odot\,\mathrm{yr}^{-1}$.

it difficult to make a direct comparison with the locally derived relations in Salim et al. (2007), however its clear that the SSFRs vs M_* of the radio population forms a continuous sequence with the objects with the lowest SSFRs being once again identified as red/AGN. As the sequence is continuous with no hint of bimodality it is difficult to determine where to draw the dividing line between AGN and star-forming galaxies and to make inferences about the success or failure of the SED fitting classification procedure.

It also interesting to note that a high proportion (∼40%) of the objects with very high stellar mass estimates, $\mathrm{Log}(M_*/M_\odot) > 11.5$, have blue templates and are better fit by an AGN template than a galaxy template. As such the K_s band in these objects is likely dominated by AGN light and not stellar light further indicating that these high stellar mass estimates may be unreliable.

5.7 *Conclusions*

This chapter has presented an investigation into the properties of the host galaxies of faint radio sources. The main results are that classification using SED fitting techniques can successfully identify the most likely blue/star-forming and red/quiescent sources out to redshifts of ~ 1. Assuming that the blue and red sources classified in this manner are predominantly star-forming galaxies and FRI sources respectively the total number of sources in each class are reasonably consistent with the predictions of the SKADS simulations. At high redshifts beyond z∼1 the success of this classification method is unclear as a result of the uncertainties surrounding the contribution from blue LERGs at these redshifts. However there is some evidence, in the form of both high $\mathrm{SFR}_{\mathrm{radio}}$ and low SSFRs that some of the sources classified as blue/star-forming by the SED method are more likely to be low luminosity AGN. At all redshifts there is a non-negligable contribution from sources with intermediate colours, and relatively low SSFRs which cannot be easily classified by this method and further observations and mid- and far-infrared wavelengths are required to characterise their nature and possible evolutionary significance. The infrared observations are particularly helpful as radio emission is known to be correlated with far- and mid-infrared emission in star-forming galaxies (Jarvis et al., 2010; Ivison et al., 2010; Garrett, 2002). Excess radio emission from the powerful jets of radio-loud AGN as well as excess mid-infrared emission from the obscuring torus in the unified model of “quasar” mode accretors can thus be used to identify AGN candidates in the radio sample (e.g. Seymour et al., 2008). AGN candidates were also identified on the basis of whether their photometry was best fit by a galaxy or an AGN SED template. These objects were shown to be preferentially associated with high $\mathrm{SFR}_{\mathrm{radio}}/\mathrm{SFR}_{\mathrm{UV}}$ ratios, and in the local universe occupy a region of the SSFR versus M_* diagram identified as being predominantly occupied by AGN (Salim et al., 2007). Additionally these sources are very clearly separated from the general star-forming galaxy population in this diagram. This provides encouraging evidence that such an AGN versus galaxy SED based classification method could be used to identify potential AGN candidates in radio samples.

Finally there appears to be no evidence of a correlation between the mass of the central black hole and radio luminosity in low luminosity AGN’s.

Chapter 6

Summary and future work

This thesis presents two new studies of the evolution of low luminosity radio sources, one over a larger survey area of 2.75 degrees^2 limited to redshifts of ∼1.2 with only relatively coarse redshift information derived from single band photometry. The second study is limited to a smaller survey area but makes use of deeper radio data and multi-band optical and near-infrared photometry in the CFHTLS and VIDEO surveys to obtain more accurate photometric redshift estimates. This deeper study is therefore able to investigate the RLF out to redshifts of ∼2.5. The results indicate an increase in the number density of radio sources out to redshifts of ∼ 1.2 with the first study implying slightly less evolution over this redshift interval. These results are in broad agreement with a number of previous investigations of the evolution of low luminosity radio sources (e.g. Clewley and Jarvis, 2004; Sadler et al., 2007; Donoso et al., 2009; Smolčić et al., 2009b; Strazzullo et al., 2010; Simpson et al., 2012). Beyond z∼1.2 there is evidence of a slowing of this evolution or even a possible decline in the number densities. A similar decline has been noted in the RLF of the *Suburu/XMM-Newton* Deep field (Simpson et al., 2012) and there have been other suggestions of a possible high redshift cutoff in the number densities of low luminosity radio sources (Rigby et al., 2007, 2011; Waddington et al., 2001) which may be consistent with this decline.

As complementary multi-wavelength datasets will be vitally important to the goals of future continuum surveys with SKA pathfinder telescopes this thesis also investigated whether the lower resolution of these planned surveys would significantly impact their ability to identify multi-wavelength counterparts to the faint radio population. This question was addressed via a comparative study of counterparts identified by the likelihood ratio technique at resolutions of 6, 10 and 15 arcsecs respectively, where the 10 and 15 arcsec resolutions correspond to the planned resolutions of EMU and WODAN respectively. The results indicate that at a flux density limit of 100μJy with complementary data complete to K$_s$ <22.6 the likelihood ratio is able to identify counterparts to ∼89% of the radio sources at 6 arcsec resolution with only a small decrease in completeness by 3 and 5% when degrading the resolution to 10 and

15 arcsec. However the results also indicate that completeness decreases sharply towards lower flux densities, as these surveys have planned depths of 10 – 50 μJy this question should be revisited at a future date with deeper radio data.

Future surveys with SKA pathfinders require a means to separate the star-forming and AGN contributions at faint flux densities. Given the difficulty of obtaining spectroscopic observations over large swathes of sky for such sources, in the final chapter of this thesis I investigated the effectiveness of SED fitting techniques in identifying these two populations. AGN identification was achieved using two methods, the first is based on the observed tendency for LERG AGN to be associated with giant 'dead and red' ellipticals (Baldi and Capetti, 2008; Herbert et al., 2010; Smolčić and Riechers, 2011; Best and Heckman, 2012), thus objects whose photometry was best fit by a red elliptical template were classified as AGN. These were associated with high $\mathrm{SFR_{radio}/SFR_{UV}}$ ratios indicating a possible AGN origin for the radio emission and in the local universe (z≤1) occupy a region of the SSFR versus M_* diagram known to be preferentially occupied by AGN sources (Salim et al., 2007). The second method determines whether the object photometry is best fit by a galaxy or an AGN SED, this method also selects objects with high $\mathrm{SFR_{radio}/SFR_{UV}}$ ratios in the AGN region of the local SSFR versus M_* diagram. These two techniques may be complementary as the second method identifies objects whose bluer optical colours preclude AGN classification via the first method. Comparisons with the SKADS simulations indicate that SED classification identifying red ellipticals as AGN is reasonably successful at low redshifts but fails towards higher redshifts where fainter photometry makes it harder to constrain dust parameters and distinguish between intrinsically red objects and dust-reddened star-forming galaxies. Also AGN may have bluer colours and higher rates of ongoing star-formation at higher redshifts and higher radio luminosities (Hardcastle et al., 2010; Seymour et al., 2011).

Future extensions of the work presented here include determining more accurate estimates of the errors on the RLF derived for the combined VLA-VIDEO survey by incorporating the photometric redshift errors using Monte Carlo techniques. The addition of mid-infrared observations from the SWIRE (Lonsdale et al., 2003) and Spitzer Extragalactic Representative Volume (SERVS; Mauduit et al., 2012) surveys and far-infrared observations from *Herschel* Multi-tiered Extragalactic Survey (HERMES; Oliver et al., 2012) would allow me to extend the classification and investigation of the properties of faint radio sources presented in chapter 5 and would be particularly useful in constraining the nature of sources with intermediate optical colours occupying the region between the red sequence and the blue cloud. This additional data could be used to identify both radio-loud and radio-quiet AGN and star-forming galaxies more securely and possibly out to higher redshifts allowing me to derive separate RLF for each of these classes and determining which sources are primarily driving the different evolutionary trends observed in the RLF of the total faint radio source population.

Mid and far-infrared data could also be used to study the star-formation activity of AGN across cosmic time to determine if AGN feedback processes influence the star-formation properties of their host galaxies and the relative significance of the two postulated modes of AGN feedback as a function of cosmic time.

A further useful extension of this work would be to obtain follow-up spectroscopy of the radio sources. Spectroscopy would result in more accurate redshift determinations used in studies of the RLF and could be used to identify and study the evolution of HERG and LERG radio sources out to higher redshifts. Reliable separations of the HERG and LERG populations would also be extremely useful in studies of the role of AGN feedback in shaping the global star-formation history of the universe.

The LR study presented in chapter 3 could also be extended in a number of ways. Incorporating information about the expected colour distribution of the radio source counterparts may provide a means to mitigate the difficulties of cross-matching at lower resolution, the method could also be adapted to take account of non-circular beam profiles. A further, more challenging, extension of this work would be to use a LR method to identify counterparts to multi-component radio sources. These sources will form an important constituent of future wide, deep surveys which will produce large samples of such source rendering the simple visual inspection methods used in this work impractical as a means of identifying their counterparts.

The deep radio observations used in this thesis in combination with excellent, cutting-edge observations from optical through to far-infrared wavelengths will thus put us in an excellent position to gain a clearer understanding of galaxy formation across cosmic time and the role that AGN feedback has in governing this process.

Bibliography

Abazajian, K. N., Adelman-McCarthy, J. K., Agüeros, M. A., Allam, S. S., Allende Prieto, C., An, D., Anderson, K. S. J., Anderson, S. F., Annis, J., Bahcall, N. A., et al.: 2009, *The Astrophysical Journal Supplement Series* **182**, 543

Allen, S. W., Dunn, R. J. H., Fabian, A. C., Taylor, G. B., and Reynolds, C. S.: 2006, *Monthly Notices of the Royal Astronomical Society* **372**, 21

Alonso-Herrero, A., Ramos Almeida, C., Mason, R., Asensio Ramos, A., Roche, P. F., Levenson, N. A., Elitzur, M., Packham, C., Rodríguez Espinosa, J. M., Young, S., Díaz-Santos, T., and Pérez-García, A. M.: 2011, *The Astrophysical Journal* **736**, 82

Antonucci, R. and Miller, J. S.: 1985, *The Astrophysical Journal* **297**, 621

Arnouts, S., Cristiani, S., Moscardini, L., Matarrese, S., Lucchin, F., Fontana, A., and Giallongo, E.: 1999, *Monthly Notices of the Royal Astronomical Society* **310**, 540

Arnouts, S., Walcher, C. J., Le Fèvre, O., Zamorani, G., Ilbert, O., Le Brun, V., Pozzetti, L., et al.: 2007, *Astronomy & Astrophysics* **476**, 137

Assef, R. J., Kochanek, C. S., Brodwin, M., Brown, M. J. I., Caldwell, N., Cool, R. J., Eisenhardt, P., Eisenstein, D., Gonzalez, A. H., Jannuzi, B. T., Jones, C., McKenzie, E., Murray, S. S., and Stern, D.: 2008, *The Astrophysical Journal* **676**, 286

Avni, Y. and Bahcall, J. N.: 1980, *The Astrophysical Journal* **235**, 694

Babbedge, T. S. R., Rowan-Robinson, M., Gonzalez-Solares, E., Polletta, M., Berta, S., Pérez-Fournon, I., Oliver, S., et al.: 2004, *Monthly Notices of the Royal Astronomical Society* **353**, 654

Baldi, R. D. and Capetti, A.: 2008, *Astronomy and Astrophysics* **489**, 989

Baldry, I. K., Glazebrook, K., Brinkmann, J., Ivezić, Ž., Lupton, R. H., Nichol, R. C., and Szalay, A. S.: 2004, *The Astrophysical Journal* **600**, 681

Baldry, I. K., Robotham, A. S. G., Hill, D. T., Driver, S. P., Liske, J., Norberg, P., Bamford, S. P., Hopkins, A. M., Loveday, J., et al.: 2010, *Monthly Notices of the Royal Astronomical Society* **404**, 86

Baldwin, J. A., Phillips, M. M., and Terlevich, R.: 1981, *Publications of the Astronomical Society of the Pacific* **93**, 5

Ball, N. M., Brunner, R. J., Myers, A. D., Strand, N. E., Alberts, S. L., and Tcheng, D.: 2008, *The Astrophysical Journal* **683**, 12

Barbosa, F. K. B., Storchi-Bergmann, T., Cid Fernandes, R., Winge, C., and Schmitt, H.: 2009, *Monthly Notices of the Royal Astronomical Society* **396**, 2

Bauer, F. E., Alexander, D. M., Brandt, W. N., Hornschemeier, A. E., Vignali, C., Garmire, G. P., and Schneider, D. P.: 2002, *The Astronomical Journal* **124**, 2351

Baum, S. A., Zirbel, E. L., and O'Dea, C. P.: 1995, *The Astrophysical Journal* **451**, 88

Becker, R. H., White, R. L., and Helfand, D. J.: 1995, *The Astrophysical Journal* **450**, 559

Bell, E. F.: 2002, *The Astrophysical Journal* **577**, 150

Bell, E. F.: 2003, *The Astrophysical Journal* **586**, 794

Bell, E. F., McIntosh, D. H., Barden, M., Wolf, C., Caldwell, J. A. R., Rix, H.-W., Beckwith, S. V. W., et al.: 2004a, *The Astrophysical Journal* **600**, L11

Bell, E. F., Wolf, C., Meisenheimer, K., Rix, H.-W., Borch, A., Dye, S., Kleinheinrich, M., et al.: 2004b, *The Astrophysical Journal* **608**, 752

Benítez, N.: 2000, *The Astrophysical Journal* **536**, 571

Bennert, N., Falcke, H., Schulz, H., Wilson, A. S., and Wills, B. J.: 2002, *The Astrophysical Journal* **574**, L105

Bennert, N., Jungwiert, B., Komossa, S., Haas, M., and Chini, R.: 2006, *Astronomy & Astrophysics* **459**, 55

Bertin, E. and Arnouts, S.: 1996, *Astronomy and Astrophysics Supplement* **117**, 393

Best, P. N. and Heckman, T. M.: 2012, *Monthly Notices of the Royal Astronomical Society* **421**, 1569

Best, P. N., Kaiser, C. R., Heckman, T. M., and Kauffmann, G.: 2006, *Monthly Notices of the Royal Astronomical Society* **368**, L67

Best, P. N., Kauffmann, G., Heckman, T. M., Brinchmann, J., Charlot, S., Ivezić, Ž., and White, S. D. M.: 2005a, *Monthly Notices of the Royal Astronomical Society* **362**, 25

Best, P. N., Kauffmann, G., Heckman, T. M., and Ivezić, Ž.: 2005b, *Monthly Notices of the Royal Astronomical Society* **362**, 9

Best, P. N., Röttgering, H. J. A., and Longair, M. S.: 2000, *Monthly Notices of the Royal Astronomical Society* **311**, 23

Bianchi, S., Maiolino, R., and Risaliti, G.: 2012, *Advances in Astronomy; eprint arXiv:1201.2119*

Bîrzan, L., Rafferty, D. A., McNamara, B. R., Wise, M. W., and Nulsen, P. E. J.: 2004, *The Astrophysical Journal* **607**, 800

Bolzonella, M., Miralles, J.-M., and Pelló, R.: 2000, *Astronomy & Astrophysics* **363**, 476

Bondi, M., Ciliegi, P., Venturi, T., Dallacasa, D., Bardelli, S., Zucca, E., Athreya, R. M., Gregorini, L., T., Garilli, B., Iovino, A., Temporin, S., and Vergani, D.: 2007, *Astronomy and Astrophysics* **463**, 519

Bondi, M., Ciliegi, P., Zamorani, G., Gregorini, L., Vettolani, G., Parma, P., de Ruiter, H., Le Fevre, O., et al.: 2003, *Astronomy and Astrophysics* **403**, 857

Bonfield, D. G., Sun, Y., Davey, N., Jarvis, M. J., Abdalla, F. B., Banerji, M., and Adams, R. G.: 2010, *Monthly Notices of the Royal Astronomical Society* **405**, 987

Bower, R. G., Benson, A. J., Malbon, R., Helly, J. C., Frenk, C. S., Baugh, C. M., Cole, S., and Lacey, C. G.: 2006, *Monthly Notices of the Royal Astronomical Society* **370**, 645

Brammer, G. B., van Dokkum, P. G., and Coppi, P.: 2008, *The Astrophysical Journal* **686**, 1503

Bridle, A. H. and Perley, R. A.: 1984, *Annual Review of Astronomy & Astrophysics* **22**, 319

Bruzual, G. and Charlot, S.: 2003, *Monthly Notices of the Royal Astronomical Society* **344**, 1000

Calzetti, D., Armus, L., Bohlin, R. C., Kinney, A. L., Koornneef, J., and Storchi-Bergmann, T.: 2000, *The Astrophysical Journal* **533**, 682

Calzetti, D., Kennicutt, Jr., R. C., Bianchi, L., Thilker, D. A., Dale, D. A., et al.: 2005, *The Astrophysical Journal* **633**, 871

Camera, S., Santos, M. G., Bacon, D. J., Jarvis, M. J., McAlpine, K., Norris, R. P., Raccanelli, A., and Rottgering, H.: 2012, *e-print arXiv:1205.1048*

Cannon, R., Drinkwater, M., Edge, A., Eisenstein, D., Nichol, R., Outram, P., Pimbblet, K., et al.: 2006, *Monthly Notices of the Royal Astronomical Society* **372**, 425

Cardamone, C. N., van Dokkum, P. G., Urry, C. M., Taniguchi, Y., Gawiser, E., Brammer, G., Taylor, E., Damen, M., Treister, E., Cobb, B. E., Bond, N., Schawinski, K., Lira, P., Murayama, T., Saito, T., and Sumikawa, K.: 2010, *The Astrophysical Journal Supplement* **189**, 270

Casali, M., Adamson, A., Alves de Oliveira, C., and Almaini, O.: 2007, *A & A* **467**, 777

Cattaneo, A., Faber, S. M., Binney, J., Dekel, A., Kormendy, J., Mushotzky, R., Babul, A., Best, P. N., et al.: 2009, *Nature* **460**, 213

Chabrier, G.: 2003, *The Publications of the Astronomical Society of the Pacific* **115**, 763

Chartas, G., Brandt, W. N., Gallagher, S. C., and Proga, D.: 2007, *The Astronomical Journal* **133**, 1849

Chhetri, R., Ekers, R. D., Mahony, E. K., Jones, P. A., Massardi, M., Ricci, R., and Sadler, E. M.: 2012, *Monthly Notices of the Royal Astronomical Society* **422**, 2274

Ciliegi, P., Zamorani, G., Bondi, M., Pozzetti, L., Bolzonella, M., Gregorini, L., Garilli, B., Iovino, A., McCracken, H. J., Mellier, Y., Radovich, M., de Ruiter, H. R., Parma, P., Bottini, D., Le Brun, V., Le Fèvre, O., and Maccagni, D.: 2005, *Astronomy and Astrophysics* **441**, 879

Ciliegi, P., Zamorani, G., Hasinger, G., Lehmann, I., Szokoly, G., and Wilson, G.: 2003, *Astronomy and Astrophysics* **398**, 901

Clewley, L. and Jarvis, M. J.: 2004, *Monthly Notices of the Royal Astronomical Society* **352**, 909

Coleman, G. D., Wu, C.-C., and Weedman, D. W.: 1980, *Astrophysical Journal Supplement Series* **43**, 393

Condon, J. J.: 1974, *The Astrophysical Journal* **188**, 279

Condon, J. J.: 1992, *Annual review of Astronomy and Astrophysics* **30**, 575

Condon, J. J.: 1997, *Publications of the Astronomical Society of the Pacific* **109**, 166

Condon, J. J., Cotton, W. D., and Broderick, J. J.: 2002, *The Astronomical Journal* **124**, 675

Condon, J. J., Cotton, W. D., Greisen, E. W., Yin, Q. F., Perley, R. A., Taylor, G. B., and Broderick, J. J.: 1998, *The Astronomical Journal* **115**, 1693

Croton, D. J., Springel, V., White, S. D. M., De Lucia, G., Frenk, C. S., Gao, L., Jenkins, A., Kauffmann, G., Navarro, J. F., and Yoshida, N.: 2006, *Monthly Notices of the Royal Astronomical Society* **365**, 11

Cruz, M. J., Jarvis, M. J., Rawlings, S., and Blundell, K. M.: 2007, *Monthly Notices of the Royal Astronomical Society* **375**, 1349

de Kool, M., Arav, N., Becker, R. H., Gregg, M. D., White, R. L., Laurent-Muehleisen, S. A., Price, T., and Korista, K. T.: 2001, *The Astrophysical Journal* **548**, 609 de Ruiter, H. R., Arp, H. C., and Willis, A. G.: 1977, *Astronomy and Astrophysics Supplement Series* **28**, 211

Di Matteo, T., Springel, V., and Hernquist, L.: 2005, *Nature* **433**, 604

Donoso, E., Best, P. N., and Kauffmann, G.: 2009, *Monthly Notices of the Royal Astronomical Society* **392**, 617

Doroshkevich, A. G., Longair, M. S., and Zeldovich, Y. B.: 1970, *Monthly Notices of the Royal Astronomical Society* **147**, 139

Downes, A. J. B., Peacock, J. A., Savage, A., and Carrie, D. R.: 1986, *Monthly Notices of the Royal Astronomical Society* **218**, 31

Dunlop, J. S. and Peacock, J. A.: 1990, *Monthly Notices of the Royal Astronomical Society* **247**, 19

Eales, S., Rawlings, S., Law-Green, D., Cotter, G., and Lacy, M.: 1997, *Monthly Notices of the Royal Astronomical Society* **291**, 593

Eisenhauer, F., Genzel, R., Alexander, T., Abuter, R., Paumard, T., Ott, T., Gilbert, A., et al.: 2005, *The Astrophysical Journal* **628**, 246

Evans, D. A., Worrall, D. M., Hardcastle, M. J., Kraft, R. P., and Birkinshaw, M.: 2006, *The Astrophysical Journal* **642**, 96

Evans, I. N., Ford, H. C., Kinney, A. L., Antonucci, R. R. J., Armus, L., and Caganoff, S.: 1991, *The Astrophysical Journal* **369**, L27

Fabian, A. C., Sanders, J. S., Crawford, C. S., Conselice, C. J., Gallagher, J. S., and Wyse, R. F. G.: 2003, *Monthly Notices of the Royal Astronomical Society* **344**, L48

Falder, J. T., Stevens, J. A., Jarvis, M. J., Hardcastle, M. J., Lacy, M., McLure, R. J., Hatziminaoglou, E., Page, M. J., and Richards, G. T.: 2010, *Monthly Notices of the Royal Astronomical Society* **405**, 347

Fanaroff, B. L. and Riley, J. M.: 1974, *Monthly Notices of the Royal Astronomical Society* **167**, 31P

Feldmann, R., Carollo, C. M., Porciani, C., Lilly, S. J., Capak, P., Taniguchi, Y., Le Fèvre, O., et al.: 2006, *Monthly Notices of the Royal Astronomical Society* **372**, 565

Fernández-Soto, A., Lanzetta, K. M., Chen, H.-W., Pascarelle, S. M., and Yahata, N.: 2001, *The Astrophysical Journal Supplement* **135**, 41

Ferrarese, L. and Merritt, D.: 2000, *The Astrophysical Journal* **539**, L9

Firth, A. E., Lahav, O., and Somerville, R. S.: 2003, *Monthly Notices of the Royal Astronomical Society* **339**, 1195

Fleuren, S., Sutherland, W., Dunne, L., Smith, D. J. B., Maddox, S. J., González-Nuevo, J., Findlay, J., et al.: 2012, *e-print arXiv:1202.3891*

Fontana, A., Pozzetti, L., Donnarumma, I., Renzini, A., Cimatti, A., Zamorani, G., Menci, N., Daddi, E., Giallongo, E., Mignoli, M., Perna, C., Salimbeni, S., Saracco, P., Broadhurst, T., Cristiani, S., D'Odorico, S., and Gilmozzi, R.: 2004, *Astronomy & Astrophysics* **424**, 23

Franceschini, A., Vercellone, S., and Fabian, A. C.: 1998, *Monthly Notices of the Royal Astronomical Society* **297**, 817

Garrett, M. A.: 2002, *Astronomy & Astrophysics* **384**, L19

Gebhardt, K., Bender, R., Bower, G., Dressler, A., Faber, S. M., Filippenko, A. V., Green, R., Grillmair, C., Ho, L. C., Kormendy, J., Lauer, T. R., Magorrian, J., Pinkney, J., Richstone, D., and Tremaine, S.: 2000, *The Astrophysical Journal* **539**, L13

Gendre, M. A., Best, P. N., and Wall, J. V.: 2010, *Monthly Notices of the Royal Astronomical Society* **404**, 1719

Ghez, A. M., Salim, S., Hornstein, S. D., Tanner, A., Lu, J. R., Morris, M., Becklin, E. E., and Duchêne, G.: 2005, *The Astrophysical Journal* **620**, 744

Gopal-Krishna and Wiita, P. J.: 2000, *Astronomy & Astrophysics* **363**, 507

Greisen, E.: 2003, *Information Handling in Astronomy - Historical Vistas*, Vol. 285 of *Astrophysics and Space Science Library*, Kluwer Academic Publishers, Dordrecht

Hardcastle, M. J., Evans, D. A., and Croston, J. H.: 2006, *Monthly Notices of the Royal Astronomical Society* **370**, 1893

Hardcastle, M. J., Evans, D. A., and Croston, J. H.: 2007, *Monthly Notices of the Royal Astronomical Society* **376**, 1849

Hardcastle, M. J., Virdee, J. S., Jarvis, M. J., Bonfield, D. G., Dunne, L., Rawlings, S., Stevens, J. A., Christopher, N. M., et al.: 2010, *Monthly Notices of the Royal Astronomical Society* **409**, 122

Hasinger, G.: 2008, *Astronomy & Astrophysics* **490**, 905

Heisler, C. A., Lumsden, S. L., and Bailey, J. A.: 1997, *Nature* **385**, 700

Herbert, P. D., Jarvis, M. J., Willott, C. J., McLure, R. J., Mitchell, E., Rawlings, S., Hill, G. J., and Dunlop, J. S.: 2010, *Monthly Notices of the Royal Astronomical Society* **406**, 1841

Herbert, P. D., Jarvis, M. J., Willott, C. J., McLure, R. J., Mitchell, E., Rawlings, S., Hill, G. J., and Dunlop, J. S.: 2011, *Monthly Notices of the Royal Astronomical Society* **410**, 1360

Herrnstein, J. R., Moran, J. M., Greenhill, L. J., Diamond, P. J., Inoue, M., Nakai, N., Miyoshi, M., Henkel, C., and Riess, A.: 1999, *Nature* **400**, 539

Hewett, P. C., Warren, S. J., Leggett, S. K., and Hodgkin, S. T.: 2006, *Monthly Notices of the Royal Astronomical Society* **367**, 454

Hine, R. G. and Longair, M. S.: 1979, *Monthly Notices of the Royal Astronomical Society* **188**, 111

Ho, L. C.: 2002, *The Astrophysical Journal* **564**, 120

Hogg, D. W.: 1999, *ArXiv Astrophysics e-prints*

Hopkins, A. M., Connolly, A. J., Haarsma, D. B., and Cram, L. E.: 2001, *The Astronomical Journal* **122**, 288

Hopkins, P. F., Hickox, R., Quataert, E., and Hernquist, L.: 2009, *Monthly Notices of the Royal Astronomical Society* **398**, 333

Huynh, M. T., Jackson, C. A., Norris, R. P., and Fernandez-Soto, A.: 2008, *The Astronomical Journal* **135**, 2470

Ibar, E., Ivison, R. J., Biggs, A. D., Lal, D. V., Best, P. N., and Green, D. A.: 2009, *Monthly Notices of the Royal Astronomical Society* **397**, 281

Ilbert, O., Arnouts, S., McCracken, H. J., Bolzonella, M., Bertin, E., Le Fèvre, O., Mellier, Y., et al.: 2006, *Astronomy & Astrophysics* **457**, 841

Ilbert, O., Capak, P., Salvato, M., Aussel, H., McCracken, H. J., Sanders, D. B., Scoville, N., et al.: 2009, *The Astrophysical Journal* **690**, 1236

Ilbert, O., Tresse, L., Zucca, E., Bardelli, S., Arnouts, S., Zamorani, G., Pozzetti, L., et al.: 2005, *Astronomy & Astrophysics* **439**, 863

Iovino, A., McCracken, H. J., Garilli, B., Foucaud, S., Le Fèvre, O., Maccagni, D., Saracco, P., et al.: 2005, *Astronomy and Astrophysics* **442**, 423

Ivison, R. J., Greve, T. R., Dunlop, J. S., Peacock, J. A., Egami, E., Smail, I., et al.: 2007, *Monthly Notices of the Royal Astronomical Society* **380**, 199

Ivison, R. J., Magnelli, B., Ibar, E., Andreani, P., Elbaz, D., Altieri, B., Amblard, A., et al.: 2010, *Astronomy & Astrophysics* **518**, L31

Jackson, C. A. and Wall, J. V.: 1999, *Monthly Notices of the Royal Astronomical Society* **304**, 160

Jackson, N. and Rawlings, S.: 1997, *Monthly Notices of the Royal Astronomical Society* **286**, 241

Jaffe, W., Meisenheimer, K., Röttgering, H. J. A., Leinert, C., Richichi, A., Chesneau, O., Fraix-Burnet, D., et al.: 2004, *Nature* **429**, 47

Janssen, R. M. J., Röttgering, H. J. A., Best, P. N., and Brinchmann, J.: 2012, *Astronomy & Astrophysics* **541**, A62

Jarvis, M. and Rawlings, S.: 2004, *New Astronomy Reviews* **48(11-12)**, 1173

Jarvis, M. J.: 2011, *eprint arXiv:1107.5165*

Jarvis, M. J. and McLure, R. J.: 2002, *Monthly Notices of the Royal Astronomical Society* **336**, L38

Jarvis, M. J. and Rawlings, S.: 2000, *Monthly Notices of the Royal Astronomical Society* **319**, 121

Jarvis, M. J., Rawlings, S., Eales, S., Blundell, K. M., Bunker, A. J., Croft, S., McLure, R. J., and Willott, C. J.: 2001a, *Monthly Notices of the Royal Astronomical Society* **326**, 1585

Jarvis, M. J., Rawlings, S., Willott, C. J., Blundell, K. M., Eales, S., and Lacy, M.: 2001b, *Monthly Notices of the Royal Astronomical Society* **327**, 907

Jarvis, M. J., Smith, D. J. B., Bonfield, D. G., Hardcastle, M. J., Falder, J. T., Stevens, J. A., Ivison, R. J., et al.: 2010, *Monthly Notices of the Royal Astronomical Society* **409**, 92

Johnston, S., Taylor, R., Bailes, M., Bartel, N., Baugh, C., Bietenholz, M., et al.: 2008, *Experimental Astronomy* **22**, 151

Jones, D. H., Saunders, W., Colless, M., Read, M. A., Parker, Q. A., Watson, F. G., Campbell, L. A., et al.: 2004, *Monthly Notices of the Royal Astronomical Society* **355**, 747

Kaspi, S., Maoz, D., Netzer, H., Peterson, B. M., Vestergaard, M., and Jannuzi, B. T.: 2005, *The Astrophysical Journal* **629**, 61

Kauffmann, G., Heckman, T. M., and Best, P. N.: 2008, *Monthly Notices of the Royal Astronomical Society* **384**, 953

Kauffmann, G., Heckman, T. M., Tremonti, C., Brinchmann, J., Charlot, S., White, S. D. M., Ridgway, S. E., et al.: 2003, *Montly Notices of the Royal Astronomical Society* **346**, 1055

Kellermann, K. I., Fomalont, E. B., Mainieri, V., Padovani, P., Rosati, P., Shaver, P., Tozzi, P., and Miller, N.: 2008, *The Astrophysical Journal Supplement Series* **179**, 71

Kellermann, K. I., Sramek, R., Schmidt, M., Shaffer, D. B., and Green, R.: 1989, *The Astronomical Journal* **98**, 1195

Kennicutt, Jr., R. C.: 1998, *Annual Review of Astronomy and Astrophysics* **36**, 189

Kewley, L. J., Dopita, M. A., Sutherland, R. S., Heisler, C. A., and Trevena, J.: 2001, *The Astrophysical Journal* **556**, 121

Kim, J.-W., Edge, A. C., Wake, D. A., and Stott, J. P.: 2011, *Monthly Notices of the Royal Astronomical Society* **410**, 241

Kinney, A. L., Calzetti, D., Bohlin, R. C., McQuade, K., Storchi-Bergmann, T., and Schmitt, H. R.: 1996, *The Astrophysical Journal* **467**, 38

Kishimoto, M., Hönig, S. F., Antonucci, R., Millour, F., Tristram, K. R. W., and Weigelt, G.: 2011, *Astronomy & Astrophysics* **536**, A78

Koratkar, A. and Blaes, O.: 1999, *Publications of the Astronomical Society of the Pacific* **111**, 1

Kormendy, J. and Richstone, D.: 1995, *Annual Review of Astronomy and Astrophysics* **33**, 581

La Franca, F., Fiore, F., Comastri, A., Perola, G. C., Sacchi, N., Brusa, M., Cocchia, F., Feruglio, C., Matt, G., Vignali, C., Carangelo, N., Ciliegi, P., Lamastra, A., Maiolino, R., Mignoli, M., Molendi, S., and Puccetti, S.: 2005, *The Astrophysical Journal* **635**, 864

Lacki, B. C. and Thompson, T. A.: 2010, *The Astrophysical Journal* **717**, 196

Lacki, B. C., Thompson, T. A., and Quataert, E.: 2010, *The Astrophysical Journal* **717**, 1

Lacy, M., Laurent-Muehleisen, S. A., Ridgway, S. E., Becker, R. H., and White, R. L.: 2001, *The Astrophysical Journal* **551**, L17

Laing, R. A., Jenkins, C. R., Wall, J. V., and Unger, S. W.: 1994, in G. V. Bicknell, M. A. Dopita, & P. J. Quinn (ed.), *The Physics of Active Galaxies*, Vol. 54 of *Astronomical Society of the Pacific Conference Series*, p. 201

Laing, R. A., Riley, J. M., and Longair, M. S.: 1983, *Monthly Notices of the Royal Astronomical Society* **204**, 151

Laor, A.: 2000, *The Astrophysical Journal* **543**, L111

Laureijs, R.: 2009, *e-print arXiv:0912.0914*

Laureijs, R., Amiaux, J., Arduini, S., Augueres, J. ., Brinchmann, J., Cole, R., Cropper, M., Dabin, C., Duvet, L., Ealet, A., et al.: 2011, *e-print arXiv:1110.3193*

Lawrence, A., Warren, S. J., Almaini, O., Edge, A. C., Hambly, N. C., Jameson, R. F., Lucas, P., and Casali, M.: 2007, *Monthly Notices of the Royal Astronomical Society* **379**, 1599

Le Fèvre, O., Arnouts, S., Tresse, L., Ilbert, O., Lonsdale, C., Polletta, M., Rowan-Robinson, M., et al.: 2007, *At the Edge of the Universe: Latest Results from the Deepest Astronomical Surveys ASP Conference Series* 380

Le Fèvre, O., Vettolani, G., Garilli, B., Tresse, L., Bottini, D., Le Brun, V., Maccagni, D., et al.: 2005, *Astronomy & Astrophysics* **439**, 845

Le Fèvre, O., Vettolani, G., Paltani, S., Tresse, L., Zamorani, G., et al.: 2004, *Astronomy & Astrophysics* **428**, 1043

Ledlow, M. J. and Owen, F. N.: 1996, *Astronomical Journal* **112**, 9

Levrier, F., Wilman, R. J., Obreschkow, D., Kloeckner, H. R., Heywood, I. H., and Rawlings, S.: 2009, *Proceedings of Wide Field Astronomy &; Technology for the Square Kilometre Array (SKADS 2009). 4-6 November 2009. Chateau de Limelette*

Lilly, S. J. and Longair, M. S.: 1984, *Monthly Notices of the Royal Astronomical Society* **211**, 833

Longair, M. S.: 1966, *Monthly Notices of the Royal Astronomical Society* **133**, 421

Lonsdale, C. J., Smith, H. E., Rowan-Robinson, M., Surace, J., Shupe, D., Xu, C., and Oliver, S. a.: 2003, *Publications of the Astronomical Society of the Pacific* **115**, 897

Lynden-Bell, D.: 1969, *Nature* **223**, 690

Macklin, J. T.: 1982, *Monthly Notices of the Royal Astronomical Society* **199**, 1119

Madau, P.: 1995, *The Astrophysical Journal* **441**, 18

Magorrian, J., Tremaine, S., Richstone, D., Bender, R., Bower, G., Dressler, A., Faber, S. M., et al.: 1998, *The Astronomical Journal* **115**, 2285

Marchesini, D., Celotti, A., and Ferrarese, L.: 2004, *Monthly Notices of the Royal Astronomical Society* **351**, 733

Mauch, T. and Sadler, E. M.: 2007, *Monthly Notices of the Royal Astronomical Society* **375**, 931

Mauduit, J.-C., Lacy, M., Farrah, D., Surace, J. A., Jarvis, M., Oliver, S., Maraston, C., Vaccari, M., et al.: 2012, *eprint arXiv:1206.4060* **124**, 714

McCracken, H. J., Radovich, M., Bertin, E., Mellier, Y., Dantel-Fort, M., Le Fevre, O., Cuillandre, J. C., et al.: 2003, *Astronomy and Astrophysics* **410**, 17

McLure, R. J. and Dunlop, J. S.: 2001, *Monthly Notices of the Royal Astronomical Society* **327**, 199

McLure, R. J. and Dunlop, J. S.: 2002, *Monthly Notices of the Royal Astronomical Society* **331**, 795

McLure, R. J. and Jarvis, M. J.: 2004, *Monthly Notices of the Royal Astronomical Society* **353**, L45

McLure, R. J., Willott, C. J., Jarvis, M. J., Rawlings, S., Hill, G. J., Mitchell, E., Dunlop, J. S., and Wold, M.: 2004, *Monthly Notices of the Royal Astronomical Society* **351**, 347

McNamara, B. R., Wise, M., Nulsen, P. E. J., David, L. P., Sarazin, C. L., Bautz, M., Markevitch, M., Vikhlinin, A., Forman, W. R., Jones, C., and Harris, D. E.: 2000, *The Astrophysical Journal* **534**, L135

McNamara, B. R., Wise, M. W., Nulsen, P. E. J., David, L. P., Carilli, C. L., Sarazin, C. L., O'Dea, C. P., Houck, J., Donahue, M., Baum, S., Voit, M., O'Connell, R. W., and Koekemoer, A.: 2001, *The Astrophysical Journal* **562**, L149

Meier, D. L.: 1999, *The Astrophysical Journal* **522**, 753

Merloni, A., Rudnick, G., and Di Matteo, T.: 2007, in *Relativistic Astrophysics Legacy and Cosmology - Einstein's Legacy, ESO Astrophysics Symposia. Springer-Verlag Berlin Heidelberg*

Miley, G.: 1980, *Annual Review of Astronomy and Astrophysics* **18**, 165

Miyoshi, M., Moran, J., Herrnstein, J., Greenhill, L., Nakai, N., Diamond, P., and Inoue, M.: 1995, *Nature* **373**, 127

Mobasher, B., Idzi, R., Benítez, N., Cimatti, A., Cristiani, S., Daddi, E., Dahlen, T., et al.: 2004, *The Astrophysical Journal Letters* **600**, L167

Moran, E. C., Barth, A. J., Kay, L. E., and Filippenko, A. V.: 2000, *The Astrophysical Journal* **540**, L73

Morganti, R., Rottgering, H., Snellen, I., Miley, G., Barthel, P., Best, P., Bruggen, M., Brunetti, G., Chyzy, K., Conway, J., Jarvis, M., and Lehnert, M.: 2010, *e-print arXiv:1001.2384*

Muxlow, T.: 2010, *"Proceedings of the 10th European VLBI Network Symposium and EVN Users Meeting: VLBI and the new generation of radio arrays". September 20-24*

Muxlow, T. W. B., Richards, A. M. S., Garrington, S. T., Wilkinson, P. N., Anderson, B., Richards, E. A., Axon, D. J., Fomalont, E. B., Kellermann, K. I., Partridge, R. B., and Windhorst, R. A.: 2005, *Monthly Notices of the Royal Astronomical Society* **358**, 1159

Myers, S.: 2010, *American Astronomical Society* 42

Norris, R.: 2011, *eprint arXiv:1111.6318*

Novikov, I. D. and Thorne, K. S.: 1973, in C. Dewitt and B. S. Dewitt (eds.), *Black Holes (Les Astres Occlus)*, pp 343–450

Ogle, P., Whysong, D., and Antonucci, R.: 2006, *The Astrophysical Journal* **647**, 161

Oliver, S. J., Bock, J., Altieri, B., Amblard, A., Arumugam, V., Aussel, H., Babbedge, T., Beelen, A., et al.: 2012, *e-print arXiv:1203.2562*

Osterbrock, D. E.: 1989, *Astrophysics of gaseous nebulae and active galactic nuclei*

Padovani, P., Mainieri, V., Tozzi, P., Kellermann, K. I., Fomalont, E. B., Miller, N., Rosati, P., and Shaver, P.: 2009, *The Astrophysical Journal* **694**, 235

Padovani, P., Miller, N., Kellermann, K. I., Mainieri, V., Rosati, P., and Tozzi, P.: 2011, *The Astrophysical Journal* **740**, 20

Perley, R. A., Dreher, J. W., and Cowan, J. J.: 1984, *The Astrophysical Journal* **285**, L35

Peterson, B. M., Ferrarese, L., Gilbert, K. M., Kaspi, S., Malkan, M. A., Maoz, D., Merritt, D., Netzer, H., Onken, C. A., Pogge, R. W., Vestergaard, M., and Wandel, A.: 2004, *The Astrophysical Journal* **613**, 682

Pogge, R. W.: 1988, *The Astrophysical Journal* **332**, 702

Polletta, M., Tajer, M., Maraschi, L., Trinchieri, G., Lonsdale, C. J., Chiappetti, L., Andreon, S., et al.: 2007, *The Astrophysical Journal* **663**, 81

Pozzetti, L., Bolzonella, M., Lamareille, F., Zamorani, G., Franzetti, P., Le Fèvre, O., Iovino, A., et al.: 2007, *Astronomy & Astrophysics* **474**, 443

Prevot, M. L., Lequeux, J., Prevot, L., Maurice, E., and Rocca-Volmerange, B.: 1984, *Astronomy & Astrophysics* **132**, 389

Raccanelli, A., Zhao, G.-B., Bacon, D. J., Jarvis, M. J., Percival, W. J., Norris, R. P., Rottgering, H., et al.: 2012, *e-print arXiv:1108.0930*

Ranalli, P., Comastri, A., and Setti, G.: 2003, *Astronomy & Astrophysics* **399**, 39

Richards, G. T., Weinstein, M. A., Schneider, D. P., Fan, X., Strauss, M. A., Vanden Berk, D. E., Annis, J., et al.: 2001, *The Astronomical Journal* **122**, 1151

Richter, .: 1975, *Astronomische Nachrichten* **296**, 65

Rigby, E. E., Best, P. N., Brookes, M. H., Peacock, J. A., Dunlop, J. S., Röttgering, H. J. A., Wall, J. V., and Ker, L.: 2011, *Monthly Notices of the Royal Astronomical Society* **416**, 1900

Rigby, E. E., Snellen, I. A. G., and Best, P. N.: 2007, *Monthly Notices of the Royal Astronomical Society* **380**, 1449

Röttgering, H., Afonso, J., Barthel, P., Batejat, F., Best, P., Bonafede, A., Brüggen, M., et al.: 2011, *Journal of Astrophysics and Astronomy* **32**, 557

Rowan-Robinson, M.: 1968, *Monthly Notices of the Royal Astronomical Society* **138**, 445

Rupke, D. S. N. and Veilleux, S.: 2011, *The Astrophysical Journal* **729**, L27

Sadler, E. M., Cannon, R. D., Mauch, T., Hancock, P. J., Wake, D. A., Ross, N., Croom, S. M., et al.: 2007, *Monthly Notices of the Royal Astronomical Society* **381**, 211

Sadler, E. M., Jackson, C. A., Cannon, R. D., McIntyre, V. J., Murphy, T., Bland-Hawthorn, J., Bridges, T., Cole, S., et al.: 2002, *Monthly Notices of the Royal Astronomical Society* **329**, 227

Salim, S., Charlot, S., Rich, R. M., Kauffmann, G., Heckman, T. M., Barlow, T. A., Bianchi, L., et al.: 2005, *The Astrophysical Journal* **619**, L39

Salim, S., Rich, R. M., Charlot, S., Brinchmann, J., Johnson, B. D., Schiminovich, D., Seibert, M., et al.: 2007, *The Astrophysical Journal Supplement Series* **173**, 267

Salpeter, E. E.: 1964, *The Astrophysical Journal* **140**, 796

Salvato, M., Hasinger, G., Ilbert, O., Zamorani, G., Brusa, M., Scoville, N. Z., Rau, A., et al.: 2009, *The Astrophysical Journal* **690**, 1250

Salvato, M., Ilbert, O., Hasinger, G., Rau, A., Civano, F., Zamorani, G., Brusa, M., et al.: 2011, *The Astrophysical Journal* **742**, 61

Sawicki, M. J., Lin, H., and Yee, H. K. C.: 1997, *The Astronomical Journal* **113**, 1

Schmidt, M.: 1968, *The Astrophysical Journal* **151**, 393

Schmitt, H. R., Donley, J. L., Antonucci, R. R. J., Hutchings, J. B., Kinney, A. L., and Pringle, J. E.: 2003, *The Astrophysical Journal* **597**, 768

Seymour, N., Dwelly, T., Moss, D., McHardy, I., Zoghbi, A., Rieke, G., Page, M., Hopkins, A., and Loaring, N.: 2008, *Monthly Notices of the Royal Astronomical Society* **386**, 1695

Seymour, N., Stern, D., De Breuck, C., Vernet, J., Rettura, A., Dickinson, M., Dey, A., et al.: 2007, *The Astrophysical Journal Supplement Series* **171**, 353

Seymour, N., Symeonidis, M., Page, M. J., Amblard, A., Arumugam, V., Aussel, H., Blain, A., et al.: 2011, *Monthly Notices of the Royal Astronomical Society* **413**, 1777

Shakura, N. I. and Sunyaev, R. A.: 1973, *Astronomy & Astrophysics* **24**, 337

Silk, J. and Rees, M. J.: 1998, *Astronomy & Astrophysics* **331**, L1

Simpson, C.: 2005, *MNRAS* **360**, 565

Simpson, C., Almaini, O., Cirasuolo, M., Dunlop, J., Foucaud, S., Hirst, P., Ivison, R., Page, M., Rawlings, S., Sekiguchi, K., Smail, I., and Watson, M.: 2006, *Monthly Notices of the Royal Astronomical Society: Letters* **373**, L21

Simpson, C., Rawlings, S., Ivison, R., Akiyama, M., Almaini, O., Bradshaw, E., Chapman, S., et al.: 2012, *Monthly Notices of the Royal Astronomical Society* **421**, 3060

Smith, D. J. B., Dunne, L., Maddox, S. J., Eales, S., Bonfield, D. G., Jarvis, M. J., Sutherland, W., et al.: 2011, *Monthly Notices of the Royal Astronomical Society* **416**, 857

Smolčić, V. and Riechers, D. A.: 2011, *The Astrophysical Journal* **730**, 64

Smolčić, V., Schinnerer, E., Scodeggio, M., Franzetti, P., Aussel, H., Bondi, M., Brusa, M., et al.: 2008, *The Astrophysical Journal Supplement Series* **177**, 14

Smolčić, V., Schinnerer, E., Zamorani, G., Bell, E. F., Bondi, M., Carilli, C. L., Ciliegi, P., et al.: 2009a, *The Astrophysical Journal* **690**, 610

Smolčić, V., Zamorani, G., Schinnerer, E., Bardelli, S., Bondi, M., Bîrzan, L., Carilli, C. L., et al.: 2009b, *The Astrophysical Journal* **696**, 24

Strateva, I., Ivezić, Ž., Knapp, G. R., Narayanan, V. K., Strauss, M. A., Gunn, J. E., Lupton, R. H., et al.: 2001, *The Astronomical Journal* **122**, 1861

Strazzullo, V., Pannella, M., Owen, F. N., Bender, R., Morrison, G. E., Wang, W.-H., and Shupe, D. L.: 2010, *The Astrophysical Journal* **714**, 1305

Sutherland, W. and Saunders, W.: 1992, *Monthly Notices of the Royal Astronomical Society* **259**, 413

Szokoly, G. P., Bergeron, J., Hasinger, G., Lehmann, I., Kewley, L., Mainieri, V., Nonino, M., et al.: 2004, *The Astrophysical Journal Supplement Series* **155**, 271

Tasse, C., Best, P. N., Röttgering, H., and Le Borgne, D.: 2008, *A & A* **490**, 893

Tasse, C., Röttgering, H. J. A., Best, P. N., Cohen, A. S., Pierre, M., and Wilman, R.: 2007, *A & A* **471**, 1105

Taylor, G. B., Perley, R. A., Inoue, M., Kato, T., Tabara, H., and Aizu, K.: 1990, *The Astrophysical Journal* **360**, 41

Tran, H. D.: 2001, *The Astrophysical Journal* **554**, L19

Tran, H. D.: 2003, *The Astrophysical Journal* **583**, 632

Tremaine, S., Gebhardt, K., Bender, R., Bower, G., Dressler, A., Faber, S. M., Filippenko, A. V., Green, R., Grillmair, C., Ho, L. C., Kormendy, J., Lauer, T. R., Magorrian, J., Pinkney, J., and Richstone, D.: 2002, *The Astrophysical Journal* **574**, 740

Tristram, K. R. W., Raban, D., Meisenheimer, K., Jaffe, W., Röttgering, H., Burtscher, L., Cotton, W. D., Graser, U., Henning, T., Leinert, C., Lopez, B., Morel, S., Perrin, G., and Wittkowski, M.: 2009, *Astronomy & Astrophysics* **502**, 67

Urry, C. M. and Padovani, P.: 1995, *Publications of the Astronomical Society of the Pacific* **107**, 803

Vanzella, E., Cristiani, S., Fontana, A., Nonino, M., Arnouts, S., Giallongo, E., Grazian, A., Fasano, G., Popesso, P., Saracco, P., and Zaggia, S.: 2004, *Astronomy & Astrophysics* **423**, 761

Vermeulen, R. C. and Cohen, M. H.: 1994, *The Astrophysical Journal* **430**, 467

Voelk, H. J.: 1989, *Astronomy & Astrophysics* **218**, 67

Voit, G. M. and Donahue, M.: 2005, *The Astrophysical Journal* **634**, 955

Waddington, I., Dunlop, J. S., Peacock, J. A., and Windhorst, R. A.: 2001, *Monthly Notices of the Royal Astronomical Society* **328**, 882

Wall, J. V., Jackson, C. A., Shaver, P. A., Hook, I. M., and Kellermann, K. I.: 2005, *Astronomy & Astrophysics* **434**, 133

Wang, Y., Bahcall, N., and Turner, E. L.: 1998, *The Astronomical Journal* **116**, 2081

White, S. D. M. and Frenk, C. S.: 1991, *The Astrophysical Journal* **379**, 52

Willott, C. J., Rawlings, S., Blundell, K. M., and Lacy, M.: 2000, *MNRAS* **316**, 449

Willott, C. J., Rawlings, S., Blundell, K. M., Lacy, M., and Eales, S. A.: 2001, *Monthly Notices of the Royal Astronomical Society* **322**, 536

Willott, C. J., Rawlings, S., Blundell, K. M., Lacy, M., Hill, G. J., and Scott, S. E.: 2002, *Monthly Notices of the Royal Astronomical Society* **335**, 1120

Willott, C. J., Rawlings, S., Jarvis, M. J., and Blundell, K. M.: 2003, *Monthly Notices of the Royal Astronomical Society* **339**, 173

Wilman, R. J., Jarvis, M. J., Mauch, T., Rawlings, S., and Hickey, S.: 2010, *Monthly Notices of the Royal Astronomical Society* **405**, 447

Wilman, R. J., Miller, L., Jarvis, M. J., Mauch, T., Levrier, F., Abdalla, F. B., Rawlings, S., Klckner, H.-R., Obreschkow, D., Olteanu, D., and Young, S.: 2008, *Monthly Notices of the Royal Astronomical Society* **388**, 1335

Windhorst, R. A., Kron, R. G., and Koo, D. C.: 1984, *Astronomy and Astrophysics Supplement* **58**, 39

Windhorst, R. A., Miley, G. K., Owen, F. N., Kron, R. G., and Koo, D. C.: 1985, *The Astrophysical Journal* **289**, 494

Wolf, C., Meisenheimer, K., Kleinheinrich, M., Borch, A., Dye, S., Gray, M., Wisotzki, L., Bell, E. F., Rix, H.-W., Cimatti, A., Hasinger, G., and Szokoly, G.: 2004, *Astronomy and Astrophysics* **421**, 913

Woo, J.-H. and Urry, C. M.: 2002, *The Astrophysical Journal* **581**, L5

Wright, E. L., Eisenhardt, P. R. M., Mainzer, A. K., Ressler, M. E., Cutri, R. M., Jarrett, T., Kirkpatrick, J. D., et al.: 2010, *The Astronomical Journal* **140**, 1868

Yip, C. W., Connolly, A. J., Vanden Berk, D. E., Scranton, R., Krughoff, S., Szalay, A. S., Dobos, L., Tremonti, C., Taghizadeh-Popp, M., Budavári, T., Csabai, I., Wyse, R. F. G., and Ivezić, Ž.: 2009, *The Astronomical Journal* **137**, 5120

York, D. G., Adelman, J., Anderson, Jr., J. E., Anderson, S. F., Annis, J., Bahcall, N. A., Bakken, J. A., et al.: 2000, *The Astronomical Journal* **120**, 1579

Yun, M. S., Reddy, N. A., and Condon, J. J.: 2001, *The Astrophysical Journal* **554**, 803

Zel'Dovich, Y. B.: 1964, *Soviet Physics Doklady* **9**, 195

Appendix A

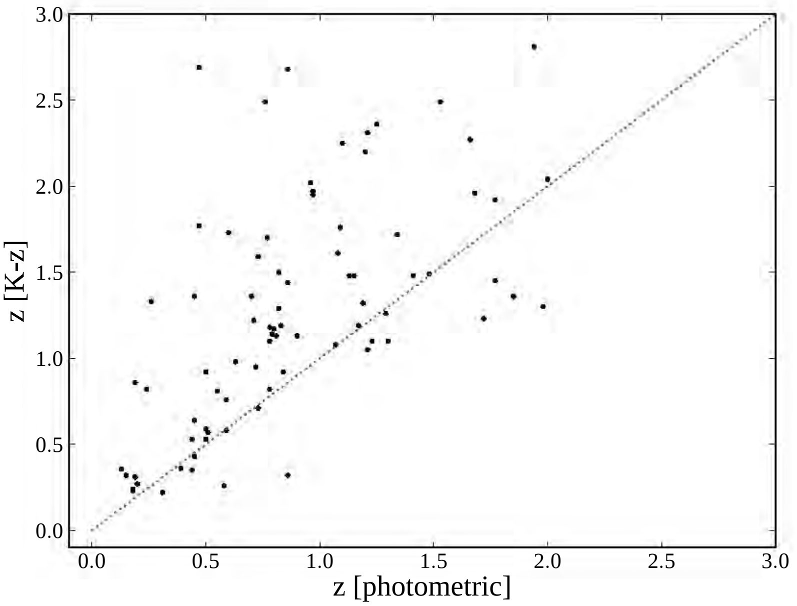

Figure A.1: Comparison of redshifts estimated via the *K*-z relation and photometric redshifts utilised by Tasse et al. (2008) in their study of the evolution of radio sources in the XMM-LSS field.

Figure A.1 presents a comparison of redshifts estimated via the *K*-z relation and photometric redshifts estimated from $u^*g'r'i'z'$ optical bands in the CFHTLS survey and mid-infrared SWIRE data at 3.6, 4.5, 5.8 and 8 μm. These photometric redshifts were used by Tasse et al. (2008) in their analysis of the properties and evolution of radio sources in the XMM-LSS field. The *K*-z redshifts are linearly related to the photometric redshifts with a large scatter. It would appear that the *K*-z relation has a tendency to estimate slightly higher than the multi-band SED fitting method.